Flow Sensors and their Application to Convective Transport of Heat in Logistic Containers

Safir Issa

University of Bremen 2014

Flow Sensors and their Application to Convective Transport of Heat in Logistic Containers

Vom Fachbereich für Physik und Elektrotechnik
der Universität Bremen

Zur Erlangung des akademischen Grades eines

Doktor-Ingenieur (Dr.-Ing.)

genehmigte Dissertation

von

M.Sc. Safir Issa

aus Syrien

Contents

List of Figures

2

4

List of Tables

Abstract

Flow measurement has achieved huge strides in the last few decades. Flow phenomenon is intrinsic to all aspects of life but is still very complex and requires further research. This phenomenon is a source that stimulates new applications. Performing an airflow measurement in logistic containers in order to maintain quality of sensitive products is one of these up-to-date applications. No sensor among the huge number of available sensors in the market is capable to satisfy all measurement requirements for this application. These requirements include the small size, high sensitivity, and ability for wireless measurements of the searched sensors. Therefore, thermal flow sensors developed by MEMS[1] technology are attractive candidates for this mission.

This thesis has two main objectives: First, to prove the suitability and capability of thermal flow micro-sensors in their performance of accurate airflow measurements. The second objective is to perform measurements and simulations in order to understand the convective transport inside reefer containers and improve the cooling system efficiency.

On the sensor side, basic research studies were performed, including modeling, characterization, calibration, and integration in wireless measurement system. The main breakthroughs in this part are studying the response time, minimum detectable air velocity, and developing new test device and calibration method. On the application side, several airflow field tests have been conducted. Additionally, a CFD[2] simulation model for turbulent flow inside the container was developed. Experimental results supported the simulation results, wherein both give a comprehensive understanding to the airflow distribution and convective transport in the container. Moreover, they are able to predict the place of forming of hotspot areas. These findings were confirmed through comparison with the results of temperature field tests performed ashore and offshore during the last four years. Several simulations were performed to improve the cooling system efficiency by comparing the results of different pallet layouts in the container. It was found that a new layout, called "chimney layout", produced the best airflow distribution and achieved the highest efficiency of the cooling system. In this new distribution the pallets are distributed in a way that a considerable gap is created between four pallets. This result was also validated all by temperature field test results.

---

[1]Microelectromechanical Systems
[2]Computational Fluid Dynamics

Dissertation Structure

The thesis title "Flow sensors and their application to convective transport of heat in logistic containers" expresses the core of the achieved work. The activities related to this thesis were conducted at the interface between different research groups including microsystems, sensors, fluid dynamics and logistics. For this reason this thesis is constructed with seven independent chapters, each with its own literature review, objectives, methods or results.

Chapter one is an introduction to the transport operation of sensitive products and the challenges facing this logistic operation in order to maintain the product's quality. Obtaining airflow pattern, by measurements and simulations, is crucial to understand convective transport in the container and to improve the efficiency of the cooling system. This requires flow sensors for the measurements and a CFD model for simulations. On the one hand, the chapter introduces a brief history about flow measurement, different flow sensor principles and their classification. Then, the choice of thermal flow micro-sensor as potential candidate is cited. On the other hand, this chapter introduces airflow distribution in enclosed areas and a brief introduction to different CFD approaches. It afterwards gives more details about the selected k-ε method to perform the simulations.

Chapter two introduces a simple numerical analysis approach that characterises thermal flow sensor behaviour and evaluates its response time. This model solves heat transfer equations with the sensor membrane. It takes into consideration the transient conduction and convection between the sensor and the surrounding fluid. Program results are confirmed by experimental measurements which explain the response time dependence of the velocity and the sensor geometry.

Chapter three characterises the different parameters of the thermal flow sensors such as characteristic curves, responsivity and minimum detectable flow. sec. 3.5 in particular, deals with the minimum detectable air velocity. In this section a presentation of a simple physical method was developed to generate very low flow rates in the mixed convection region. Natural convection and noise at zero flow case are studied in order to evaluate the minimum detectable flow by the sensor.

Chapter four discusses the calibration of the sensors. A new calibration test device is designed and manufactured for this purpose. A calibration method based on the comparison between a reference device and the sensor under calibration is used. In this method the deviation and the uncertainty of measurement are calculated. This method is applied to calibrate the developed airflow sensors in addition to some other flow sensors that were used in field tests.

Chapter five describes the experimental measurements performed in different field tests and introduces the different manipulated sensors. In addition, it describes the container where the measurements took place. It also introduces the infrastructure that enables wireless airflow measurements within the already established network. This chapter shows some tests results after performing the necessary treatment and analysis.

Chapter six describes the k-ε model which was built in order to simulate the turbulent flow inside the container. After that, it presents the simulation results including analysis to the airflow pattern and comparison between different layouts of pallets in the container. Moreover, the chapter compares simulations to the experimental measurements in order to validate the simulations. Results agree with temperature measurement results (performed ashore and offshore during the last four years). This agreement is reflected by the hot spots formed in the container. Additionally, simulations and temperature measurement results prove that using a new distribution of pallets called "chimney layout" is providing better efficiency of the cooling system.

Finally, chapter seven summarises the methods, approaches and results achieved by this study. It also provides conclusions and interpretations to the obtained results. It provides, at the end, some related outlook issues that can be done in future.

Fig. 0.1 represents a schematic draw of the dissertation's structure. The coloured boxes in this figure, refer to group activities achieved within the "Intelligent Container" project, however, they were not carried out by the author. For this reason the details of these activities are not mentioned in this study.
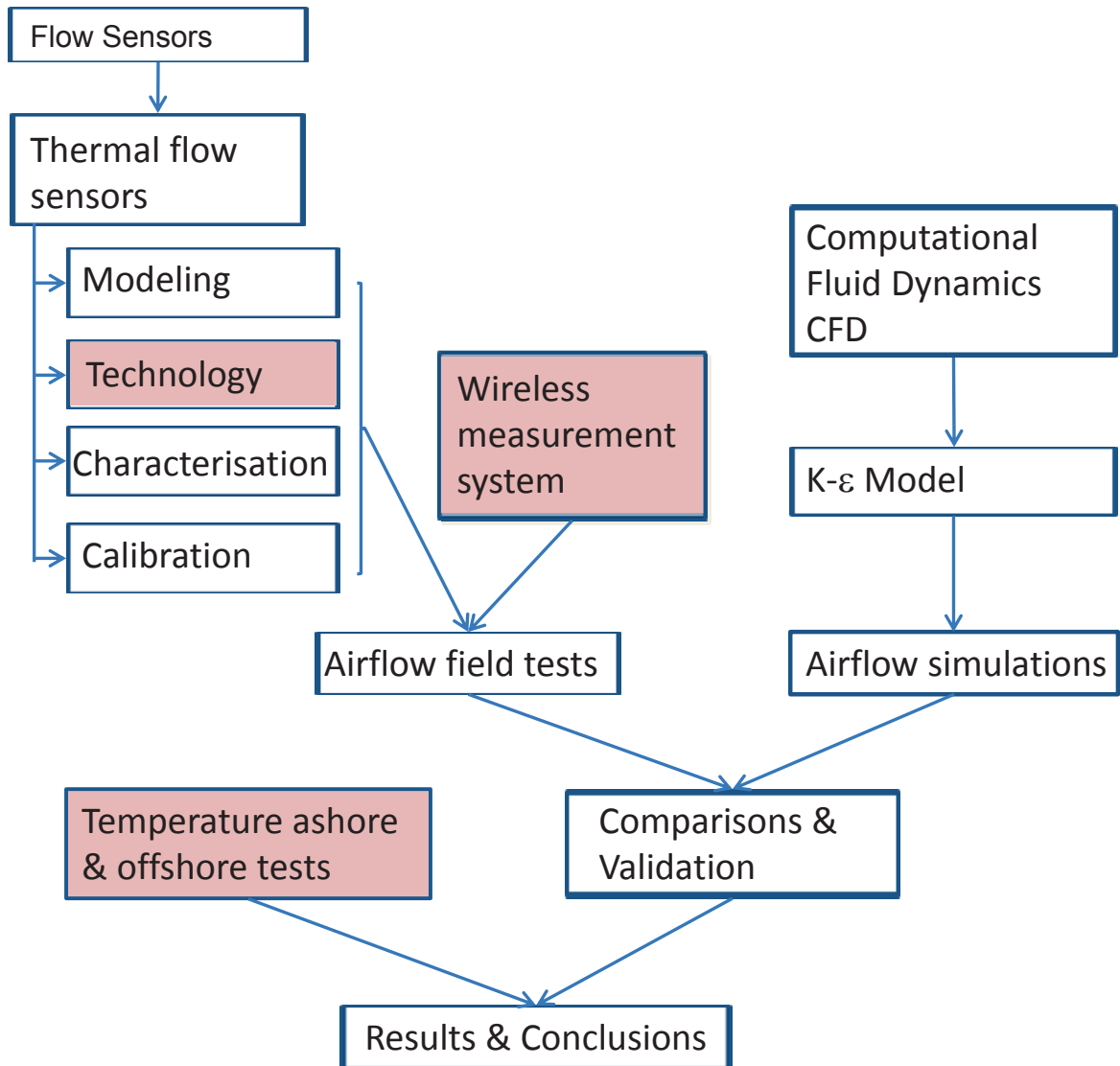
Figure 0.1: Structure of the dissertation. Coloured boxes refer to activities performed not by the author, they are not treated in this thesis

1 Introduction

Nowadays, the "fresh" agricultural produce is available in markets all year round due to huge progress in logistic networks. Nevertheless, the intercontinental transport of sensitive products still has serious challenges to overcome in order to maintain the required quality. Some products, such as bananas, are very sensitive to ambient conditions of transport and storage. For that reason, as well as the strict legal regulations, producers are forced to ensure the arrival of these products at their consumers in a good condition. Regarding fruit and vegetables, temperature is the dominant environmental factor that influences their deterioration, effecting their external shape, quality and shelf life. Temperatures either above or below the optimal range for fresh products can cause rapid deterioration due to freezing, chilling injury or heat injury [Kade04]. Thus maintaining a specific temperature throughout the container during the whole transport process is an essential matter to keep the product's quality and to reduce its losses. In reefer containers, convection is the dominant mode of heat transfer; therefore, the temperature and its distribution are governed by the airflow pattern[Mour09]. However, it is very difficult to obtain homogeneous distribution of airflow inside the container. The internal production of heat and moisture generated by fruit and vegetables are supplementary parameters that affect the temperature profile. The internal geometry of container causes more turbulence to the airflow. All equipped pallets and boxes can provide only narrow spaces and holes for air current passages. Therefor, obtaining airflow pattern (by measurements and simulations) will provide a better understanding of convection transport inside the container and will identify the stagnant zones where the air flow is very poor. Temperatures in these zones are surely higher than expected, as the air circulation is not able to remove the generated heat. Moreover, analysing results may improve the efficiency of the air conditioning system, in order to avoid forming stagnant zones and to obtain more homogeneity in temperature distribution. Fig. 1.1 depicts the temperature effect on sensitive products and the benefits of obtaining the airflow pattern by measurements and simulations in improving transport conditions.

To the extent of understanding airflow behavior in such enclosed areas, researchers have been developing airflow models for the last four decades [Amba13]. With the new powerful computers, Computational Fluid Dynamics (CFD) have become their preferred choice. Such numerical models, regarding their advantages of fast time and low cost, offer a powerful tool to understand fluid flow and heat transfer in the intended enclosed environments. However, they cannot replace the extensive, costly experiments which are imperative. Some examples of the reported CFD and
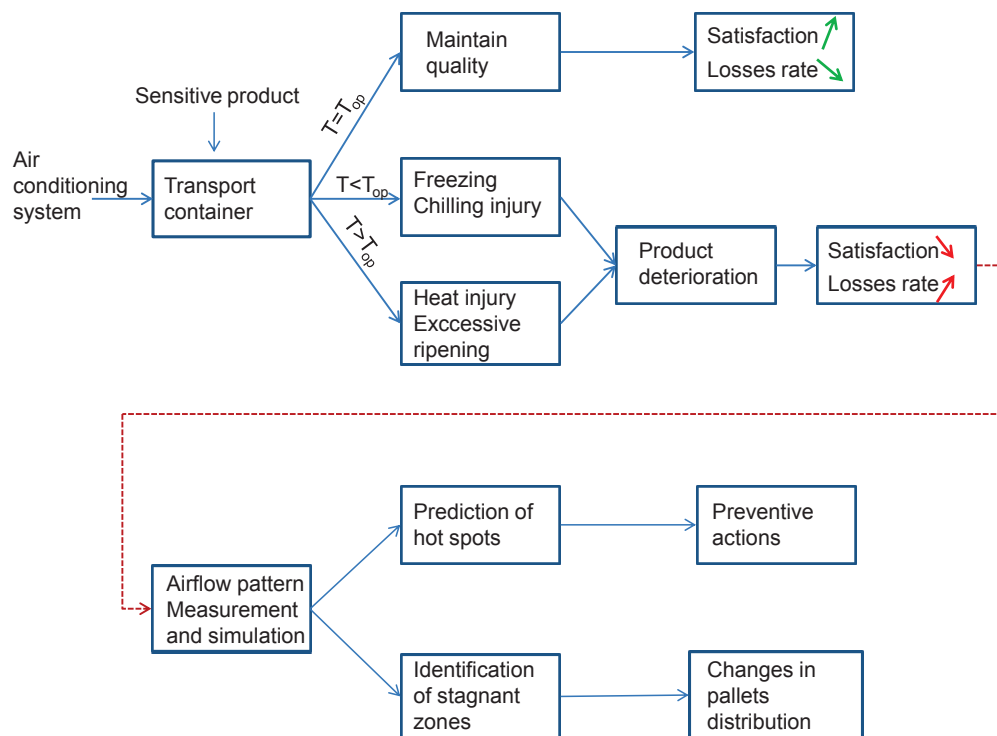
Figure 1.1: Effect of temperature on the sensitive products and the estimated role of airflow measurements

parametric studies are mentioned here. Zou et al. [Zou06-1, Zou06-2] developed a CFD modeling system of the airflow patterns and heat transfer inside a ventilated apple package through forced air cooling. The model was validated by temperature measurements of the apples, and this model is concerning the food packages and not the whole container. Moureh et al. [Mour09] presented a numerical approach and experimental characterisation of airflow within a semi-trailer enclosure loaded with pallets in a refrigerated vehicle with and without air ducts. Measurements of air velocities were carried out by a laser Doppler velocimeter in clear regions (above the pallets) and thermal sphere-shaped probes located inside the pallets. The velocimeter was placed outside the vehicle and the measurements were done through a glass window. Results showed the importance of narrow spaces around pallets to reduce temperature variability in the truck, in addition to the fact of using air ducts which improved the ventilation homogeneity. Xie et al. [Xie06] presented a CFD model which studies the effect of design parameters on flow and temperature field of a cold store. The complexity of airflow pattern analysis and its dependency on many operating conditions have pushed many researchers to recommend further parametric studies [Smal06]. In this context, Laguerre et al. [Lagu12] presented an experimental study of heat transfer and air flow in a vertical and open refriger-

ated cabinet loaded with packages. Rodriguez-Bermejo et al. [Rodr07] presented temperature distributions in a transport container by performing a thermal study. By testing several experimental conditions, it was found that the difference in temperature between the set point and the temperature inside the container rises up to 30% of ambient temperature. Jedermann et al. [Jede13], within the intelligent container project [Lang11], showed an online monitoring and supervision system of spatial temperature deviations in a 40-foot container loaded with bananas during its two-week offshore transportation from Central America to Europe. Temperature curves were recorded at several positions in the centers and corners of banana boxes. In the interest of evaluating spatial deviations of the speed of temperature changes, the related curves were approximated by a structured system model.

During temperature tests (ashore and offshore) it was found that there are large differences between the pallets for the local speed or efficiency of the cooling process. The difference in gap width causes difference in temperature between pallets [Jede13]. However, it was also found that the temperature difference depends on pallet position by experiments. These phenomena require analysing the airflow pattern to be understood. The goal of this study is to investigate methods with regard to perform airflow measurements inside the container and to support the results by CFD simulations.

Performing airflow measurements inside logistic containers require manipulating appropriate flow sensors whereas obtaining airflow simulations implies using suitable computational fluid dynamics approach.

On the one hand, Section (sec. 1.1) introduces a brief history to flow measurement and the different principles of flow sensors. More details about the selected thermal flow sensors are provided.

On the other hand, Section (sec. 1.2) presents famous computational fluid dynamic approaches after a short description of the turbulence problem. Furthermore, an introduction to the k-ε method (which was selected to build simulation models) is given.

The research question in this thesis therefore is two-fold:

Are thermal flow sensors capable and suitable for accurate airflow measurement in reefer containers?

&

How do airflow measurements and simulations improve transport processes for logistic containers?

1.1 Flow Sensors

Progress in flow measurement has always been a sign of human civilisation. Ancient Egyptians used flow techniques to measure water flows for the purpose of irrigation.

In addition, they studied the Nile river-flow to predict the annual harvest. Romans, over 2000 years ago, developed flow meters to measure adequate drainage pipes. The early Chinese measured salt water to control flows in special pots in the interest of producing salt. Mankind has invested much effort to understand fluid flow, because it has a direct impact in many industrial, technical and daily situations. These applications include: wind velocity and direction (crucial for forecast and ship transport), respiration and blood flow (essential in Biomedics), and distribution of gas and oil. These examples reflect the importance of this science which is still evolving.

The main stages of this flow science evolution started in the eighteenth century. In that time the mathematical development appeared especially with the equations of Bernoulli and Euler. In 1790 Venturi has published a paper about a new metering device which later holds his name. In the nineteenth century, positive displacement meters were steadily developed. Additionally, the first successful gas meter was reported in 1815, and a few years later, water meters appeared.

In the early twentieth century the most common meters came out, such as: Orifice plate, Propeller meters and Pitot tubes. Since 1950, an explosion of flow metering innovations has occurred. Most of the important techniques appeared after that date. These techniques include ultrasonic, direct mass, vortex, electromagnetic, and magnetic resonance meters. Some important flow meters release dates are: Ultrasonic Doppler meters in 1970, Coriolis mass meters in 1977, and Wedge differential pressure meter in 1978. It is important to mention that the physical principles on which these techniques work were established long time before the commercial meters came out. For example the first commercial magnetic meter appeared in 1950, although Faraday established the measurement principle in 1832 [Furn89, Spit84].

In the last decades, a huge development in micromachining occured, this allowed the miniaturisation of existing sensors. Additionally, this development enabled obtaining better resolutions than before. Batch production of the microsensors introduced the advantage of producing low cost sensors. Consequently, new applications have came out such as the array sensing enabling an instantaneous representation of a complex flow. Moreover, new sensor principles published which are based on new materials such as carbon nanotubes (CNTS)[Haas08]. So far, however, not all macroscopic flow measurement systems can be realised as microsensors such as the Laser Doppler Anemometer [Lang12]. In spite of all this huge progress, there are still many problems to be solved regarding complex flow phenomenon. Despite the hundreds of different flow sensors available in the market not one can be used in all situations!

1.1.1 Flow Sensors Principles

There are many ways to classify flow sensors. Spitzer [Spit84] grouped flow meters into four classes and four types. Furness [Furn89] suggested 12 groups for

flow meters according to their operating principle. These groups include meters of Differential-pressure, Positive displacement, Rotary inferential, Fluid oscillatory, Electromagnetic, Ultrasonic, Direct mass, Thermal, Miscellaneous, Solid meters and Open channel types. Haasl and Stemme [Haas08] classified micromachined flow sensors into 8 groups according to the application domain and their operating principle. These groups are thermal, mechanical, differential-pressure, optical, ultrasonic, coriolis, direct Electrical and CNT-based flow sensors.

A short introduction to some basic flow principles follows:

1.1.1.1 Differential-Pressure Principle

Orifice meters, Venturi tubes, Flow nozzles, and Pitot tubes are famous meters that belong to the differential-pressure flow groups .This group contains a wide variety of meter size and shape, used for both gas and liquid applications. Regardless of their design, they have the same principle: all follow the Bernoulli equation.

$$P + \frac{1}{2}\rho \cdot v^2 + \rho \cdot g \cdot h = P_0 = Constant \tag{1.1}$$

where P is the pressure (or static pressure), ρ is the fluid density, v is the mean velocity of the fluid, g is the acceleration of gravity, h is the height and P_0 is the total pressure. The first term in the left side of the previous equation represents the static pressure (pressure energy), the second term represents the dynamic pressure (kinetic energy) and the third term represents the hydrostatic pressure. For a fluid with very slight changes of height the term $\rho \cdot g \cdot h$ can be neglected. When a fluid of density ρ flows in a pipe of cross section area A_1 with a mean velocity v_1 and related pressure P_1 passes through a restriction in the pipe in a way the cross section area reduced to A_2 then the mean velocity increases to v_2 and the pressure falls to P_2, as presented in Fig. 1.2 and described in the following equation:

$$P_1 + \frac{1}{2}\rho v_1^2 = P_2 + \frac{1}{2}\rho v_2^2 = P_0 \tag{1.2}$$

The continuity equation applied on both sections of the pipe given as:

$$Q = A_1 v_1 = A_2 v_2 \tag{1.3}$$

where Q is the volume flow.
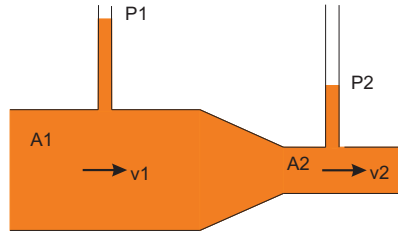
Figure 1.2: Representation of differential pressure principle on a flow in a pipe

By considering $m = A_2/A_1$, substituting Equation 1.3 in Equation 1.2, and multiplying the resulted equation by an empirical constant C_D (discharge coefficient) we obtain:

$$Q_a = C_D \cdot \frac{A_2}{(1-m)^{1/2}} \cdot (\frac{2(P_1 - P_2)}{\rho})^{1/2} \tag{1.4}$$

The discharge coefficient is used to compensate losses of temperature, pressure, compressibility and other factors. In the case of gas flow the mean velocity is function of the area and density which is not constant anymore. Therefore, Equation 1.4 is multiplied by a complex expansion factor Y_1 [Furn89]. The resultant equation is considered a universal equation for one meter works in a single-phase fluid. However, it is not valid for a two-phase fluid where only empirically derived correlations are required [Furn89].

1.1.1.2 Electromagnetic Flow Sensors

Electromagnetic flow sensors follow Faraday's law of induction. This law states that a voltage will be induced when a conductor, the fluid in this case, moves through a magnetic field. The magnitude of the induced voltage U is proportional to the mean velocity of the medium $\bar{v}$, the strength of the magnetic flux B and the pipe diameter D as in the following equation:

$$U = kB\bar{v}D \tag{1.5}$$

where k is a proportional constant. The constant-strength magnetic field is generated by two field coils, one on either side of the measuring pipe. The induced voltage by the flowing fluid through the magnetic field is then detected by two measuring electrodes on the inside wall of the pipe. The electrodes are at right angles to the coils, as depicted in Fig. 1.3. The magnetic field is generated by a pulsed direct current with alternating polarity. This ensures a stable zero point and makes the measurement insensitive to influences from multiphase or inhomogeneous liquids or low conductivity. Electromagnetic flow meters can measure difficult and corrosive liquids and slurries flow in both directions with equal accuracy.
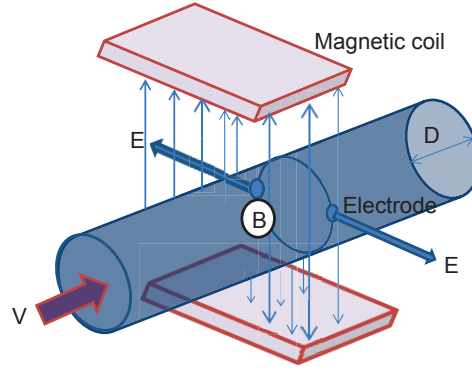
Figure 1.3: Representation of electromagnetic principle

1.1.1.3 Ultrasonic Flow Sensors

There are two basic techniques: Doppler type and time-of-flight ultrasonic flow meters. Doppler ultrasonic meters uses the Doppler effect to detect and measure flow in a pipe. When an acoustic wave of a known frequency is reflected from a moving object, the change in frequency of the reflected beam is proportional to the speed of the moving object. The second technique works by the difference of time between sound waves emitted by two transducers located in opposite directions of the pipe; shown in Fig. 1.4. In this figure the transducers A and B emit and receive short ultrasonic pulses through the fluid flowing in the pipe. A pulse traveling in the flow direction from A to B needs a transit time of:

$$t_{AB} = \frac{D}{sin\alpha} \cdot \frac{1}{C + vcos\alpha} \tag{1.6}$$

where C is the sound speed in the fluid, v is the fluid velocity to be determined, D is the pipe diameter, and α is angle of sonic transmission. A pulse traveling against the current from B to A needs a transit time of:

$$t_{BA} = \frac{D}{sin\alpha} \cdot \frac{1}{C - vcos\alpha} \tag{1.7}$$

The time difference between the two pulses becomes:

$$\Delta t = t_{BA} - t_{AB} = v \cdot \frac{t_{BA} \cdot t_{AB} \cdot sin(2\alpha)}{D} \tag{1.8}$$

From these equations we can determine the mean velocity of the fluid v, the flow

rate of the fluid Q (assuming circular section of the pipe), and the sound speed in the fluid C as in the following equations:

$$v = \frac{D}{sin(2\alpha)} \cdot \frac{\Delta t}{t_{BA} \cdot t_{AB}} \tag{1.9}$$

$$Q = \frac{\pi \cdot D^3}{4 \cdot sin(2\alpha)} \cdot \frac{\Delta t}{t_{BA} \cdot t_{AB}} \tag{1.10}$$

$$C = \frac{2D}{sin\alpha} \cdot \frac{1}{t_{BA} + t_{AB}} \tag{1.11}$$
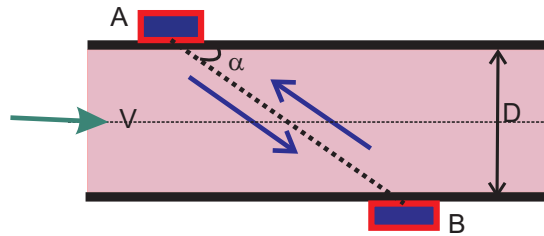
Figure 1.4: Representation of time-of-flight ultrasonic principle

1.1.1.4 Coriolis Flow Sensors

The first description of this principle was established by Coriolis (1792-1843). If a body rotates or vibrates about a fixed position then Coriolis forces are generated when this body undergoes a change of position relative to the fixed one. Coriolis mass flow-meter uses the Coriolis Effect to measure the amount of mass moving through a tube. A Coriolis measuring system is of symmetrical design and consists of one or two measuring tubes, either straight or U-shaped as in Fig. 1.5. Coriolis forces F_c are generated in oscillating systems when a liquid or a gas moves away from or towards an axis of oscillation. In Fig. 1.5 when there is no flow in the tube, the Coriolis force does not exist. However, when there is fluid flow Coriolis force F_c is generated from the fluid particles which are accelerated between the points AC and decelerated between the points CB. This generated force produces a slight distortion of the measuring tube directly proportional to the mass flow rate. The distortion, which is expressed by a phase shift $\Delta\varphi$, is picked up by special sensors. Coriolis flow meters are used in many areas of industry where it is useful to measure mass flow, such as the food industry. It is common that food products are packaged by weight not volume; direct measurement with Coriolis mass flow-meters provides mass flow, density, volume and temperature.
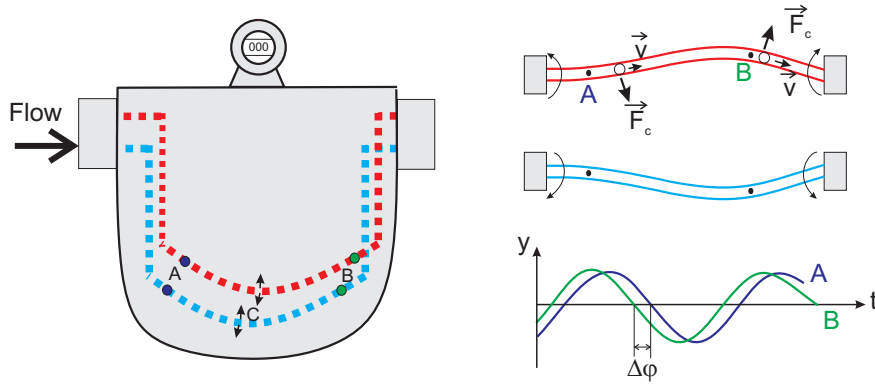
Figure 1.5: Representation of Coriolis flow meter principle

1.1.1.5 Thermal Flow Sensors

The thermal flow meters principle is based on the use of heat in flow measurement. These meters introduce heat into the flow fluid and measure the amount of dissipated heat by means of temperature sensors. There are two methods to measure this dissipated heat: the constant temperature difference method and the constant power method. In the first method, at least two temperature sensors are needed. One is a heated sensor and the other measures the fluid temperature. According to the required power to maintain a constant temperature difference between the two sensors, the flow rate is computed. In the constant power method, the power used to the heated sensor is kept constant. Flow is therefore a function of the difference between the two temperature sensors. Fig. 1.6 shows a representation of thermal flow meter in a pipe, HT sensor is the heated temperature sensor and T sensor is the temperature sensor.
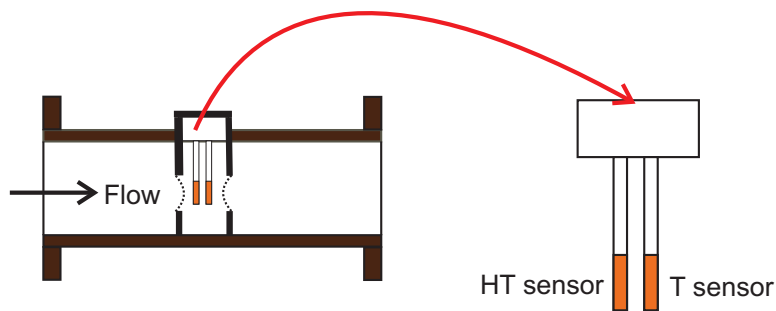
Figure 1.6: Representation of thermal flow meter

In the micromachined flow sensors area, thermal flow sensors make up the largest number of sensors described in literature [Haas08]. They are also the oldest type of micromachined flow sensors, evolved from the integrated circuits, with which the observation of the air cooling of a simple heated resistor is sufficient to obtain a measurement of the flow.

Thermal flow meters are more sensitive than other types and have a broad dynamic range. The major advantages of these sensors are the fast response, the ability to measure very low flow rates, the batch fabrication which means very low cost per sensor chip and the absence of moving components. If a small diameter of tubing is required, as in automotive, aeronautic and medical applications, sensors with moving components become mechanically impractical. In these applications, thermal transport sensors are indispensable. They are used in some additional applications such as combustion air; fuel gas; natural gas distribution; food processing; heating, ventilation and air conditioning [Oli99]. In automotive application for example, "sensors based on a thermal heat-loss principle, including a hot-wire element are mounted in a bypass channel of the air intake to measure mass air flow into an engine" [Flem01]. In the medical field, the respiration disturbances related to some cardiovascular diseases are a supplementary risk for the cardiovascular system. They require urgent diagnostic assessment and consistent therapeutic measures. Thermal flow sensors satisfy such specific requirements of high dynamic flow range and fast response time in controlling the patient's respiration [Hed10].

There are three different principles that are based on the dissipation of heat to a fluid; they are the anemometers, calorimetric flow sensors and time-of-flight flow sensors. In the anemometers case the flow is measured by its cooling effect on a heated entity, anemometers called also hot-wire, hot-chip, or hot-film anemometers depending on the heated element. For calometric sensors, two temperature sensors are placed upstream and down stream of the heater separated from the heated element but still within the thermal boundary layer of the heated body. By such setup both the heating effect of the flow and the flow direction can be measured. Time-of-flight flow sensors measure the time needed by a thermal pulse to reach the temperature sensors placed outside the boundary layer of the heater [Asha09].

1.1.2 Choice of Thermal Flow Sensors

From the wide range of flow sensors described in sec. 1.1.1 very limited options are adequate to our particular application. We performed investigations regarding the requirements of the suitable sensors that can be used in the container as described in sec. 5.1. Briefly, such sensors should be very accurate for the low flow range below 10 m/s. They should have very small size to be installed in very narrow gaps (dimensions of few centimeters). They should also have a robust cover that bears sudden shocks. Additionally, these sensors should be capable to perform wireless measurements. Once they are installed and the container door is closed it is not possible to reach them until the container is discharged. The previous conditions lead us to think about thermal micro-flow sensors as suitable candidates. These sensors are very sensitive for the low flow range; they are very small and can be used for wireless measurements. Since there are no available airflow sensors for such measurements at the market, we had to construct our own sensors. IMSAS has already developed thermal flow microsensors a few years ago, but to use them in

our application they need to be characterised, calibrated and then integrated into the wireless measurement system.

1.1.2.1 IMSAS Flow Micro-sensor

Thermal flow micro-sensors developed by IMSAS consist of a heater and two thermopiles as temperature sensors. The thermopiles are embedded in a low stress silicon nitride membrane, which is $1 \times 1~mm^2$ in dimensions and 600 nm in thickness. The heater is made of tungsten-titanium whereas the thermopiles are made of a combination of polycrystalline silicon and tungsten-titanium. Fig. 1.7 depicts an example of these sensors. The sensing principle is straightforward: as the heater receives power it generates heat that is distributed uniformly in all directions. In a stagnant case, where no airflow passes through the sensor, both thermopiles receive similar amount of heat and then produce similar output voltages. However, when there is airflow, part of the generated heat is convected by the air current in the flow direction. As a result, a difference between up- and downstream thermopiles is detected. This difference is related to the flow value and is the intersection characterising by the sensor.

Thin-film thermopiles are not only used in thermal flow sensors, but also in many other fields such as infrared detectors [Graf07] and thermoelectric gas sensors. A thermopile as a temperature sensor that measures the difference in temperature between two specified points. Their functionality is based on the Seebeck effect[Herw86] where the resulting thermopower is proportional to the difference in temperature between the two junctions. In the flow sensors and Infra-red detectors cases, the hot junction is placed on a membrane for thermal isolation close to the heater. Whereas the cold junction is placed on the bulk material acting as a heat sink.
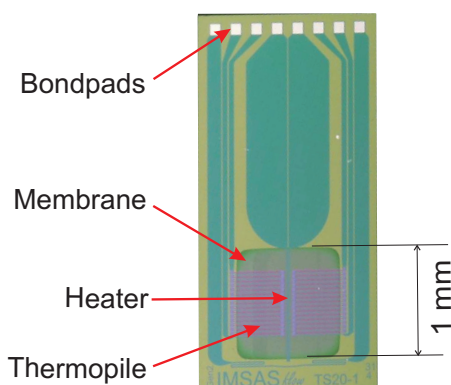
Figure 1.7: IMSAS flow microsensor

1.1.2.2 Thermopiles

The Seebeck effect discovered in 1821 by Thomas Seebeck is the principle on which thermocouple and thermopiles work. Regarding this effect an electric current will flow in a closed circuit composed of two dissimilar metallic conductors forming two junctions when these two junctions are kept at different temperatures. It was found that this happens only with two different conductors (thermocouple). The electromotive force being evoked in an open circuit is called Seebeck voltage U_{AB}, it is proportional to the differential temperature ΔT between the two junctions [Weck97]:

$$U_{AB} = S_{AB} \cdot \Delta T \tag{1.12}$$

where S_{AB} is the Seebeck coefficient, expressed commonly as µV/K, is dependent on the choice of materials. Fig. 1.8 illustrates this effect. In Fig. 1.8 two conductors called thermoelements A and B create the circuit which forms the thermocouple. Seebeck coefficient is assigned according to the potential difference related in sign to the change in temperature. However, working with absolute value is more convenient. In this case the Seebeck coefficient magnitude is calculated as the absolute value of the difference between the Seebeck coefficients of each conductor with respect to platinum:

$$S_{AB} = |S_A - S_B| \tag{1.13}$$

where S_A and S_B are the Seebeck coefficients compared to platinum for the conductors A and B, respectively.
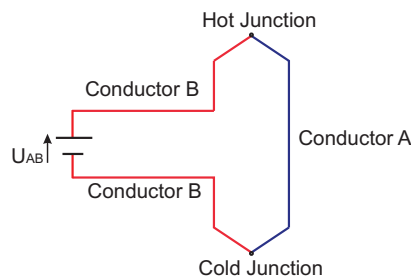
Figure 1.8: Schematic representation of the Seebeck effect

The electromotive force produced in an open circuit operation is usually low, on the order of 10 µV/K for a single junction pair. In the interest of increasing the output voltage it is possible to connect several junction pairs in series. The output voltage (U) is then increased n times with n the number of thermocouple junction pairs connected in series and such a device is called a thermopile.

$$U = n \cdot S(T) \cdot \Delta T \tag{1.14}$$

Thermopile as shown in Fig. 1.9 is formed by a number of thermocouples connected in series and consist of alternate material A and B which are placed between a heat source and a heat sink. The active junction in high temperature surroundings produces an electromotive force at the leads and comes into thermal equilibrium. As a result thermal energy is converted into electrical energy. The remaining energy absorbed by the hot junction is then conducted to the heat sink at the cold junction. When a thermopile is used, the active junction is placed near the heat source. The difference in temperature between the active and cold junctions is transformed into output voltage through the Seebeck effect. In most practical implementations, other thermoelectric effects, (e.g. Joule, Peltier and Thomson effects can be neglected as the input impedance of the signal-conditioning circuit is high enough to ensure that a negligible current flows through the thermopile [Weck97].
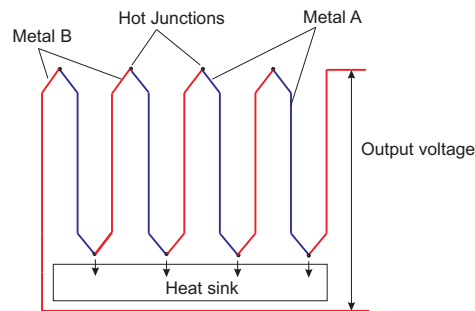
Figure 1.9: Schematic representation of a thermopile

MEMS technology can realise a high grade of miniaturisation of silicon based thermopiles due to the fact that the Seebeck coefficient is dependent on the materials and not the size of junction area. Consequently, very small thermopile structures with low thermal capacitance values and fast response times can be accomplished. IMSAS flow sensors use thermopiles consisting of polysilicon and tungsten–titanium (WTi). Polysilicon is chosen because of its high Seebeck coefficient, whereas tungsten–titanium is used as a metallisation layer allowing a LPCVD[1] passivation of silicon nitride with superior film quality.

1.1.2.3 Fabrication Process

"The sensors are fabricated on silicon substrates with 250 nm of thermal oxide. The oxide is needed as an etch stop layer for the DRIE[2] release etch of the membrane. The thickness of the oxide is optimised to provide a safe etch stop, as well as to avoid buckling of the membrane at higher thicknesses because of compressive stress of the thermal oxide. The heater and the thermopiles are embedded between two layers of low stress LPCVD silicon nitride with a tensile stress of 200MPa. Three hundred nanometer in situ p-doped polysilicon used as one thermopile material is

---

[1]Low Pressure Chemical Vapor Deposition
[2]Deep Reactive Ion Etching

structured by a RIE process. WTi (90% W/10% Ti) with a thickness of 200 nm
is used as the second thermopile material and for the heater. Fig. 1.10 shows the
sensor's membrane area with functional structures" [Buch06]
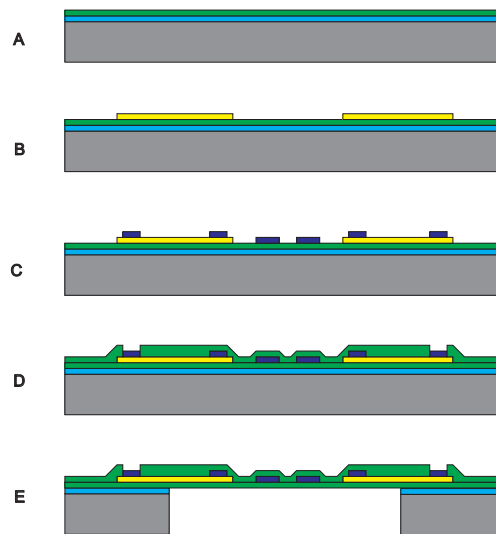
Figure 1.10: Schematic representation of fabrication process of the flow sensor:
(A) thermal oxidation and LPCVD nitride deposition, (B) polysilicon deposition
and structuring, (C) sputtering and etching of WTi, (D) deposition of LPCVD
nitride passivation, (E) DRIE membrane fabrication and optional oxide removal.
[Buch06]

1.2 Airflow Distribution in Enclosed Areas

Controlling air distribution in enclosed areas is a very essential and challenging task.
Enclosed areas in the logistic field include transport containers, warehouses, storage
facilities and others. Airflow distribution should provide the necessary conditions
for maintain the products stored in warehouses in a good quality, or transported by
containers. In such places, air distribution can be driven by different mechanisms;
forced, as by mechanical fan; natural, as by natural convection; or a combination
of the two mechanisms creating a complex indoor airflow characteristics [Zhai07].
Numerical simulations of airflow distribution in enclosed spaces have become a prac-
tical approach due to the increase in performance of high speed computers. These
simulations determine airflow distributions by solving a set of equations describing
the flow and energy. Numerical models can be classified into three different models:
nodal, zonal and computational fluid dynamics (CFD) [Zhan07]. In a nodal model,
the domain is divided into sublayers where flow and energy form a thermal network
by moving between these layers. Flow pattern enables modeling flow rate between
layers. In a zonal model, the enclosed space is divided into zones. Similarly to nodal
model, zonal model requires the flow pattern. It solves conservation equations of

mass and energy and then calculates flow rate between zones by simple correlations for flow and pressure. Both nodal and zonal models have the objective of modeling the airflow as simplified flow network where the governing equations are linear [Zhan07]. The last model is the CFD model; it solves a set of differential transport equations based on the non linear Navier-Stokes equations.

1.2.1 Describing Turbulence

Before defining the selected simulation model, we start by a short introduction to the fluid dynamics to the extent of describing fluid motions. The velocity and pressure distributions in the flow of viscous fluid or gas are described by the Navier-Stokes equations. Fluid dynamics equations [CFD13-1], momentum equation and mass conservation equation are written in Cartesian tensor notation as:

$$\rho \left[\frac{\partial \tilde{u}_i}{\partial t} + \tilde{u}_j \frac{\partial \tilde{u}_i}{\partial x_j} \right] = -\frac{\partial \tilde{p}}{\partial x_i} + \frac{\partial \tilde{T}_{ij}^{(v)}}{\partial x_j} \tag{1.15}$$

$$\left[\frac{\partial \tilde{\rho}}{\partial t} + \tilde{u}_j \frac{\partial \tilde{\rho}}{\partial x_j} \right] + \tilde{\rho} \frac{\partial \tilde{u}_j}{\partial x_j} = 0 \tag{1.16}$$

where, $\tilde{u}_i$ is the i-component of velocity of the fluid with (i) can take one of the values 1, 2 and 3; $\tilde{p}$ is the static pressure; $\tilde{T}_{ij}^{(\nu)}$ is the viscous stresses and $\tilde{\rho}$ is the fluid density. Equation 1.15 represents then three equations, it is the Newton second law, whereas equation 1.16 is the mass conservation equation. For incompressible fluid, the density is considered constant i.e. its derivation in respect to time is zero:

$$\frac{d\tilde{\rho}}{dt} = \frac{\partial \tilde{\rho}}{\partial t} + \tilde{u}_j \frac{\partial \tilde{\rho}}{\partial x_j} = 0 \tag{1.17}$$

Consequentially, equation 1.16 becomes:

$$\frac{\partial \tilde{u}_j}{\partial x_j} = 0 \tag{1.18}$$

The viscous stresses for incompressible fluid is given by [CFD13-1]:

$$\tilde{T}_{ij}^{(\nu)} = 2\mu \tilde{s}_{ij} \tag{1.19}$$

where $\tilde{s}_{ij}$ is the instantaneous strain rate tensor defined as:

$$\tilde{s}_{ij} = \frac{1}{2}\left[\frac{\partial \tilde{u}_i}{\partial x_j} + \frac{\partial \tilde{u}_j}{\partial x_i}\right] \tag{1.20}$$

Additionally by assuming that the density ρ and the viscosity μ are constants, Equation 1.15 becomes:

$$\left[\frac{\partial \tilde{u}_i}{\partial t} + \tilde{u}_j\frac{\partial \tilde{u}_i}{\partial x_j}\right] = -\frac{1}{\rho}\frac{\partial \tilde{p}}{\partial x_i} + \nu\frac{\partial^2 \tilde{u}_i}{\partial x_j^2} \tag{1.21}$$

where ν is the kinematic viscosity expressed as:

$$\nu = \frac{\mu}{\rho} \tag{1.22}$$

The Navier-Stokes equations are valid for any turbulent flow. They can provide the instantaneous velocity and pressure distributions. However, the fine structure of a turbulent motion is not usually the most interesting part. "The instantaneous quantities are always unsteady and depend strongly on the smallest alterations of the initial and boundary conditions, which are never known precisely" [Karp99]. More interesting are the mean velocity profiles because only such distributions can give a reliable information about main statistical characteristics of a turbulent flow and can be compared with the experimental data. The mean velocity distributions can be obtained from the modified Navier-Stokes equations.

The equations in Reynolds-averaged Navier-Stokes (RANS) turbulence models deal with the mean of the air parameters, providing less complex solutions than the instantaneous value of these parameters. To see this, flow parameters are divided and written in equation 1.15 in two components. The first component is for the mean motion, represented by U_i, P and $T_{ij}^{(\nu)}$ for mean velocity, pressure and viscous stress, respectively. The second component is for the fluctuating motions, represented by u_i, p and $\tau_{ij}^{(\nu)}$ for fluctuating velocity, pressure viscous stress, respectively. These equations become [CFD13-1]:

$$\tilde{u}_i = U_i + u_i \tag{1.23}$$

$$\tilde{p} = P + p \tag{1.24}$$

$$\tilde{T}_{ij}^{\;(\nu)} = T_{ij}^{(\nu)} + \tau_{ij}^{(\nu)} \tag{1.25}$$

Substitution of these last three equations in Equation 1.15 gives:

$$\rho \left[\frac{\partial(U_i + u_i)}{\partial t} + (U_j + u_j)\frac{\partial(U_i + u_i)}{\partial x_j} \right] = -\frac{\partial(P + p)}{\partial x_i} + \frac{\partial(T_{ij}^{(\nu)} + \tau_{ij}^{(\nu)})}{\partial x_j} \tag{1.26}$$

By averaging this equation, a new one is obtained. It expresses momentum conservation for the averaged motion and notices that the average of a fluctuating quantity is zero. That is:

$$\rho \left[\frac{\partial U_i}{\partial t} + U_j\frac{\partial U_i}{\partial x_j} \right] = -\frac{\partial P}{\partial x_i} + \frac{\partial T_{ij}^{(\nu)}}{\partial x_j} - \rho \left\langle u_j\frac{\partial u_i}{\partial x_j} \right\rangle \tag{1.27}$$

The last term in the equation is the remaining fluctuating product that depends on the correlation of the terms inside, in general these correlations are not zero. In similar way the mass conservation equation can be decomposed, by substituting Equation 1.23 into Equation 1.18 it becomes:

$$\frac{\partial(U_j + u_j)}{\partial x_j} = 0 + \frac{\partial u_j}{\partial x_j} = 0 \tag{1.28}$$

The last equation illustrates that, for incompressible flows, the fluctuating motions follow the same form of the mass conservation equation that follow the averaged motions. This comes from the fact that the continuity equation is linear but unfortunately this is not the case for the momentum equation. To rework the remaining fluctuating term in Equation 1.27 Equation 1.28 is multiplied by u_i then averaged, that gives [CFD13-1]:

$$\left\langle u_i\frac{\partial u_j}{\partial x_j} \right\rangle = 0 \tag{1.29}$$

Adding $\left\langle u_j\frac{\partial u_i}{\partial x_j} \right\rangle$ to both sides of Equation 1.29 we obtain :

$$\left\langle u_j\frac{\partial u_i}{\partial x_j} \right\rangle + \left\langle u_i\frac{\partial u_j}{\partial x_j} \right\rangle = \frac{\partial}{\partial x_j} \left\langle u_i u_j \right\rangle \tag{1.30}$$

Substituting this in equation 1.27 gives:

$$\rho \left[\frac{\partial U_i}{\partial t} + U_j \frac{\partial U_i}{\partial x_j} \right] = -\frac{\partial P}{\partial x_i} + \frac{\partial T_{ij}^{(\nu)}}{\partial x_j} - \rho \frac{\partial}{\partial x_j} \langle u_i u_j \rangle \tag{1.31}$$

Rearranging last equation leads to:

$$\rho \left[\frac{\partial U_i}{\partial t} + U_j \frac{\partial U_i}{\partial x_j} \right] = -\frac{\partial P}{\partial x_i} + \frac{\partial}{\partial x_j} [T_{ij}^{(\nu)} - \rho \langle u_i u_j \rangle] \tag{1.32}$$

The fluctuations, or so called largest eddies, play the most important part in any turbulent flow. They have the largest dimensions and the largest velocity and pressure amplitudes [Land87, Brek94]. Therefore, the large eddies influence significantly the mean characteristics of any turbulent flow; especially the mean velocity and pressure distributions. The small eddies have a small influence on the turbulent flow with small velocity and pressure amplitudes. They are regarded as a fine detailed structure superposed on the fundamental large turbulent eddies [Land87, Brek94]. The large eddies derive their kinetic energy from the average motion of the fluid as they have no other source of energy. So their energy space distribution is similar to the distribution in the mean flow. However, a significant portion of the large eddies energy passes to the smaller eddies according to energy cascade and eventually dissipates in the smallest eddies. In different areas of a turbulent flow there is varying numbers of smaller eddies. The generations of smaller eddies is proportional to the degree of turbulence in the flow region. It is clear that the turbulence level is determined by the relative value of the mean velocity. Thus, in a boundary layer, where mean velocity has small values due to the considerable magnitudes of viscous forces, the degree of turbulence is low, i.e. the influence of small eddies is insignificant and energy obtained by the large eddies from mean flow mainly remains within them.

Returning to the fluid dynamics equations, the terms on the right of Equation 1.32 in square brackets expresses the stress. First term, is the viscous stress, whereas the second term, is called the Reynolds stress. It is in fact resulted from fluctuations of the flow motion. The main problem to be solved is how to express the last term containing the fluctuating velocity components as a function of the mean velocity.

CFD predicts turbulent flows through three basic approaches: direct numerical simulation (DNS), large-eddy simulation (LES), and Reynolds-averaged Navier-Stokes (RANS) equations.
DNS solves Navier-Stokes equations without approximation for the whole range of spatial and temporal scales of the turbulence. As a result, DNS requires a very fine grid resolution and very small time steps [Nieu94] leading to an extremely long simulation.

LES corresponds to the three-dimensional, time-dependent equations with the approximation of eliminating the very fine spatial grid and smaller time increments. This consideration comes from the fact that macroscopic structure is characteristic for turbulent flow. Moreover, the large scales of motion are responsible for all transport processes. LES still needs considerable computing time, but also gives detailed information on airflow turbulence.

RANS equations with turbulence models deals with the mean of the air parameters, being more useful than the instantaneous value of the turbulent flow parameters. As a consequence airflow distributions can be quickly predicted. RANS approach evaluates Reynolds-averaged variables for both steady-state and dynamic flows by using different turbulence models. The k-ε model is one of the most common turbulence models belonging to this approach. It is a two equation model, thus it includes two extra transport equations to represent the turbulent properties of the flow. This allows a two equation model to account for history effects like convection and diffusion of turbulent energy. Due to its smaller requirements of computer resources, the RANS approach has become very popular in modeling airflow in closed environments [Zhan07].

1.2.2 k-ε Model

The k-ε model is one of the most common turbulence models belonging to RANS approach. It is a two equation model, that means, it includes two extra transport equations. They are for the two transported variables: the turbulent kinetic energy and the turbulent dissipation. The turbulent kinetic energy (k) determines the energy in the turbulent flow, whereas the turbulent dissipation (ε) determines the scale of the turbulence. This model is appropriate in cases of small pressure gradients and internal flows. However, it is not accurate for problems containing large pressure gradients, such as inlet and compressors problems. The two transport equations for standard k-ε model are [CFD13-2]:

$$\frac{\partial}{\partial t}(\rho k) + \frac{\partial}{\partial x_i}(\rho k u_i) = \frac{\partial}{\partial x_j}\left[(\mu + \frac{\mu_t}{\sigma_k})\frac{\partial k}{\partial x_j}\right] + P_k + P_b - \rho\epsilon + S_k \qquad (1.33)$$

$$\frac{\partial}{\partial t}(\rho\epsilon) + \frac{\partial}{\partial x_i}(\rho\epsilon u_i) = \frac{\partial}{\partial x_j}\left[(\mu + \frac{\mu_t}{\sigma_\epsilon})\frac{\partial\epsilon}{\partial x_j}\right] + C_{1\epsilon}\frac{\epsilon}{k}(P_k + C_{3\epsilon}P_b) - C_{2\epsilon}\rho\frac{\epsilon^2}{k} + S_\epsilon \quad (1.34)$$

where μ_t is the turbulent viscosity which modeled as:

$$\mu_t = \rho C_\mu \frac{k^2}{\epsilon} \qquad (1.35)$$

31

P_k is a production of k that is:

$$P_k = -\rho \overline{u_i' u_j'} \frac{\partial u_j}{\partial x_i} \tag{1.36}$$

$$P_k = \mu_t S^2 \tag{1.37}$$

with S is the modulus of the mean rate of strain tensor, defined as:

$$S = \sqrt{2S_{ij}S_{ij}} \tag{1.38}$$

P_b is the effect of buoyancy given as:

$$P_b = \beta \frac{\mu_t}{Pr_t} \frac{\partial T}{\partial x_i} \tag{1.39}$$

where Pr_t is the turbulent Prandtl number for energy (default number is 0.85) with g_i is the component of the gravitational vector in the direction i. β is the coefficient of thermal expansion defined as:

$$\beta = -\frac{1}{\rho} \left(\frac{\partial \rho}{\partial T} \right)_p \tag{1.40}$$

Model constants are the following:

$C_{1\epsilon} = 1.44$, $C_{2\epsilon} = 1.92$, $C_\mu = 0.09$, $\sigma_k = 1.0$, and $\sigma_\epsilon = 1.3$

Practically, when using this simulation model, it is important to specify the boundary conditions like the values at the inlet. It is very difficult to decide the incoming turbulence when it is not known exactly. For this reason, estimating the turbulence model variables, including the turbulent energy and dissipation is a very difficult mission. An easier solution is the thinking of determining other variables like the incoming turbulence intensity (I) and turbulence length scale (l) which are defined as:

$$I = \frac{\sigma}{U} \tag{1.41}$$

where σ is the standard deviation of velocity fluctuations and U is the mean velocity. Knowing the turbulence intensity enables computing the turbulent energy (k), that is:

$$k = \frac{3}{2}(UI)^2 \tag{1.42}$$

The basic guideline to estimate the incoming turbulence intensity is depending on the turbulence case. For low turbulence cases, the turbulence intensity is considered below 1%. In the ventilation flow case, the turbulence intensity is between 1% and 5%. Finally for a high turbulence case, as in heat exchanger, the turbulence intensity is between 5% and 20%.

The second parameter (the turbulence length scale) is a physical quantity that describes the eddies with large energies in the turbulent flow. As a general rule it should not be larger than the dimension of the problem. Estimating the turbulence length scale enables computing the turbulence dissipation rate, ϵ, as:

$$\epsilon = C_\mu \frac{k^{\frac{3}{2}}}{l} \tag{1.43}$$

where C_μ is a model constant, its value is usually 0.09. In practice, l is estimated to be 5% of the channel height in inlet cases. Whereas, it is estimated to be in the order of the size of the grid bars in grid generated turbulence cases [CFD13-2].

2 Modeling of Thermal Sensor Characteristics

2.1 Overview

Modeling of sensor behavior by applying extensive simulations and optimisation tools provides a comprehensive method to evaluate the sensor reactions. Concerning the studied sensor in this research (IMSAS thermal flow sensor) a detailed analytical model was already developed and described in [Sosn]. In that model the thermal behavior of the sensor is described by a one dimensional differential equation. The differential equation calculates the temperature distribution caused by the heater on the membrane. Although this analytical model enables estimating many features of the sensors such as thermal boundary layer thickness and measuring range, it has limitation for some specific phenomenon like the response time of the sensor. For this reason we developed a simple model that focuses especially on the response time feature of the sensor. Response time is defined as the time needed by the sensor output signal to reach 63.2% of amplitude due to a change of fluid flow. The new model uses the finite-difference method to solve the heat transfer equations, taking into consideration the transient conduction and convection between the sensor membrane and the surrounding fluid. This model evaluates the response time of the sensor and its dependence on fluid velocity and sensor geometry.

The thermal flow sensors considered in this study are those developed by IMSAS [Buch06, Sosn11]. These sensors are based on silicon as substrate material. They consist of a heater and two thermopiles embedded in a silicon nitride membrane, in which the thermopiles are placed symmetrically on both sides of the heater. The heater is made of tungsten-titanium, whereas the thermopiles compile a combination of polycrystalline silicon and tungsten-titanium [Buch06]. The thickness of the membrane is 600 nm and its area is 1 mm × 1 mm. Fig. 2.1 (a) shows an example of the referred thermal flow sensors and (b) depicts a cross section in the sensor membrane area. In case of zero flow, the heater generates heat which is distributed uniformly to both sides and there is no difference in temperature detected between the thermopiles signals. However, if there is a difference in temperature between the two signals, this difference is the value of airflow.

Although there is no established standard method for response time measurements [Sosn11], there are reports about measuring the response time. Some of these reports are: Sosna et al.[Sosn11], Ashauer et al.[Asha09], Kohl et al.[Kohl03] and de
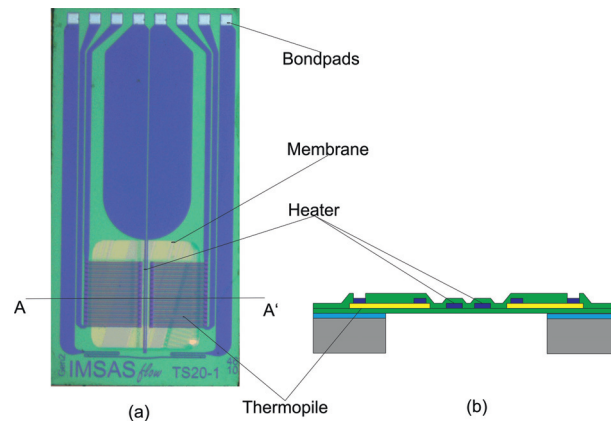
Figure 2.1: (a) An example of IMSAS thermal flow sensors. (b) A cross section according to (AA') of the sensor.

Bree et al.[Bree99]. For example, Sosna et al. investigated methods for measuring the response time of thermal flow sensor via bursting a membrane and an electrical measurement. In the first method, sensors were placed inside a tube closed by an elastic membrane. The tube was filled slowly with air until the membrane breaks; there is a sharp velocity step generated. The disadvantage of this method is the poor reproducibility of the generated flow step. In the electrical measurement method, an electric heating impulse is applied to the sensor heater causing a heat transfer through the membrane. The two thermopiles detect a rising temperature (measured as an electric voltage) that leads to estimating the thermal response time. The disadvantage of Sosna's model is the characterisation of the sensor membrane with one temperature value only, leading to a noticeable difference between the experimental and the model results. The actual work presents a more detailed model in which the membrane is divided into 100 nodes. The temperature of each node is calculated by solving the heat transfer equations through a MATLAB-based modeling program for each time step (1 µs) of the program. Model results meet the experimental results of the response time and provide the sensor output signals (thermopiles) in the steady state case.

2.2 Description of the modeling program

This modeling program uses the numerical analysis approach in the extent of solving heat transfer equations within the sensor membrane and the surrounding fluid. A cross section in the membrane and the air flow channel represents a two dimensional body with uniform thickness in the z-direction. We assume that there is no temperature gradient in that direction. By choosing adequate spacing, the body is divided into a network of nodes. Each node is characterised by a single nodal point at its center as shown in Fig. 2.2. With the assumption that the heat transfer occurs between nodal points only, the partial derivatives of $T(\xi, \tau)$ at the point (ξ, τ) are

given by the forward finite-difference approximations as [Pitt98]:

$$(\frac{\partial T}{\partial \xi})_{\xi,\tau} \approx \frac{1}{\delta \xi}[T(\xi + \delta \xi, \tau) - T(\xi, \tau)] \tag{2.1}$$

$$(\frac{\partial T}{\partial \tau})_{\xi,\tau} \approx \frac{1}{\delta \tau}[T(\xi, \tau + \delta \tau) - T(\xi, \tau)] \tag{2.2}$$

where ξ and τ are independent variables. By definition of the derivative, these approximations become exact as $\delta \xi$ and $\delta \tau$ trend to zero. For the second partial derivatives, the central finite-difference approximation are employed:

$$(\frac{\partial^2 T}{\partial \xi^2})_{\xi,\tau} \approx \frac{1}{(\delta \xi)^2}[T(\xi + \delta \xi, \tau) - 2T(\xi, \tau) + T(\xi - \delta \xi)] \tag{2.3}$$
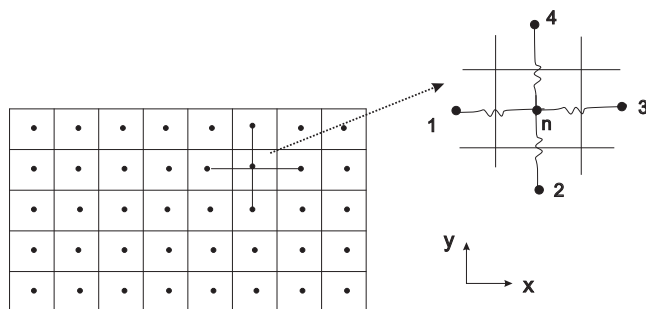
Figure 2.2: Nodal representation of two dimensions body (1, 2, 3 and 4 are the four adjacent nodes to node n).

The formula for the evaluation of temperature in each node based on the explicit Finite-Difference conduction equation[Pitt98] is given by:

$$T_n^{t+1} = T_n^t + \Delta t[\sum_m \frac{T_m^t - T_n^t}{R_{mn}C_n}] \tag{2.4}$$

where m represents all four nodes adjacent to node n in both x and y directions; R_{mn} is the thermal resistance and C_n is the thermal capacitance:

$$R_{mn} = \begin{cases} \frac{\Delta s}{\lambda \cdot A_{k,mn}} & Conduction \\ \frac{1}{\alpha \cdot A_{c,mn}} & Convection \end{cases} \tag{2.5}$$

$$C_n = \rho c V_n \tag{2.6}$$

where Δs is the grid spacing; λ is thermal conductivity; α is the wall heat transfer coefficient; $A_{k,mn}$ is the area for conductive heat transfer between nodes m and n; $A_{c,mn}$ is the area for convective heat transfer between nodes m and n; ρ is the density; c is the specific heat; and V_n is the volume element of node n. The wall heat transfer coefficient is given by:

$$\alpha = Nu \frac{\lambda_{air}}{l} \tag{2.7}$$

where l is the characteristic length and Nu is the Nusselt number. We assume l to be the effective diameter which is defined as:

$$l = 4A/P \tag{2.8}$$

with A the flow cross sectional area, and P the perimeter, respectively. In our case, l is obtained to be 1.2 mm. Nusselt number is given according the following equation [Incr02]:

$$Nu = 0664 \cdot Re^{1/2} \cdot Pr^{1/3} \tag{2.9}$$

where Re is Reynolds number and Pr is Prandtl number. The previous equation is not valid for the stagnant air case; where Nusselt number is a constant independent of Reynolds number, Prandtl number and axial location. This constant value is estimated to be 2 for the chip[Lang90]. By considering the rectangular cross section of the used air channel and by assuming laminar fully developed conditions, the Nusselt number is estimated to be 3.86. The wall heat transfer coefficient is then equal to $97W/m^2 \cdot K$ for the stagnant air case.

2.3 Results and discussion

2.3.1 One Dimensional Model for the Response Time

Firstly, a one-dimensional model is established to obtain the thermal response time of the flow sensor. A cross section of the sensor membrane is divided into 100 nodes as shown in Fig. 2.3. These nodes are equal in dimensions but different in their properties (i.e., thermal conductivity, density and specific heat capacity according to the constituents of each node). This enables us to precisely calculate the thermal resistance and thermal capacitance for the nodes. The values of the constituents' properties are listed in Tab. 2.1. In this model the time varying conduction in between the membrane nodes is considered, as well as the air convection of both membrane sides.
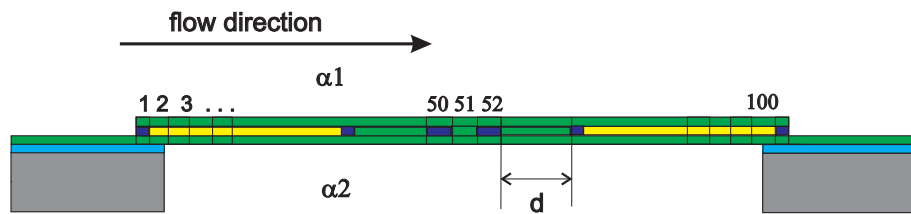
Figure 2.3: Schematic representation of the one dimensional model where a cross section in the membrane is divided into 100 nodes. $\alpha 1$ and $\alpha 2$ are the wall heat transfer coefficients. d is the distance between heater and thermopile.

Table 2.1: Properties of constituent's elements

Element	$\lambda[W/m \cdot K]$	$c_p[J/kg \cdot K]$	$\rho[kg/m^3]$
Titanium	20	530	4500
Tungsten	177	130	19300
Poly-silicon	34	710	2300
Silicon Nitride	4	750	3100
Air	0.03	1006	1.18

Regarding the membrane geometry, two sensor configurations are contemplated: TS20 and TS50. They have the same membrane area ($1 \times 1\ mm^2$), but differ in the distance, d, between the heater and the hot contact of the thermopiles (Fig. 2.3). This distance equals 20 µm for TS20 and 50 µm for the sensor TS50. When a step function is given to the heater, raises its temperature and leads to a heat transfer through the membrane depending on the material's properties and the air velocity. First, a specified value is set for the air flow velocity. The flow goes through an air

channel which is mounted onto the sensor membrane. Then the step function is given to the heater. The temperature of each node is affected by the temperatures of its adjacent nodes, as presented in Equation 2.4. The program calculates and registers the temperature values every 1 µs for all nodes in the membrane, starting from the instance of applying the impulse to the heater. Fig. 2.4 depicts the temperature curves for the thermopile signals for some air velocity values. Response time is then estimated from these curves, corresponding to 63.2% of the stable sensor signal amplitude for the chosen velocity. It is essential to mention that the heat transfer mechanisms for the zero flow case and the one under flow are different. The modeling program differentiate in calculation between the both cases. The comparison here is noted only to show the response time over the whole studied range.
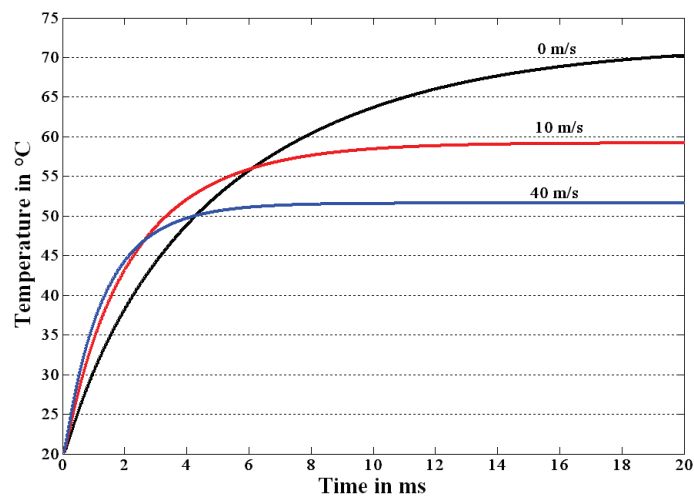
Figure 2.4: Temporal changes of thermal flow sensor signal (thermopile) for different values of air velocities according to the theoretical model. For this 1D model, the direction of the flow is not taken into account and therefore both thermopiles have exactly the same temperature.

The response time of the configuration sensor TS20 (sensor in which the distance heater_thermopile equals 20 µm) is 5 ms in the stagnant air case. However, when airflow is introduced, the time constant decreases to ca. 1.5 ms at air velocity of 44 m/s. As the flow increases the heat transfer between heater and thermopiles rises and the response time is thus reduced. These results are compared with the experimental measurements performed by Sosna et al.[Sosn11] for the same sensor configurations and by applying the same conditions. The comparison shows high agreement between the model and the experimental results. For the low velocity values there are identical results. Aside a slight difference between both results is observed from the velocity 20 m/s and becomes larger as the flow speed increases, as presented in Fig. 2.5. This difference could be explained by two arguments. The first argument is the fact that in Equation 2.9 the flow is assumed to be laminar. Nevertheless, for velocities higher than 30 m/s the flow enters the transition region,

which might cause some errors. The second argument is the fact that heat transfer is assumed to be only in the sensor membrane and the model does not take into account the heat carried by the fluid along the sensor's plane (outside the membrane). The maximum error is less than 0.2 ms for the studied velocity range.
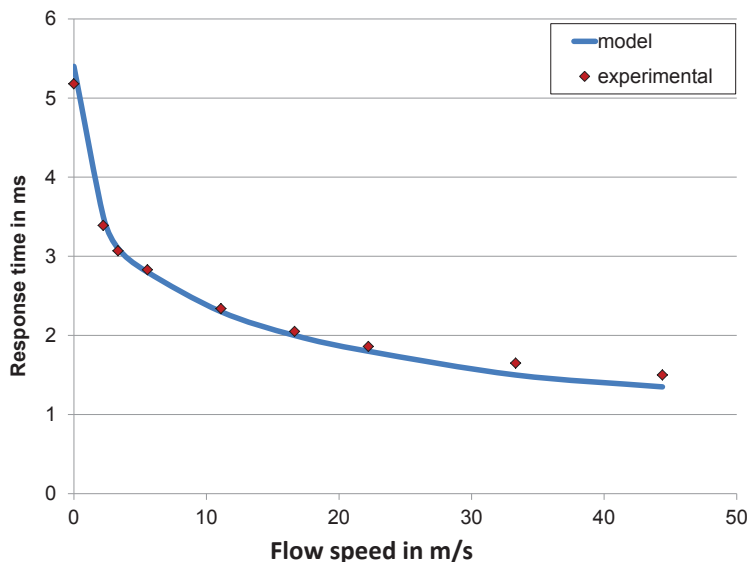
Figure 2.5: Comparison between experimental and model results for flow sensor (TS20) response time. Experimental results from measurements performed by Sosna et al

It is interesting to compare the response time founded by this method with the time of flight (τ). Time of flight is defined as the time needed by air to pass the distance between the heater and the hot contact of the thermopile (d). For the sensor $TS20$: the distance (d) equals 20 µm and by considering the air velocity (v) equals 1 m/s, the time of flight is therefore:

$$\tau = \frac{d}{v} = 20 \text{ µs } \ll 3 \text{ } ms \tag{2.10}$$

Equation 2.10 demonstrates that the time of flight is much smaller than the response time of the sensor. This can be explained by the fact that the response time is composed of several time constants: first, the time constant of the membrane itself and second, the time constant due to the shift of temperature (resulted from velocity change) on the membrane. Reducing the response time of thermal flow sensors is possible by using constant temperature difference electronics. In such mode, the temperature difference between the heater and air around is kept constant, therefore; the sensor's response to a change in flow speed is faster.

Model results also explain the dependence of the response time on the distance between the thermopiles and the heater. The larger the distance, the higher the response time because heat travels further. Fig. 2.6 compares the response times of two sensors: TS20 and TS50.
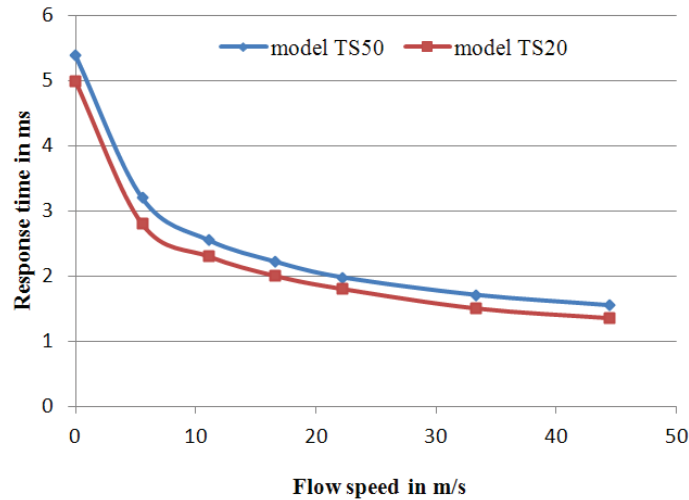
Figure 2.6: Comparison in response time between two sensor configurations TS20 and TS50. The points are model results for some discrete values of velocity and lines are the interpolation from these values.

2.3.2 Two Dimensional Model for the Steady State

A second dimension is added to the previous model, mainly for the steady state case. The new design enables modeling the thermopiles output as a function of flow velocities. The new dimension consists of virtual sublayers of the air flowing over the membrane through the air channel as depicted in Fig. 2.7. In addition, we take into account the conduction among air nodes in both directions x and y, assuming that the air particles flow in straight lines along the air channel.

For each unit of time, the conduction equation is applied to all nodes, and then each virtual air node moves one step in the direction of the flow to replace the next node. This means we can assume for the sake of simplicity that all layers move at the same speed, though in reality the velocity should follow a parabolic pattern. Boundary conditions were taken by considering that heat transfer occurs only in the membrane and the air channel; other surroundings keep the same ambient temperature. This 2D model is used to provide sensor output signals in the steady state case. In this case the velocity was set to values in the range from 0 to 70 m/s. The up- and downstream thermopile signals are extracted, their difference is calculated and the three of them are plotted as a function of the velocity. At zero flow, the two thermopiles give the same signals. As expected, when a flow exists the difference
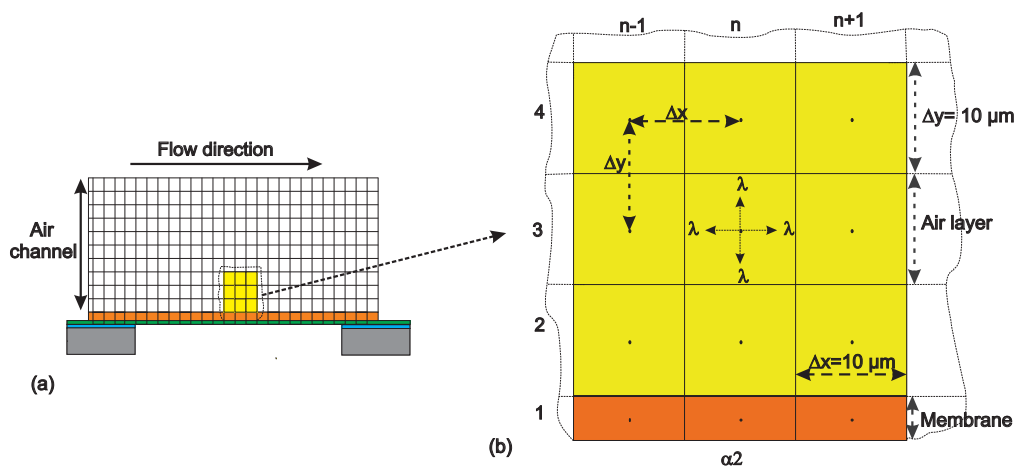
Figure 2.7: (a) Schematic representation of the two dimensions model which is a cross section in the membrane and the air channel. (b) A sample grid, where λ is the thermal conductivity of air and $\alpha2$ is the wall heat transfer coefficient

between the two signals is detected, increasing with the increment of the air velocity [Buch09, Gian07]. Here, the sensor is operating on constant power mode. As a result, when the flow increases, the temperature of the heater decreases due to force convection and leads to a decrease in the thermopiles' signals. Fig. 2.8 shows a comparison between experimental and the 2D model results for sensor signals. Again, the difference in results could be explained by the fact that all layers are assumed to move at the same speed. It is important to note that the homogeneity process of units for both results may generate some errors. Thermopiles' signals are extracted experimentally as voltage whereas program results are produced as temperatures. The Seebeck effect explains the relationship between the output voltage and the temperature difference for the thermopiles. The Seebeck coefficient for the sensor thermopiles is estimated to be 4.3 mV/K [Buch06]. Any deviation from the estimated value causes additional difference between both results.
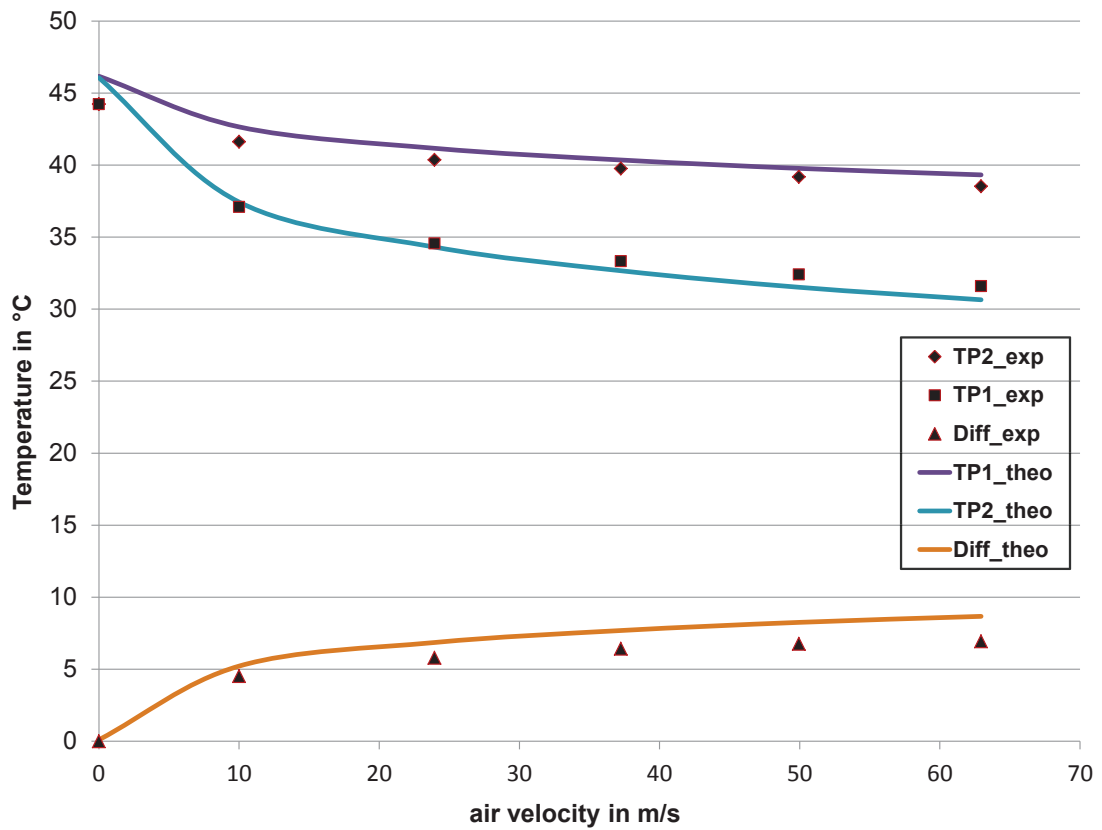
Figure 2.8: Comparison between model and experimental sensor output signals: up- and downstream thermopiles TP1 and TP2 and their differences as functions of air velocity. Solid lines represent model results and dotted lines represent experimental results

3 Characterisation

3.1 Introduction

This chapter introduces an overall characterisation of the thermal flow sensors. Such characterisation is essential to prove their suitability for the intended objective of airflow measurements in logistic containers. Since the maximum airflow velocity inside the container does not exceed 5 m/s, the characterisation study covers this specific range. We do not refer by this assumption to the velocity near the inlet (about 8 m/s). Thermal flow sensors can be characterised by many parameters such as: characteristic curves, responsivity, sensitivity, minimum detectable velocity, response time and others. The response time was already presented in sec. 2.3.1, some other parameters are introduced in the following sections.

3.2 Characteristic Curves

Four sensor configurations are considered in this study TS5, TS10, TS20 and TS50. They have the same membrane area of 1 mm^2 and differ in the distance between heater and thermopiles. This distance is 5 µm for TS5 and 50 µm for TS50. Two flow ranges are studied to separate the linear part of the whole characteristic curve. The ultra-low flow is from 0 to 10 SCCM (standard cubic centimeter per minute) and the low flow is from 10 to 1000 SCCM. They cover the range of air velocity values inside the container which varies from 0 to 5 m/s according to the preliminary investigations. During the characterisation setup, three mass flow controllers (MKS company) are used. Their maximum capacities are: 20, 200 and 1000 SCCM. They are connected through pipes to an air supply source from one side and to the sensor air channel from the other side as shown in Fig. 3.1. These controllers are driven by a control unit MKS through a LabVIEW program. According to this program several mass flow controllers are chosen with adjustable flow steps. The sensor is operated in constant power mode and the two thermopiles' signals are extracted by NI (National Instruments) data acquisition device. The data of the sensor's output with the related flow values are stored in a computer.
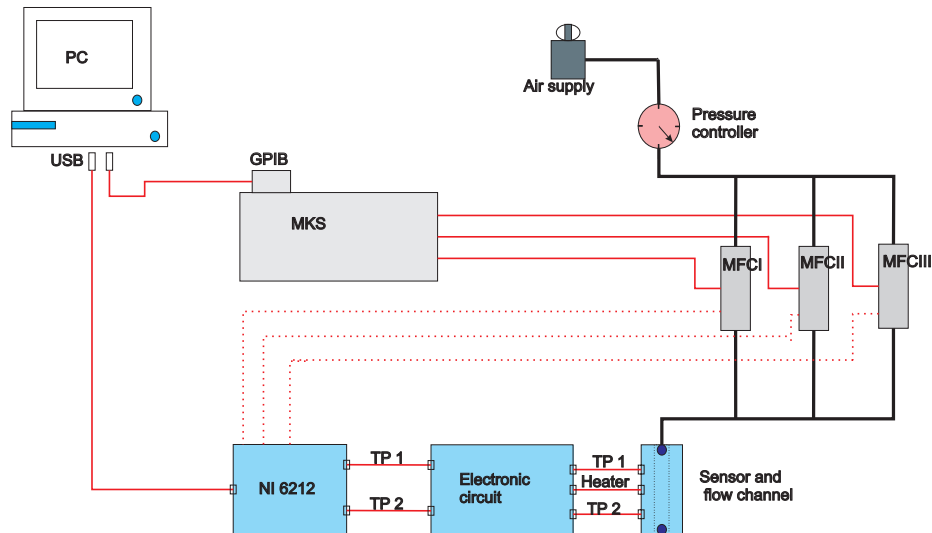
Figure 3.1: Measurement setup for characterisation of thermal flow sensors

3.2.1 Ultra-low Flow Range

In ultra-low flow range, only one mass flow controller (MKS company) is used with maximum capacity of 20 SCCM. By analysing the extracted data, we calculate the output voltage difference. It is the difference between the two thermopile signals as a function of air flow. The resulting curve is called the characteristic curve. We after that compare the curves of the four sensor configurations: TS5, TS10, TS20 and TS50. Fig. 3.2 shows this comparison, demonstrating that the curves are all linear as they are in good agreement with the linear fitting. The R-squared values are all in the range of 0.99. This fact indicates that the fitting degree is very high. We can notice that the sensor sensitivity increases with the distance between the heater and the thermopiles. This gives advantages to select TS50 sensor for future measurements in containers. It is important to mention that these sensors have a small zero offset due to a slight difference between the up- and down- stream thermopiles. When the two thermopiles are perfectly identical, they give the same signal at zero flow, otherwise a small difference between the two signals is noticed, causing the zero offset. To make comparison, the zero offset values are taken into consideration in a way that all curves start from a same point.

3.2.2 Low Flow Range

Secondly, the low-flow case is presented. Here we use 3 mass flow controllers, with the maximum capacities of 20, 200 and 1000 SCCM. The characteristic curves for the four sensor configurations are extracted as in the ultra-low flow case. The output voltage difference starts to increase linearly with the air velocity until a certain limit, where it continues to increase in non-linear way as shown in Fig. 3.3. The function
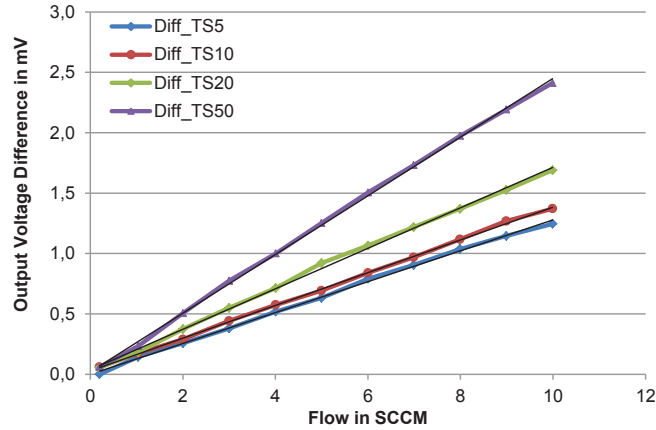
Figure 3.2: Thermopiles output voltage difference as function of flow with the linear fitting for the four sensors configurations TS5, TS10, TS20 and TS50

model that specifies the relationship between air velocity and voltage difference is:

$$\Delta U = a \cdot e^{b \cdot v} + c \cdot e^{d \cdot v} \qquad (3.1)$$

where, ΔU is the output voltage difference of the sensor; v is the air velocity; a, b, c and d are constants to be determined for each sensor configuration. We use the MATLAB based function (fminsearchbnd) to find the suitable fitting curves. Substituting experimental measurement results in the model formula enables estimating the best values of the constants for the best fit. Fig. 3.3 shows the characteristic curves with their fits of the four sensor configurations as function of air velocity. Moreover, Tab. 3.1 depicts the constant values of a, b, c and d in addition to the R-squared values which are very close to 1. These results ensure the suitability of the fitting curves.

Table 3.1: Values of constants for the fitting curves and the R-squared values

Sensor	a	b	c	d	R_seq
TS_05	0.010	0.064	0.010	1.274	0.999
TS_10	0.011	0.065	0.011	1.330	0.998
TS_20	0.014	0.062	0.013	1.328	0.998
TS_50	0.019	0.054	0.018	1.446	0.997

3.3 Responsivity

The responsivity (R) is an important static parameter of the flow sensor. Responsivity measures the input–output gain of a detector system. For a system that responds
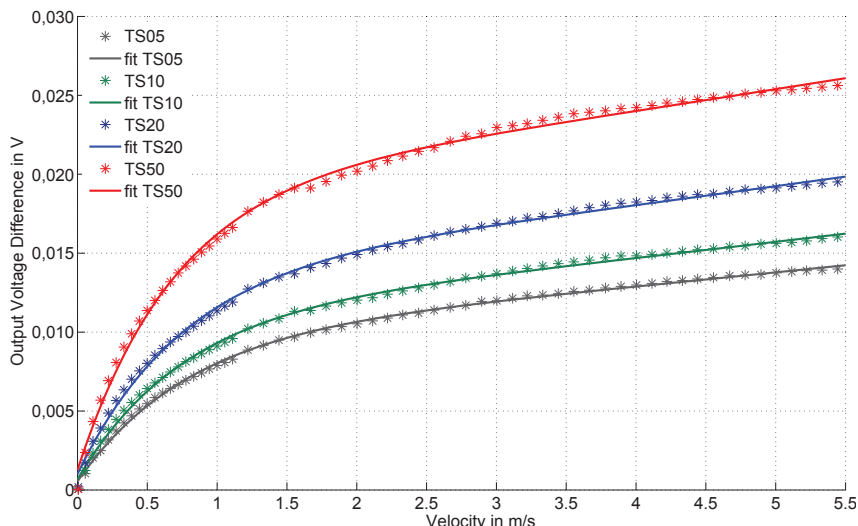
Figure 3.3: Characteristic curves with fits of the four sensor configurations: TS5, TS10, TS20 and TS50. Points are the experimental results with corresponding best-fitted lines.

linearly to its input, there is a unique responsivity. For nonlinear systems, the responsivity is the local slope (derivative)[Busc90]. In case of thermal flow sensors, it is defined for the two thermopiles by the ratio of the sum of their signal to the input power as in the following equation[Kalt99]:

$$R = U_{th}/P_{in} \tag{3.2}$$

where U_{th} is the sum of the two thermopiles signals and P_{in} is the input power. With regard to evaluate the responsivity value, we extract the two signals of the thermopiles for a single flow value of 10 sccm by changing the input power from 1 mW to 7 mW with 1 mW increment. Fig. 3.4 depicts the thermpoiles signals as function of the power. The results show that the sum signal is linear with the input power; i.e. there is a unique responsivity which is the inclination of the line curve. However, responsivity is dependent on the distance between the heater and thermopiles, therefore there is a slight change for the different configurations. The responsitivity value for the studied sensors is in the order of 50 V/W.

3.4 Sensitivity

The sensitivity (S) of a thermal flow sensor is defined as the derivative of the temperature difference with respect to the mass flow rate at a zero flow rate. In other
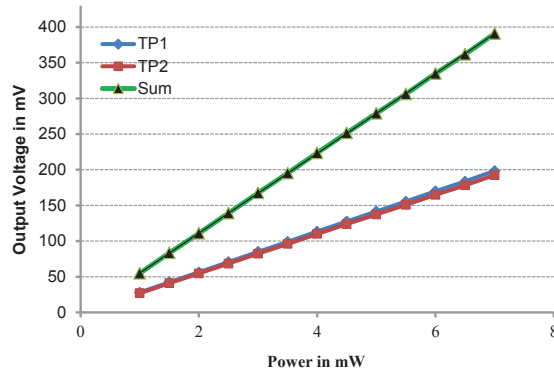
Figure 3.4: Responsivity of the sensor: sum of both thermopiles signals as function of input power

words, the sensitivity is given as the following equation [Kim09]:

$$S = \frac{\partial \Delta T}{\partial v} \Big|_{v=0} \tag{3.3}$$

The relationship between the temperature difference and the output voltage difference of the sensor is described by the Seebeck effect as the temperature is detected by thermopiles, subsequently this relationship is written as:

$$\Delta U = \alpha \cdot \Delta T \tag{3.4}$$

where α is the Seebeck coefficient. Each thermopile in the studied sensors consist of 15 poly silicon and titanium tungsten thermocouples with a thermopower of $4.3\,mV\,K^{-1}$[Buch06]. Equation 3.3 can be rewritten as:

$$S = \frac{1}{\alpha} \frac{\partial U}{\partial v} \Big|_{v=0} \tag{3.5}$$

More details about this parameter in addition to the sensitivity values for the studied sensor are in sec. 3.5

3.5 Minimum Detectable Air Velocity

The minimum detectable flow (MDF) becomes a crucial feature when flow sensors are used in very low-flow applications, including gas detection and accurate supply of

gases in some medical applications [Kuo12, Silv12]. MDF is the minimum flow passing through the sensor which will give a signal (different from noise). It represents a threshold that the flow should exceed to be considered non-zero. This parameter differs from the resolution of the sensor which is defined as the smallest change in a measured quantity which causes a perceptible change in the corresponding indication [IVM08]. MDF is basically influenced by natural (free) convection and thermal noise in the case of thermal flow sensors. Natural convection is a complex mechanism in which the fluid motion is generated by density differences in the fluid due to temperature gradients [Incr02]. The air surrounding the sensor heater receives heat, expands and rises. The cooler air subsequently sinks to replace the warm air. This cooler air is therefore heated and the process continues, forming a convection current. Thermal noise is an electrical noise source caused by random motion of electrical charges in the material. Flow is characterised mainly by Reynolds number (Re). Re is a dimensionless number used in fluid mechanics to study the flow; it represents the ratio of inertial forces to viscous forces in the fluid. Reynolds number depicts different flow regimes, i.e., laminar and turbulent flow. Laminar flow is depicted by a low Reynolds number where viscous forces are dominant and fluid flows in parallel layers with no mixing between the layers. By contrast, turbulent flow occurs when inertial forces are dominant and it is depicted by high Reynolds numbers where eddies, vortices and other flow instabilities are produced. Reynolds number is given by the following equation:

$$Re = v \times L / \nu \tag{3.6}$$

where, v is air velocity; L is the characteristic length and ν is the kinematic viscosity of the air. Free convection is characterised by Grashof number (Gr) expressing the ratio between buoyancy forces due to spatial variation in fluid density (caused by temperature differences) to viscous forces acting on the fluid. It is given as:

$$Gr = \frac{g\beta(T_s - T_\infty)L^3}{\nu^2} \tag{3.7}$$

where g is the local acceleration due to gravity; β is the volumetric thermal expansion coefficient (for an ideal gas, β equals the inverse of the absolute temperature); T_s and T_∞ are temperatures of the surface and the surrounding fluid, respectively; L is the characteristic length and ν is the kinematic viscosity of the fluid. Free convection on a surface depends on several parameters such as geometry, orientation, variation of temperature on the surface and thermo-physical properties of the fluid. In a vertical plate position, the plate is aligned with the gravitational vector and the buoyancy force induces fluid motion in the upward (or downward) direction. However, if the hot plate is horizontal, as in our case, the buoyancy force is normal to the surface and the resulting fluid motion is in the vertical direction. When the temperature difference $(T_s - T_\infty)$ rises, the surrounding air moves and loses heat quickly. However, when the convective flow is established, the heat transfer rises

slightly with increasing temperature difference [Lang90]. The ratio Gr/Re^2 defines the importance of natural convection in respect to a forced convection. This ratio of the buoyancy forces and the inertial forces is expressed as:

$$\frac{Gr}{Re^2} = \frac{gL\beta\triangle T}{\nu^2} \tag{3.8}$$

where g is the local acceleration due to gravity; L is the characteristic length of the hot plate; β is the volumetric thermal expansion coefficient; ΔT is the temperature difference between the heater and surrounding air; and v is the velocity. It is well established that natural convection is negligible when $Gr/Re^2 \ll 1$, forced convection is insignificant when $Gr/Re^2 \gg 1$, and both are significant when $Gr/Re^2 \cong 1$. In the strict sense, a free convection flow is induced by buoyancy forces, if there is no well-defined forced convection velocity and $Gr/Re^2 = \infty$ [Incr02]. In the flow sensor case, a pure free convection may occur when the "forced" flow is zero as depicted in Fig. 3.5(a). However, by increasing the flow, the forced convection increases as well. The free and forced convection enter the mixed convection region where both of them are significant as in Fig. 3.5(b). For higher velocities the contribution of the free convection can be neglected as represented in Fig. 3.5(c).
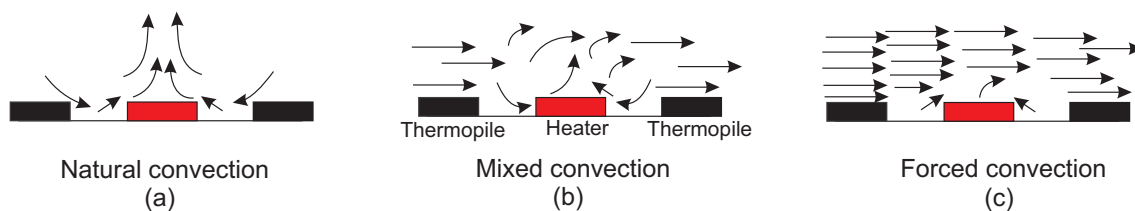
Figure 3.5: Representation of natural, mixed, and forced convection around thermal flow sensor.

Van Putten et al. [Putt99] found that the upper limit on the mixed convective region, (which is defined by the ratio Gr/Re^2), equals [0.3–0.8] for a horizontal hot plate. The method used to generate velocities in the mixed convection region is based on a vertical piston controlled by a computer. It moves back and forth in order to generate the airflow in two opposite directions. A hardware clock in the engine control unit measures the number of rotations of the engine moving the piston. Velocities achieved by this method ranged from 1 to 25 mm/s, 1 mm/s was clearly detected whereas velocities below 0.5 mm/s could not be generated in a reliable way. Cubacku et al. [Cubu10] presented a design of a low power 2D flow sensor. They found that the velocity detection limit is about 5 mm/s, which is in the range of the critical velocity for the transition to the mixed convective flow. Microchannels realised by microfluidic structures were used for measuring very low flow rates, as noted by Buchner et al. [Buch07] and Patsis et al. [Pats12], among others. In the two reports above, water flow was used for the evaluation of the

thermal flow sensors. Liao et al. [Liao13] reported a minimum detectable airflow velocity of 0.2 mm/s by presenting a novel CMOS micromachined capacitive flow sensor for respiratory monitoring. Resolution is also reported in several flow sensors reports. Some examples of the reported resolution values are: 0.1 mm/s in [Asha09], 2 mm/s in [Kaan10], and 0.5 m/s in [Sun07].

3.5.1 Description of the Applied Method

The investigated thermal flow sensor is TS20. An airflow channel is mounted on the sensor PCB in such way that the sensor membrane is located in the middle of the channel (see Fig. 3.6). The air channel has rectangular cross section with dimensions 1.5×2 mm2. The sensor is operated by a constant power circuit providing constant power to the heater during the measurement.
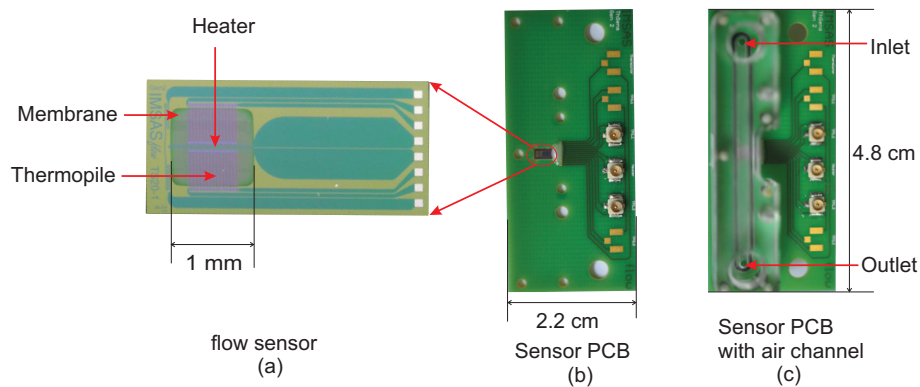
Figure 3.6: (a) IMSAS thermal flow sensor, (b) the sensor within its PCB, and (c) the air channel mounted on the sensor PCB.

In order to measure the sensor MDF, a physical method generating very small flow rates was built. The method principle is based on weighing the mass changes of one bottle partially filled with water during its discharge into another bottle. Mass readings were taken in time increments of 2.5 s in order to calculate the mass flow. Water flows between the two bottles occurs by means of a small pipe, (see Fig. 3.7). In the experiments, we initiate a water flow between two bottles, placed in different height positions, by pushing air into the first bottle. This action forces an equivalent air flow going out from the second bottle. The generated air flow is guided through a pipe to the sensor air-channel. The first bottle is placed on an electronic microbalance (Sartorius company) interfaced to a computer through DAQ NI 6212 device. Balance readings are synchronised with the sensor output voltage difference through the program LabVIEW. Initial conditions have the first bottle as half full with water and the second one as empty. Hence we consider three different cases regarding the height positions of the two bottles, that is, large, moderate and small, respectively. In the first two cases, the first bottle is discharged completely

into the second one, but at different speeds, whereas in the third case, water starts to flow slowly between the two bottles until equilibrium in water level is achieved.
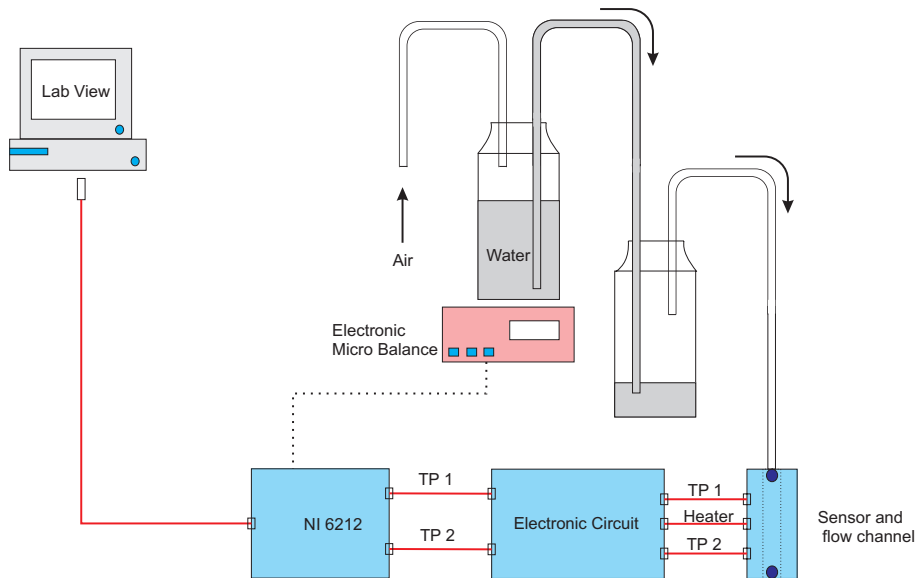
Figure 3.7: Setup for generating very small flow rates. The flow is identified by measuring the water flow rate between two closed bottles.

The accuracy of the calculated flow velocity depends on the accuracy of the balance, which is 0.1 mg. The mass flow is calculated as successive discrete values. Each one represents the mean flow between two successive weighing operations separated by 2.5 s. Thus we have 600 flow values. The accuracy of velocity values, (calculated by substituting the corresponding values of pipe section area and water density), is about 0.03 mm/s. Additionally, the relative errors generated by using the mean velocity value between each two successive weighing operations are less than 5%.

3.5.2 Results and Discussion

The discharging curve in the previous experiments is exponential as shown in Fig. 3.8. This figure compares the equivalent air velocity (left) and the related sensor output voltage difference (right) vs. time. The flow decreases very slowly towards zero. The equivalent air velocity is calculated at 20 °C by assuming that the water density is 998.2 kg/m^3 and the section area of the air channel is 3 mm^2. The resulting curve of velocity (v) as function of time has similar behavior of the sensor output voltage difference (ΔU) as function of time. With a view to obtain the direct relationship between the sensor output voltage difference and air velocity, we modeled both curves by using a MATLAB based program. The resultant fitted curves for the air velocity (in mm/s) and the sensor output voltage difference (in mV), are given

in the following expressions:

$$v = 21.1e^{-0.0014t} - 0.01 \tag{3.9}$$

$$\triangle U = 0.4e^{-0.0014t} + 0.12 \tag{3.10}$$
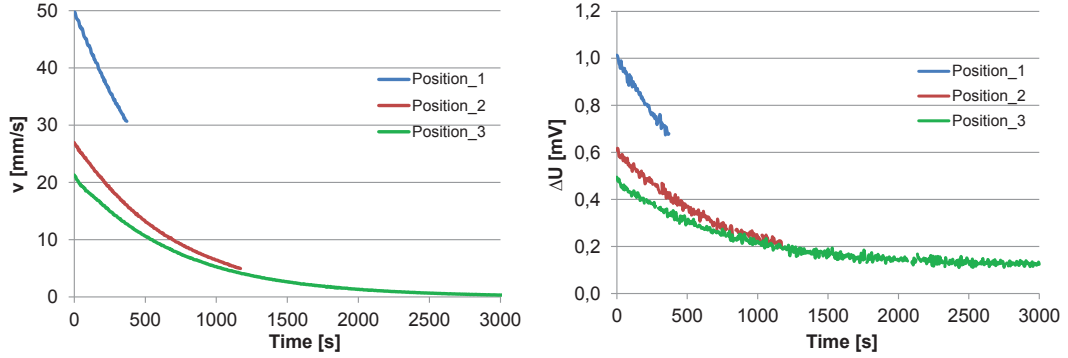
Figure 3.8: (left) Induced air velocities vs. time, (right) the correspondent sensor output voltage differences vs. time for three different positions of both bottles regarding their height difference.

We can obtain the characteristic curve of the sensor in the mixed convention region by eliminating time between the above two equations, which give:

$$\triangle U = 0.017v + 0.12 \tag{3.11}$$

This equation assumes the linear relationship in the mixed convection region. Sensor sensitivity (S) is defined as the derivative of the output voltage difference with respect to the airflow velocity, as in the following equation [Kim09]:

$$S = \partial \Delta U / \partial v \tag{3.12}$$

The sensitivity is then 0.017 V/m/s. Due to the constant time step of extracting data, the experimental data between ΔU and v are plotted in Fig. 3.9. Showing their linear relationship. It also shows that the number of observations in the early part of the curve is very high and then decreases as the velocity increases. When the two bottles are in the vicinity of equilibrium the flow becomes very slow causing the accumulation of data in this region. MDF of the sensor is estimated by two

steps. First, we calculate the deviations of all experimental data from the fitted line and calculate their standard deviation. Second, we divide the resultant standard deviation by the sensor sensitivity. Standard deviation of the experimental data has been calculated from 600 points and is 7 µV. We consider 2σ (representing 95% of the population in a normal distribution). Minimum detectable flow velocity of the sensor by means of this method is therefore:

$$MDF = 2\sigma/S = 0.8\,mm/s \tag{3.13}$$

The relative error by this method is less than 20% for the range from 0 to 5 mm/s; it decreases significantly afterward to less than 10% for the range 5 to 20 mm/s. The larger relative errors for small velocities are due to the high significance of the free convection in heat transfer in addition to the instability of the balance at low values which is another reason for these relatively high errors. By extracting the maximum deviation from the fitted line we found the maximum error to be 0.03 mV. The corresponding error in velocity according to Equation 3.11 is about 1.8 mm/s. This MDF result is in the same order as the results found in the previously mentioned reports [Cubu10, Putt99]. However, it is higher than the one mentioned in [Liao13], where a different sensor principle is used. Eliminating the error caused by the balance in the previous method is possible by evaluating the sensor noise at zero flow where the natural convection is maximum. This was done by a second experiment without flow.
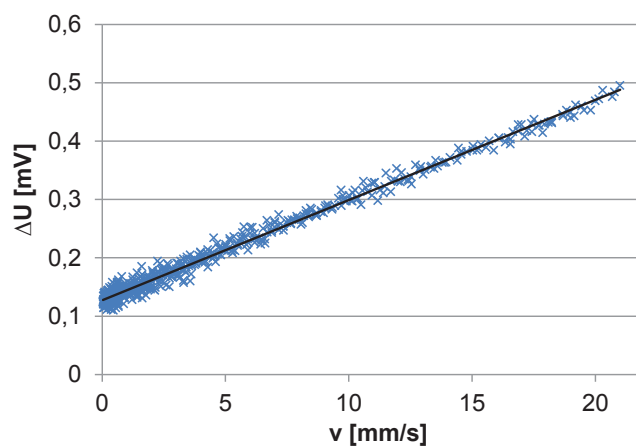
Figure 3.9: Sensor output voltage difference (ΔU) as function of air velocity (v) in the mixed convection region.

Zero Flow Case

Noises on the sensor signals are caused by the sensor itself and by the measurement system. At zero flow, new experiments were done to evaluate the noise level. The

noise of the sensor is mainly caused by thermopiles noises and natural convection. In this case, we can examine pure natural convection together with the thermal noise since there is no defined forced convection, where $Gr/Re^2 = \infty$. Firstly, the thermopile noise is basically the temperature noise and the thermal noise. The temperature noise is caused by temperature fluctuations in the surrounding atmosphere. We assume that this noise has minimal effect on our calculations as all our measurements have been performed at room temperature (20 to 22 °C). Meanwhile, the thermal noise (or the Johnson noise) is an electrical noise source caused by random motion of electrical charges in the material. The Johnson noise is determined by the following equation [John28]:

$$U_{noise} = \sqrt{4k_B T_{ext} R_e \triangle f} \tag{3.14}$$

where k_B is the Boltzmann's constant; T_{ext} is the external temperature; R_e is the electrical serial resistance and Δf is the frequency bandwidth. With $k_B = 1.38066 \times 10^{-23} J/K$; $T_{ext} = 323\,K$; $Re = 200\,K\Omega$; $\Delta f = 1\,Hz$. The thermal noise of the sensor is then $0.06\,\mu V$. Secondly, the main noise source of the measurement system is the Analogue to Digital Convertor (ADC). Since the thermopiles signals are analogue they are converted into digital by ADC with reference voltage of 400 mV and resolution of 16 digits. The root-mean-square quantisation noise (N) is obtained from the following equation [Kest05]:

$$N = q/\sqrt{12} \tag{3.15}$$

where q equals one least significant bit (LSB). The quantisation noise is then $1.76\,\mu V$ which is much higher than the thermal noise of the sensor. Due to the difficulty of estimating the exact participation of the natural convection and other parameters in the measurement system in the total noise, we performed experimental measurement to identify the noise level at zero flow. The sensor output voltage difference (ΔU) at zero flow is extracted for a large number of data through a LabVIEW program. The 1,000 samples with a time increment of 5 s were taken with the heater on. Fig. 3.10 shows the sensor's output voltage difference (ΔU) as function of time. The mean value of the extracted data is $0.12\,mV$ representing the sensor offset, whereas the signal noise expressed as standard deviation (2σ) is about $2.26\,\mu V$. The corresponding air velocity to this noise level is calculated according to the Equation 3.13 and presented in Fig. 3.11:

$$Noise\ equivalent\ velocity\,|_{v=0} = 2\sigma/S = 0.13\ mm/s \tag{3.16}$$

This value represents the theoretical limit for the minimum detectable flow velocity for the studied sensor.
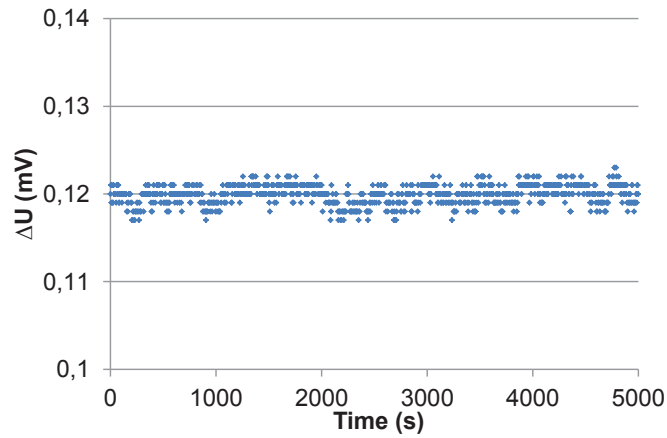
Figure 3.10: Sensor's output voltage difference vs. time in the zero flow case.

The results demonstrate thermal flow sensors' capabilities in detecting very low air velocities by optimising the noise sources. First, the thermal noise of the thermopile is very small since it gives a detection limit of 0.9 µm/s for temperature resolution of 0.1 mK. Second, the natural convection can be minimised by either reducing the characteristic length or reducing the temperature difference between the heater and surrounding air. The first solution requires reducing the sensor dimensions, for example by using narrow and deep air channels, whereas the second solution will decrease the sensor sensitivity and the measuring range. Third, the noise arising from the measurement system can be reduced by optimising the choices of the circuit elements such as ADC with higher resolution. Moreover, the promising results of using microchannels realised by microfluidic structures in providing very accurate measurements for very low flow rates, particularly for liquids, gives motivation to use such structure for airflow as well.
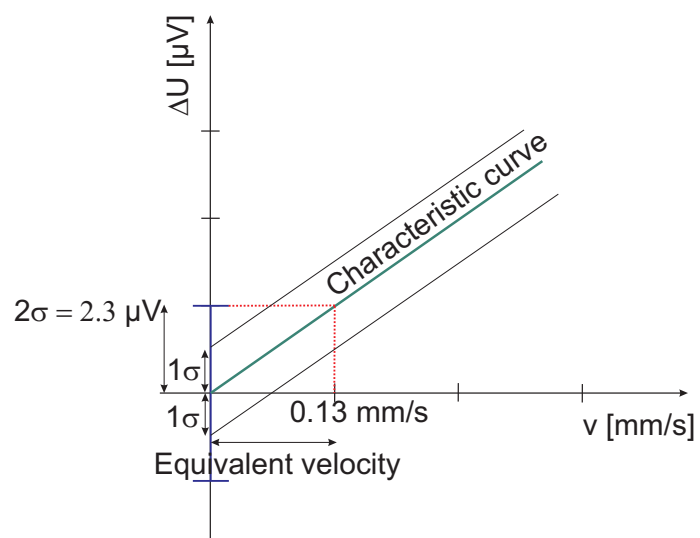
Figure 3.11: Representation of the detection limit of the flow sensor.

4 Calibration

4.1 Introduction

Calibration of flow sensors is crucial for validating sensor readings. However, due to the complexity of performing controlled measurements, calibration is generally difficult. Thermal flow sensors, which are chosen for airflow measurements in reefer containers need to be calibrated. There is a lack of literature about the calibration of these sensors. However, there are many reports about hot wire anemometers calibration, such as Al-Garni [Al-G07] and Özahi et al. [Özah10]. The former reports a method based on moving hot wire probes in stagnant air for low speed values below 1 m/s and the latter reports in situ calibration and rotating disc methods also for low speed values. Further, neither of the above reports mention uncertainty of measurement for the reported methods. In this study a description of a new test device is illustrated in sec. 4.2. After that the calibration method is explained in sec. 4.3. The characterisation and modeling of the sensor results are provided and then the calibration of the sensor is performed. The calibration principle is based on comparing sensor results with those of the reference anemometer. The uncertainty of measurement, yielded from different parameters that influence the measurement results, is evaluated in sec. 4.3.3.

4.2 Description of the calibration test device

The test device consists of a Plexiglas tube of 1.5 m in length and 35 mm in diameter (see Fig. 4.1). The inlet is connected to a mass flow controller (MFC) through a pipe of 10 mm in diameter. From this inlet the air flows through a conic section before entering the tube. At the tube's entrance is a thin regulator, consisting of a plate with many small holes to distribute the airflow uniformly inside the tube. At a distance of 1 m from the inlet a special parallelepiped section is situated to hold the airflow sensor. The sensor is fixed on a special cover of the parallelepiped section. This cover assures that the sensor membrane is placed exactly on the horizontal center line of the tube. A small hole on the cover provides space for the connection wires to connect the sensor signal and power terminals to the constant power circuit outside. A schematic drawing of this test device is depicted in Fig. 4.1. A second cover for the parallelepiped section is designed for the reference anemometer probe. This cover has a hole that allows the insertion of the anemometer probe from the

top and places its sensing probe head exactly in the tube's center. No air leakage
was detected with this design during calibration measurements. In the character-
isation setup, one mass flow controller (MFC in Fig. 4.1) with maximum capacity
of 300 SLM (Standard Liters per Minute) from MKS Company (MKS Instruments,
Germany) is used. It is connected through pipes to an air supply source from one
side and to the inlet of the testbed from the other side as shown in Fig. 4.1. This
controller is driven by the control unit MKS (model: 147C, MKS Instruments, Ger-
many) where a LabVIEW program is used to set the desired flow inside the pipe.
The sensor which is placed inside the pipe detects the changes in the airflow and
its two thermopile's signals are extracted by NI DAQ (National Instruments data
acquisition) device. The sensor output data of the related flow values are stored
in a computer. From the two thermopile signals, we calculate the output voltage
difference as a function of flow. For our application i.e. airflow measurement in
transport containers, air velocity value is of more importance than the flow value.
For this reason we consider it as the basic parameter in this study.
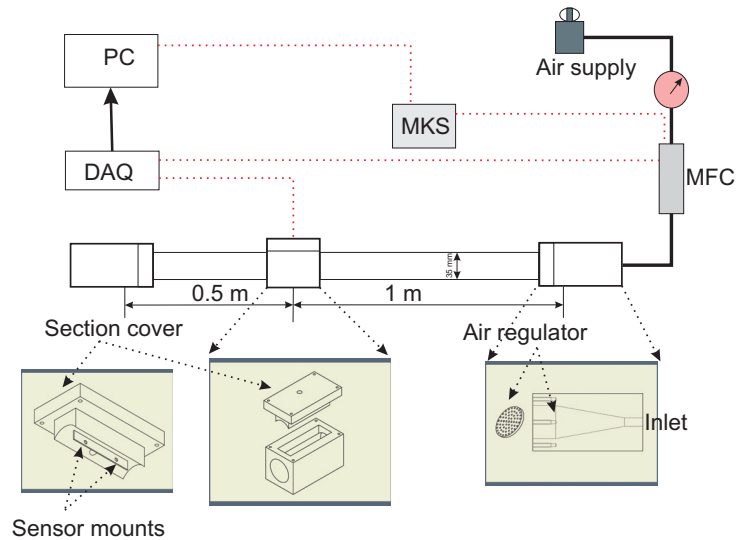
Figure 4.1: Schematic drawing of the manufactured calibration test device.

4.3 Calibration method

To study the flow in the setup, we distinguish between two situations. On the one
hand, flow inside the pipe is depicted mainly by Reynolds number, Re:

$$Re = \rho \cdot v \cdot D/\mu \tag{4.1}$$

where ρ is the air density; v is air velocity; D is the pipe diameter and μ is the
dynamic viscosity of air. Calculations show that for $\rho = 1.1774 \; kg/m^3$ and $\mu =$

$1.8462 \cdot 10^{-5} \, kg/m.s$, Re inside the pipe for air velocities higher than 2 m/s is more than 4000. This value indicates that we have a turbulent flow. Only for the velocity of 1 m/s, the Reynolds number is about 2100. This value is at the laminar flow limit but with the perforated plate acting as a turbulence generator we assume that the flow inside the pipe is turbulent for the whole range. The entry region for fully developed turbulent flow is from 10 to 60 times the diameter[Incr02]. In our case, this distance is about 30 times the diameter.

On the other hand, the boundary layer flow over the sensor is considered as flow over the parallel plate. The position of the sensor is parallel to the flow in the middle of the test tube. In this case, the critical Reynolds number is 60,000 for laminar flow in the boundary layer over the sensor [Lien08, Cubu10].

$$Re(x) = \rho \cdot v \cdot x/\mu \tag{4.2}$$

The distance x from the leading edge of the sensor's PCB is 22 mm. It is the characteristic length in this case. Therefore, the calculated Reynolds number is below 10,000 in all measurement cases and is much smaller than the critical value. The sensor is placed exactly at the center of the pipe, where the air velocity is maximum. In turbulent flow, velocity fluctuates with time in a random fashion. Measurement of velocity at the sensor position in turbulent flow may produce a plot as shown in Fig. 4.2. In Fig. 4.2, the schematic velocity profile for turbulent flow is depicted in (a) and the temporal velocity changes at sensor position in (b). Velocity at the center of the pipe v can be expressed as a mean value $\bar{v}$ plus a random fluctuation component v':

$$v = \bar{v} + v' \tag{4.3}$$

In order to avoid the unpredicted velocity value v', we consider each velocity value as an average of successive readings over a time period T. The period T is assumed to be long enough so that the fluctuations in Equation 4.3 are averaged to zero as shown in Fig. 4.2. T was taken as 1 min with successive reading interval of 2 s.

$$\overline{v'} \,|_T = 0 \tag{4.4}$$

Pressure and temperature have been checked at different flow rates in the test section. Differential pressure was checked by Testo 510 differential pressure device (Testo AG). The maximum pressure difference from the atmospheric one is about 30 mbar at 300 SLM flow. This pressure difference is 13.3 mbar at 200 SLM and 3.25 mbar at 100 SLM. The temperature profile shows very slight changes, (within 1 °C) over the whole range.
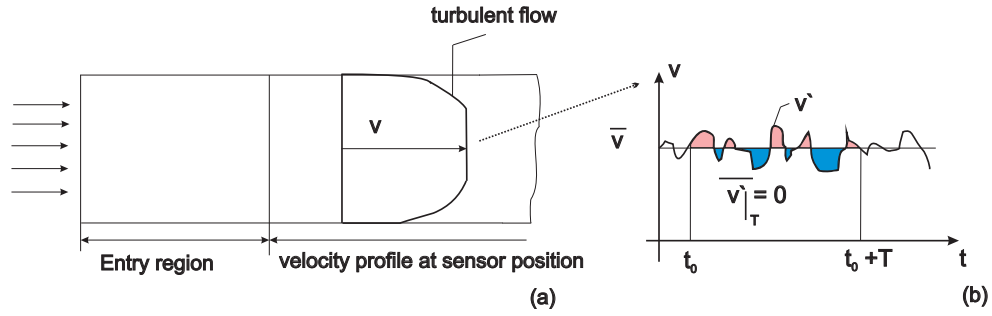
Figure 4.2: (a) Velocity profile inside the pipe, (b) velocity fluctuation with time at the center line region.

The proposed calibration method consists of two steps. First, we characterise the relationship between the air velocity in the pipe and the output voltage of the sensor which is the thermopiles voltage difference. The air velocity is deduced from the air flow, delivered by the mass flow controller to the pipe inlet. Second, we compare sensor readings with air velocity values obtained by the reference anemometer.

4.3.1 Calibration Curves

The relationship between the air velocity v at the pipe center (given in m/s) and the flow F delivered by the mass flow controller (given in SLM) is estimated as:

$$v = \frac{3 \cdot 10^{-3} \cdot F}{2 \cdot 60 \cdot \pi \cdot r^2} \tag{4.5}$$

The experimentally obtained parameters (air velocity and thermopiles voltage difference) are plotted to yield a calibration curve, (refer to sec. 4.2). The function-model that best fits these experimental results, is as follows:

$$\Delta E = a + b \cdot v^c \tag{4.6}$$

where ΔE^1 is the thermopiles voltage difference in mV; v is the air velocity at the sensor position ; a, b, $and\ c$ are constants to be determined for the best fit of experimental results through a MATLAB program. The flow range in these experiments is from 0 to 300 SLM; the entire range is covered with flow increments of 2 SLM. For each flow step, velocity and sensor output voltage are calculated and plotted. Then the MATLAB program determines the constants a, b, $and\ c$ for the best fit. Fig. 4.3 shows the characteristic curve of the sensor where the thermopiles voltage difference

---

[1]ΔE is the thermopiles voltage difference. The notation (ΔE) is used only in this Chapter to avoid confusing with the uncertainty (U) described in this Chapter.

is plotted against the air velocity. The doted curve represents experimental data whereas the continuous curve represents the best fit. This operation is repeated 7 times in several days during one month to check the repeatability of the measurement. For the fitted curve, the mean value of each constant from all tests was adopted. Additionally, the standard deviations are considered for the uncertainty estimation, described in sec. 4.3.3.
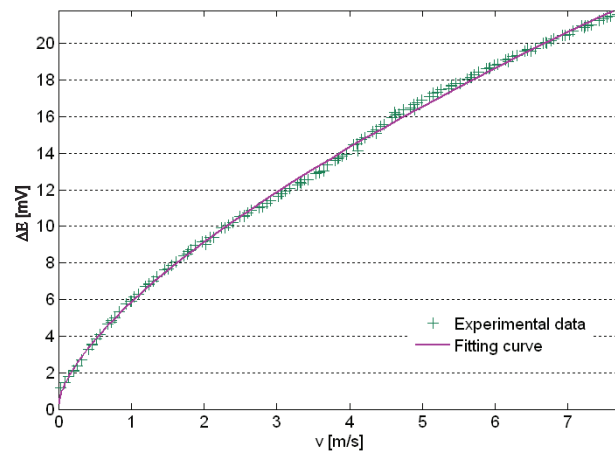
Figure 4.3: Characteristic curve of the sensor where the thermopiles voltage difference is plotted against air velocity for the experimental data and fitted curve

As a result we found the following model:

$$\Delta E = 0.26 + 5.62 \cdot v^{0.66} \tag{4.7}$$

with a R-squared value of 0.99. This value confirms the good model fit. In practice, air velocity is the interesting output parameter as a function of the thermopiles voltage difference. Therefore, the function-model can be rewritten in the following form:

$$v = \alpha + \beta \cdot \Delta E^{\gamma} \tag{4.8}$$

where α, β and γ are constants to be determined for the best fit through the same MATLAB program mentioned above. The sole difference is that, in the first case, the air velocity is considered as a variable and the thermopiles' voltage difference is the output; in the second case the inverse is tested. Fig. 4.4 depicts experimental and fitting characteristic curves where velocity is plotted against thermopiles voltage difference. Previous measurements show:

$$v = -0.01 + 0.07 \cdot \Delta E^{1.53} \tag{4.9}$$

with an R-squared value of 0.998. The latter equation is used as characteristic equation of the sensor. It is also validated by the calibration of the sensor explained in sec. 4.3.2.
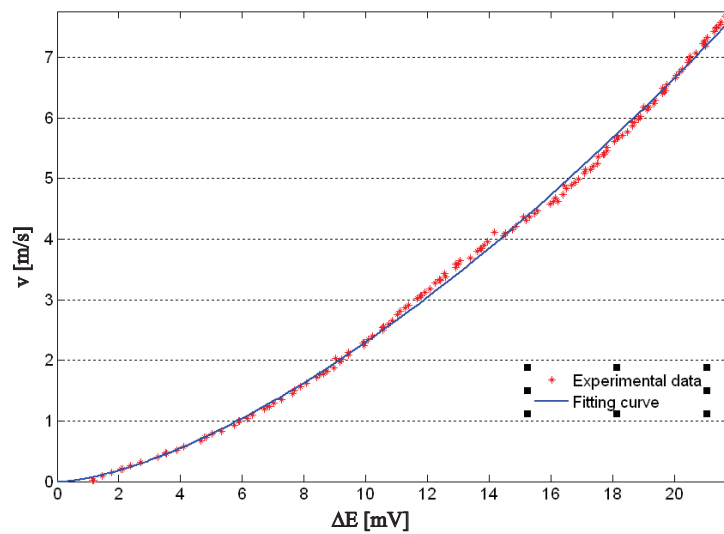
Figure 4.4: Characteristic curve of the sensor where air velocity is plotted against the thermopiles voltage difference for the experimental data and fitting curve.

4.3.2 Comparison with Reference Anemometer

The calibration method described in sec. 4.2, and shown in Fig. 4.1 is used. The calibration method is based on the comparison between the flow sensor and the reference device readings for the flow range from 0 to 300 SLM. The used reference anemometer is the thermo-anemometer VT200 (KIMO Instruments); a calibrated airflow measurement device. The probe of the reference device and the sensor under calibration were placed at the same position alternatively, one at a time. In both cases, the sensing element (membrane of the flow sensor and the probe head of the anemometer) is aligned with the horizontal centre line. The flow inside the tube is controlled by the control unit and the mass flow controller. Sixteen test points are evaluated, starting from 0 SLM with successive flow increment of 20 SLM. Readings of both the flow sensor under calibration and the reference device are registered. This operation is repeated 4 times to check the repeatability. The equivalent velocity of the sensor under calibration is calculated from Equation 4.9. The velocity is a function of the thermopiles voltage difference for the test points. On the other side, the reference anemometer gives the air velocity as a direct output. From the repeated measurements the average values and standard deviations were calculated for results comparison and uncertainty estimation. Fig. 4.5 shows a comparison between the sensor and reference device results. This comparison shows a good agreement between both results; this validates the model given to the sensor output. The maximum difference over the whole calibration range is about 0.2

m/s. The plots, depicted in Fig. 4.5, show a slight overestimation in sensor readings with respect to the values measured by the reference anemometer, in particular for velocities lower than 7 m/s. These slight differences are most likely caused by the estimated function-model in Equation 4.9.
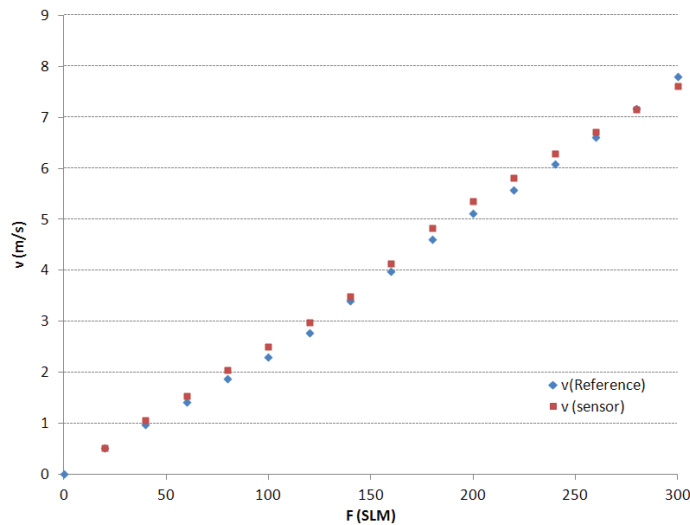
Figure 4.5: Comparison of sensor and reference device readings for different flow values.

4.3.3 Uncertainty Estimation

Uncertainty of measurement is a basic metrological parameter defined by VIM [IVM08] as: "a parameter, associated with the result of a measurement, that characterises the dispersion of the values that could reasonably be attributed to the measurand". It reflects the lack of exact knowledge of the value of the measurand. Quantitatively, uncertainty of a measurand y is calculated by the law of propagation of uncertainty, assuming that all input quantities x_i are independents [JCGM08]:

$$u_c^2 = \sum_{i=1}^{n} (\frac{\partial f}{\partial x_i})^2 u^2(x_i) \tag{4.10}$$

where the measurand, y, is a function dependent on all input quantities x_i by the functional relationship:

$$y = f(x_1, x_2, ..., x_N) \tag{4.11}$$

where $\partial f / \partial x_i$ is the sensitivity coefficient and $u(x_i)$ is the standard uncertainty for the input quantity i. Analysis of the before mentioned calibration method of thermal

flow sensor allows the determination of the parameters or the input quantities that affect measurement uncertainty. These parameters are: function-model formula, mass flow controller, reference, repeatability of measurements and ambient temperature. The functional relationship between the velocity and the input quantities is therefore written as:

$$v_S = v_R + \Delta_r + \delta F + \delta C + \delta T \tag{4.12}$$

where v_S *and* v_R are the sensor and the reference readings, respectively; Δ_r is the difference between the model and the reference readings; δF, δC *and* δT are errors caused by the model-function formula, mass flow controller and temperature changes. As these errors cannot be calculated exactly, their estimate values are considered to be zero and their uncertainties are evaluated in the following bullet points:

- Reference device uncertainty $u(v_R)$
  The reference device has a recent calibration certificate. The uncertainties are provided in the calibration certificate of the device for different air velocity values. In this certificate the coverage factor k = 2, which means that the level of confidence is 95%, as the Gaussian reference distribution is considered. The standard uncertainties are obtained by dividing the given uncertainties by 2 as shown in the following table.

Table 4.1: Certificate and standard uncertainties ($U(v_R)$ and $u(v_R)$)of the reference device for some air velocity values.

v (m/s)	1	2	4	7
$U(v_R)$(m/s)	0.05	0.10	0.12	0.14
$u(v_R)$(m/s)	0.03	0.05	0.06	0.07

- Repeatability uncertainty $u(\Delta_r)$
  The calibration process is repeated 4 times, which enables calculating the uncertainty arising from data dispersion. The mean of the differences between the reference device and the flow sensor under calibration readings is the estimate of Δ_r. The standard deviation of these differences is assumed to be the standard uncertainty of the repeatability for each air velocity specific value, shown in Tab. 4.2.

- Function-model formula uncertainty $u(\delta_F)$
  Constants in the function-model formula (Equation 4.8) are concluded by repetitive measurements, and thus formula's uncertainty must be determined.

Table 4.2: Standard uncertainties of differences between sensor and reference readings.

v (m/s)	1	2	4	7
u(Δ_r)(m/s)	0.03	0.02	0.05	0.14

The formula constants α, β *and* γ are the input quantities in this case. Standard uncertainties for these quantities are their standard deviations, calculated from the repeated measurements described in sec. 4.3.2. The sensitivity factors are obtained by derivation of air velocity in Equation 4.8 in respect to each input quantity α, β, *and* γ, respectively. Sensitivity factors are dependent on the sensor output voltage and are calculated for each velocity value:

$$\frac{\partial v}{\partial \alpha} = 1; \; u(\alpha) = 0.012 \tag{4.13}$$

$$\frac{\partial v}{\partial \beta} = \Delta E^\gamma; \; u(\beta) = 0.001 \tag{4.14}$$

$$\frac{\partial v}{\partial \gamma} = \beta \cdot ln(\Delta E) \cdot \Delta E^\gamma; u(\gamma) = 0.005 \tag{4.15}$$

Applying the uncertainty propagation law (Equation 4.10) for the maximum voltage difference value of the thermopiles allows estimating the formula uncertainty as follows: $u(\delta_F) = 0.18 \, m/s$.

- Mass flow controller uncertainty $u(\delta_C)$
  The used MKS mass flow controller has a maximum capacity of 300 SLM with accuracy of 3% of full scale, including repeatability and pressure coefficient. By associating a uniform distribution function to this value, the standard uncertainty becomes:

$$u(\delta_{C,F}) = \frac{0.03 \cdot 300}{\sqrt{3}} = 5.2 \, SLM \tag{4.16}$$

The sensitivity coefficient is calculated from Equation 4.5. In order to express this uncertainty in m/s, the following calculation is used:

$$\frac{\partial v}{\partial F} = \frac{3 \cdot 10^{-3}}{2 \cdot 60 \cdot \pi \cdot r^2} = 0.0087 \, (\frac{m/s}{SLM}) \tag{4.17}$$

The resultant uncertainty of mass flow controller is then $u(\delta_C) = 0.05 \, m/s$

- Ambient temperature changes uncertainty $u(\delta_T)$

  Temperature changes influence the thermopiles readings as well as the air velocity inside the tube. First, considering the thermopiles voltage difference, a small change in temperature leads to small changes in both thermopiles; hence such influence is negligible. In all cases, measurements were performed at room temperature and only slight changes were detected. Second, the temperature changes effect on the air velocity inside the tube is estimated, using the mass flow controller specifications. The temperature coefficient for this controller is 0.13% of full scale/°C. This uncertainty is calculated in the same way to the mass flow controller uncertainty $u(\delta_C)$ for temperature changes of 10°C.

$$u(\delta_{T,F}) = \frac{0.0013 \cdot 300 \cdot 10}{\sqrt{3}} = 2.3 \; SLM \tag{4.18}$$

$$u(\delta_T) = 0.02 \; m/s \tag{4.19}$$

The combined uncertainty is calculated by using Equation 4.10 for all previous parameters and for each test value as shown in Tab. 4.3. Fig. 4.6 shows the calibration results for the chosen air velocity values with their corresponding uncertainties.

$$u_c(v_S) = \sqrt{u^2(v_R) + u^2(\Delta_r) + u^2(\delta_F) + u^2(\delta_C) + u^2(\delta_T)} \tag{4.20}$$

Table 4.3: Combined uncertainties for some air velocity values.

$v(m/s)$	1	2	4	7
$u_c(v_S)$ (m/s)	0.19	0.20	0.21	0.24

These results show that the maximum uncertainty over the studied range is 0.24 m/s. Such a value is large in respect to the sensor capability, but it is reasonable regarding measurement conditions. where the turbulent flow is dominant. In the real application, the sensor is placed in an open medium where many parameters highly affect its results. For some other applications, uncertainty can be reduced significantly. In such cases a strict control of measurement conditions is required.
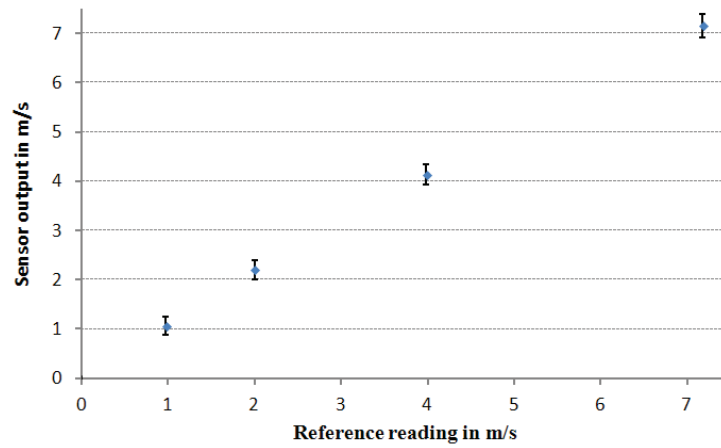
Figure 4.6: Calibration results with uncertainty for the chosen air velocity values.

4.4 Application of the calibration method for different sets of sensors

The concept of the calibration method explained in sec. 4.3, is applied in order to calibrate all thermal flow sensors involved in field tests. These sensors were used to measure airflow in the intelligent container. Details about the sensors and their calibration results are presented in chapter 5.

5 Experimental measurements

This chapter describes the requirements, devices and results of the field tests which took place over the last three years under the Intelligent Container project. Our focus (in this project) was directed only for airflow measurement in the container. This chapter introduces first, different sensors which were used in the measurements. Additionally, it refers to the requirements to prepare a suitable measurement system. Then, it introduces the container and the different pallets distributions which were tested. Concluding this chapter summarises measurement results.

5.1 Sensors and measurement system

Different types of flow sensors were used to measure airflow in the container. These sensors are: hot-wire anemometers, Elbau sensors and IMSAS sensors. All these sensors are working on the thermal principle. The anemometers were used for manual measurements only, whereas the other two were used for wireless measurements.

5.1.1 Hot-wire anemometers

The following anemometers were utilised:

- Thermo-anemometer VT200 (KIMO Instruments), a calibrated airflow measurement device. Its measuring range is divided into two parts: from 0.15 to 3 m/s with resolution of 0.01 m/s and from 3.1 to 30 m/s with resolution of 0.1 m/s.

- Hot-wire anemometer PCE 423, an airflow device suitable for the flow range from 0 to 25 m/s with resolution of 0.01 m/s.

These devices were mainly used in the early investigations of airflow distribution, to provide an idea about air velocity values in different locations of the container. Additionally, they were used in the calibration process. One calibrated anemometer was taken as a reference device to which we compare the readings of the sensors under calibration. Later on they were used in some manual measurements to obtain velocity values at the inlet, outlet and above the pallets levels. These devices are widely available in the market and can be used easily. The main issue regarding their applicability is that they cannot be used wirelessly and have bulky structures. However, they were experimented with one test (Antwerp 2011) by using only three

hot-wire anemometers (type PCE 423). The devices' bodies were placed inside banana boxes, whereas their probes were mounted on the side, inside and top of the boxes. The probes were fixed with duct tape corresponding to the desired direction. These devices have limited memory to store data and they cannot send their data wirelessly, for these reasons we connect them to laptops via USB sticks. Therefore, the connection cables were laid out carefully among or on top of the pallets. This test was useful to determine the challenges and requirements for airflow measurements. Consequently, the main requirements of the sensors that can be used in the container are:

- Sensors with very small sizes can be distributed and fixed in different locations of the container.

- Sensor's body should be robust. During loading, unloading, and transportation sensors might be exposed to high forces.

- Sensors should have high sensitivity in the low flow range. Measurements showed that the air speed inside the container is between 0 and 5 m/s and about 8 m/s in the inlet.

- Sensors should communicate wirelessly. Once the sensors are distributed in and around pallets, it's not possible to reach them unless the container is unloaded.

Previous requirements led us to think about the thermal flow sensors as the best option for this task. They fulfill the first three requirements and are capable to be integrated within the RFID network. Moreover, they need low power consumption. For this reason, attention was directed towards these sensors. First Elbau sensors were tested, followed by IMSAS thermal flow sensors to the extent of achieving accurate measurements.

5.1.2 Elbau sensors

Elbau sensors are thermal flow sensors developed by one of the project partners, Elbau Elektronik Bauelemente GmbH Berlin. These sensors have compact size and can communicate with the base station where a star-shaped network topology was chosen. They send continuous wireless transfers of information to the central base station until the battery power is lost. The calibration curve is linearised in the range 0.4 to 3 m/s in both directions. The characteristic curve is stored in the sensor with order to transmit the same calibrated values. Several field tests were done by using these sensors. They should be distributed around the base stations which are connected to a computer placed outside the container through USB connections. The maximum distance that we were able to receive sensor data from was limited to 1.5 m from the base station in the loaded container. Therefore, the base station was placed on the top of one pallet, data was received from a particular pallets' sensors, but not near the floor. For this reason we arranged two base stations for the ten

available sensors. With these sensors, specific airflow measurements were performed in specific areas of the container, such as around one chimney or one pallet. Very long cables were needed to connect the base station(s) with the laptop(s), which were led through the container door. Computers should not be in sleep mode during the measurements. These sensors were calibrated before and after field tests to counterbalance their performance.

5.1.2.1 Calibration of Elbau sensors

We used a simple method for the calibration process, based on the comparison between both readings of the Elbau sensors and a reference device for a specific flow value. The reference device is a hot-wire anemometer (KIMO VT200). This calibration method is based on the method explained in sec. 4.3.2 [Issa12]. The airflow is controlled by a control unit (MKS) through mass flow controller of 300 SLM. The airflow is guided into a glass pipe with a 62 mm diameter. In the distance of 1 m from the inlet, a small open hole is created on the top part of the pipe. The hole is used to insert the reference probe and an appropriate material is used to prevent any air leakage. We alternatively placed the reference device and the tested sensor in the same place of the pipe, exposed them to 15 successive flow steps of 20 SLM each during equal time interval of 1 min for each flow step. Fig. 5.1 shows a schematic drawing of the calibration setup. The maximum velocity in the middle of the pipe is about 2.6 m/s for 300 SLM. Therefore, this calibration procedure is restricted to this velocity limit. This calibration limit was accepted since the calibration range is defined by the company from 0.4 to 3 m/s.
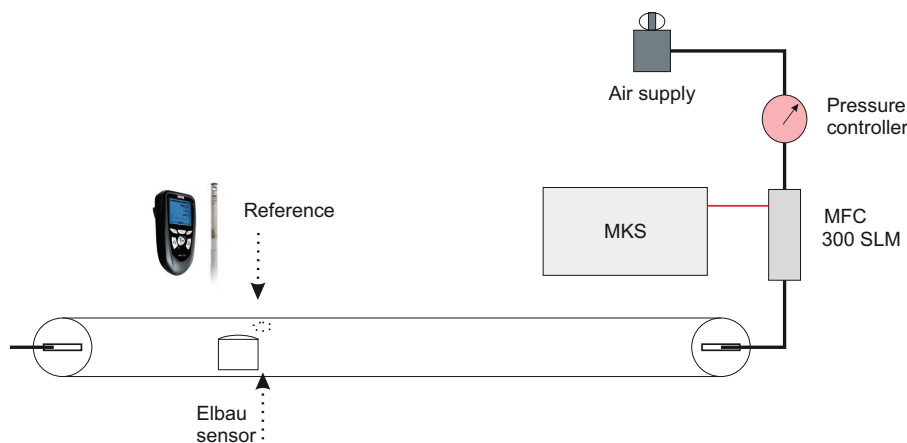
Figure 5.1: Schematic draw of the calibration setup

Two calibrations for these sensors were done, before and after one field test. Eight sensors were involved in these calibrations, assigned by their serial numbers: S1720, s2122, s2124, s2127, s2128, s2129, s2130 and s2131. Fig. 5.2 shows an example of the calibration results; it is for the sensor s1720 and the reference device. There

is therefore a clear difference between both results. The difference error is not a constant but rather an error increases with the increase in flow. Another difference that this sensor has an offset of all data except zero and can be fitted by a linear curve where the R-squared value is 0.99 (Fig. 5.2). The deviation between both results starts by 0.46 m/s at 20 SLM as flow and it reaches to the maximum difference about 1 m/s at 280 SLM. Other sensors have similar behaviour, with maximum error ranging of about 0.5 m/s. However, the maximum error between sensors and reference is about 1.2 m/s. These errors come from the fact that all sensors have the same calibration curve which simplifies getting the results on the one hand, but generates higher errors on the other hand. Fig. 5.3 depicts a comparison between all sensors results and the reference device.
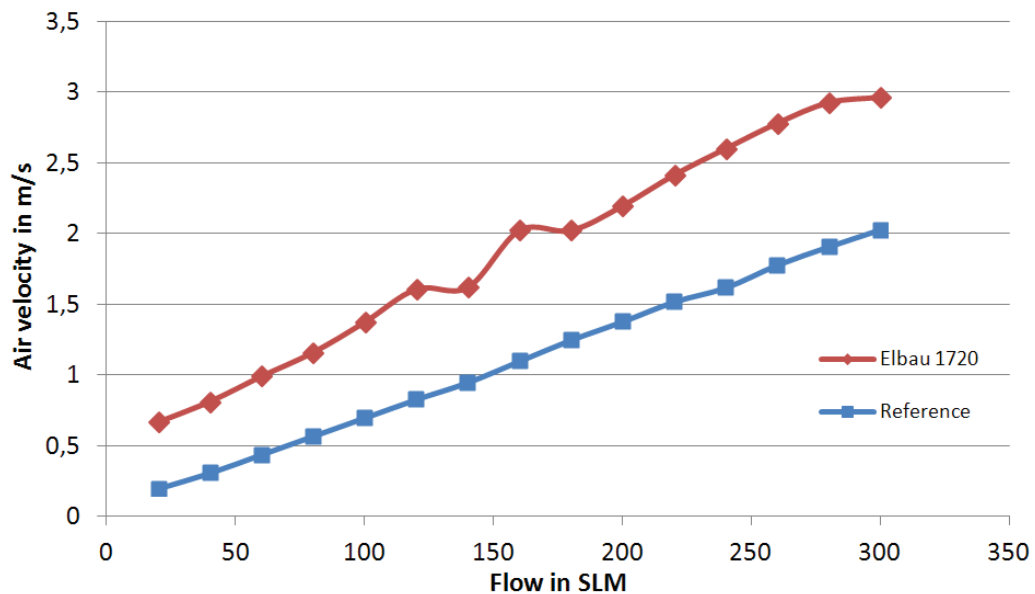
Figure 5.2: a comparison in calibration results between the reference and one Elbau sensor (s1720)

The two calibrations gave similar results with slight differences. Maximum error between the two calibration operations is 0.2 m/s.

5.1.2.2 Evaluation

Manipulating these sensors in logistic containers has advantages such as: the small size fits in small gaps between pallets and walls in different areas of the container. These sensors detect airflow values and send their data wirelessly to a base station located not so far from their locations. All sensors have one calibration curve stored inside the sensors, so the sent data are given as air velocity and don't need any further treatment. These sensors are easily manipulated as they send data continuously until the end of the battery, which is later replaced by the company itself.
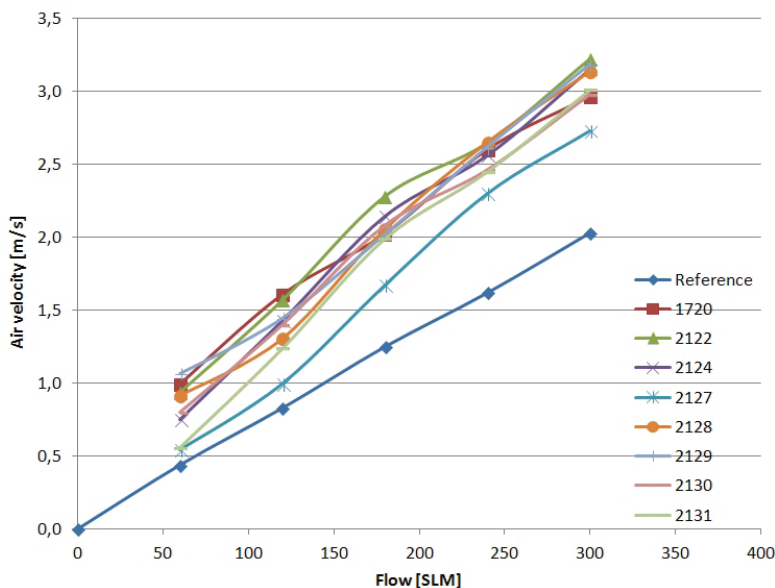
Figure 5.3: a comparison in calibration results between the reference and 8 Elbau sensors

These sensors also have some limitations, due to the limited distance between the sensors and the base station, many places in the container could not be measured. In addition, all sensors should be distributed in a specific area, around one pallet for example. Interfacing the base station with the computers through USB cables is no easy task. Furthermore, the calibration curve does not cover the whole expected range in the container from 0 to 5 m/s. Values less than 0.4 m/s and higher than 3 m/s are not completely accurate.

In the interest of overcoming the mentioned shortages and limitations, we manipulated IMSAS thermal flow sensors.

5.1.3 IMSAS sensors

IMSAS flow sensors were described in sec. 1.1.2.1. These sensors can be integrated into a wireless platform to be used wirelessly. This platform is TelosB which is based on the IEEE 802.15.4 standard [Lloy13]. Within the sensor enclosure (made by 3D printing technology) 4 layers are implemented: thermal flow sensor, constant power circuit, TelosB circuit and battery. Fig. 5.4 shows the flow sensor in (a), the 4 layers in (b) and the complete airflow sensor with its enclosure in (c). A short description of the preparation processes which was performed with a view to get the sensors ready for the measurements follows:
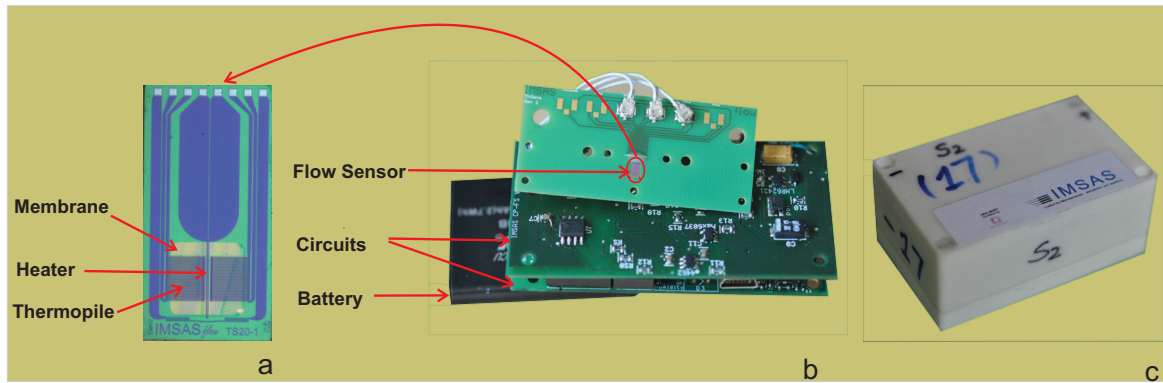
Figure 5.4: (a) is IMSAS thermal flow sensor, (b) is the flow sensor within its PCB connected the circuits, and (c) is airflow sensor that consists of thermal flow sensor and its related circuits

5.1.3.1 Preparing the sensors PCBs

The sensor chip dimensions are: $2{\times}4$ mm, the chip is integrated into a PCB ($1.7{\times}4.8$ mm) where the bonds of the heater and thermopiles are wired. First step is fixing the sensor chip against a light tape and then attaching it to the pre-prepared PCB. On that PCB, there is an empty space which fits the sensor chip. After that, special UV glue already prepared is injected in the corners of the PCB. From the four corners, the glue flows (following the Bernoulli equation) to the gaps between the sensor chip and the edges of the PCB hole. This operation continues until the glue all around the chip was distributed. Observation is done by means of microscope and injection of glue is operated by a special device through a fine needle. Afterwards, the prepared PCBs were exposed to UV in furnace in favour of hardening the glue. Then, the sensors were placed in a solvent to remove the light tapes. These solvents are acetone and then propanol. Sensors are then checked under a microscope for any remaining glue or any other dirty spots on the sensor membrane. The next step is wiring the sensor with its PCB where connectors were added. By means of these connectors the heater is powered and the thermopiles voltages are extracted. Once the sensors are ready, their performance was checked with regard to make sure that they are working properly. After that the resistances were measured of both thermopiles and heater for all sensors. Results show that the heater resistance is about 900 Ω, whereas the thermophile resistance is about 200 kΩ. However, there is a slight difference in resistance values from one sensor to another. This difference between the up- and downstream thermopiles causes an offset at zero flow value because both thermopiles do not display the same output voltage. For this reason we decided to calibrate all sensors and find the specific calibration curve for each sensor. In this way, accurate results were obtained and the errors caused by sensor's differences were reduced.

5.1.3.2 Preparing the sensors circuits

The sensors are operated in constant power mode. In this mode the real power of the sensor is compared to a reference power. The difference between the real and reference powers is maintained in a defined range. A constant power circuit for the thermal flow sensors which are used wirelessly was developed by Lloyd et al. [Lloy13]. This constant power circuit collects the analog sensor signals, where the flow value is represented by a voltage difference in the up- and downstream signals. This voltage difference is proportional to the temperature difference. Additionally, the circuit should adjust the electric energy supply to the heater to implement the constant power. The analog mode is not suitable for wireless sensor node because it consumes too much energy and uses + 9 V supply. Moreover, the digital mode enables making data analysis easily in host computer. For this reason a wireless sensor (TelosB) is used to read the analog signals and convert them into digital signals (see Fig. 5.4(b)). In the digital mode two sensor nodes are involved. The first node controls the constant power method. It obtains the voltage information and feedback for adjustment in the circuit and sends processed data messages to the radio. Second node receives the messages from the radio, then sends them to the serial port connected to the host PC. This node works as a base station between the local control center (first node) and background data analysis center (PC). The TelosB is programmed on its MCU (microcontroller) to implement the function of reading the analog signal from the sensor node [Lloy13].

5.1.3.3 Preparing sensors enclosures

As it was mentioned above, flow sensors which will be used in the container need a robust body. Therefore, sensors' enclosures are not only needed to protect the sensors but also to provide an appropriate housing for the sensors and the electronic parts. For this reason, a robust enclosure was designed taking into consideration the dimensional restrictions. The enclosures were fabricated by 3D printing technology. The designed model was manufactured by the selective laser sintering (SLS) method, which is commonly used in 3D printing. The principle of this method is the fabrication of very thin layers and afterwards assembling them together to obtain the product regardless of the complexity of the design. The SLS 3D printing method is suitable for rapid creation of relatively robust parts that can be used as concept models, functional prototypes or even as end-use parts (as in dentistry and aerospace). Dimensions of the enclosures are $7.3 \times 4.6 \times 3.1$ cm. One enclosure consists of three parts: top cover, middle section and bottom cover (see Fig. 5.4(c)). The flow sensor is fixed into the top cover where there is an integrated airflow channel. O rings are placed between the sensor PCB and enclosure top cover to prevent any leakage from the air channel. In the middle section the constant power circuit connected with TelosB node is placed. Connections between the sensor and its constant power circuit are done through thin cables. The bottom cover is designed for

housing the battery giving the power to circuit through switch. The three sections were initially fabricated separately and they are assembled by means of plastic or metallic screws.

5.1.3.4 Calibration of the sensors

The calibration method is based on the method explained in sec. 4.3.2. It is the same method used for calibration of Elbau sensors with the difference in the mass flow controller. This time, the airflow was controlled by mass flow controller of maximum capacity 1000 SLM. The reference probe and one IMSAS sensor were alternatively placed in the same place of the pipe. They were exposed to 15 successive flow increments of 20 SLM each, at equal time interval of about 1 min for each flow increment, and sensors' readings were then recorded. Fig. 5.5 shows a schematic drawing of the calibration setup. The calibration range is from 0 to 5 m/s covering the expected air velocity values inside the container. The value 5 m/s is achieved by applying flow of 650 SLM from the mass flow controller.
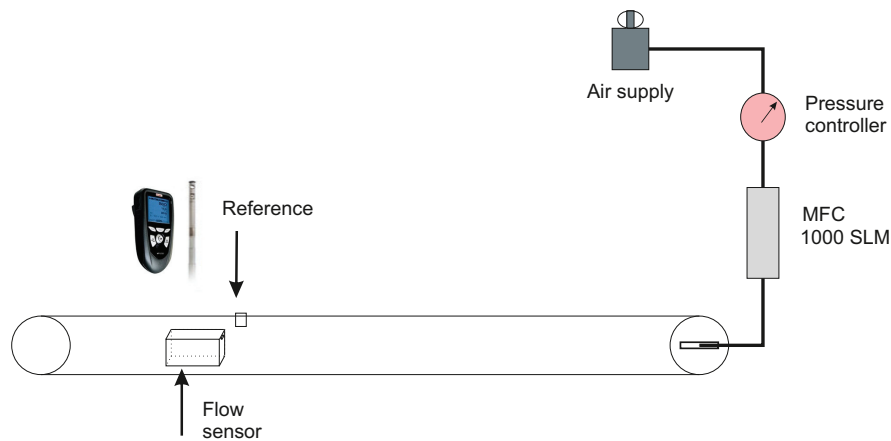
Figure 5.5: Schematic draw of the calibration setup

The calibration procedure is repeated two times for each sensor, one for the positive velocities and the other for the negative ones. The calibration curves were found by means of a based MATLAB fitting program. These curves follow the mathematical model-function:

$$v = a + b \cdot \Delta U^c \tag{5.1}$$

where v is air velocity given in (m/s); ΔU is the sensor output voltage difference given in (V); a, b, and c are constants found by the fitting program for each sensor and for both directions. By this way, each sensor has its own calibration curves, allowing to obtain exact velocity values and consequently avoiding severe errors

resulting from applying one calibration curve for all sensors. 15 sensors where calibrated by this method and were used in field tests. The constants a, b, and c are cited in Tab. 5.1 with the R-squared values for both positive and negative velocities. Fig. 5.6 shows an example of a sensor calibration curve.

Table 5.1: Calibration constants and r-squared values for the calibrated sensors

Sensor	a1	b1	c1	R1	a2	b2	c2	R2
S1	0.513	0.001	8.335	0.98	-3.622	8.845	-1.171	0.97
S2	-1.714	0.245	3.182	0.94	-0.427	5.361	-2.668	0.97
S3	0.438	0.002	7.701	0.98	-0.314	3.446	-2.262	0.98
S4	0.541	0.003	5.307	0.91	49.9	-48.2	0.043	0.96
S5	0.439	0.002	7.495	0.98	0.548	3.720	-4.619	0.96
S6	-1.532	0.284	3.005	0.96	0.126	3.816	-3.138	0.95
S7	-0.346	0.059	4.567	0.99	-2.037	6.497	-1.503	0.99
S8	-1.722	0.242	3.207	0.97	-1.208	6.467	-1.857	0.98
S9	-1.592	0.275	3.061	0.93	0.305	3.435	-3.940	0.98
S10	-1.767	0.235	3.230	0.97	-0.129	4.334	-3.004	0.99
S11	0.452	0.004	7.147	0.96	0.137	2.726	-3.071	0.99
S12	-1.614	0.268	3.081	0.93	0.07	3.179	-3.025	0.98
S13	-0.353	0.025	6.395	0.98	0.159	21.583	-7.027	0.99
S14	-1.482	0.283	2.955	0.92	0.038	3.239	2.885	0.99
S15	-0.163	0.002	8.249	0.94	0.516	38.294	-7.005	0.97

The R-squared value, indicates goodness of fit, for all fitted calibration curves is higher than 0.9, i.e. a good agreement is achieved between the experimental results and the fitted curves. This model-function is sensitive for the range from 1 to 5 m/s. However, for velocities under 1 m/s a non negligible calibration errors were detected as shown in Fig. 5.6.

5.2 Field tests

5.2.1 Geometry of the container

Most field tests took place in a specially prepared experimental container. This container belongs to a group of containers which are used usually for transporting goods offshore, such as bananas from Central America to Europe. In the interest of performing measurements in the container, some modifications were necessary. These modifications are basically some partitions enabling to install the electronic parts, base station(s) and other facilities [Lang11].

The external dimensions of the container are: 12.192 m (40'), 2.438 m (8'), and 2.896 m (9.5') for length, width and height, respectively. The internal dimensions
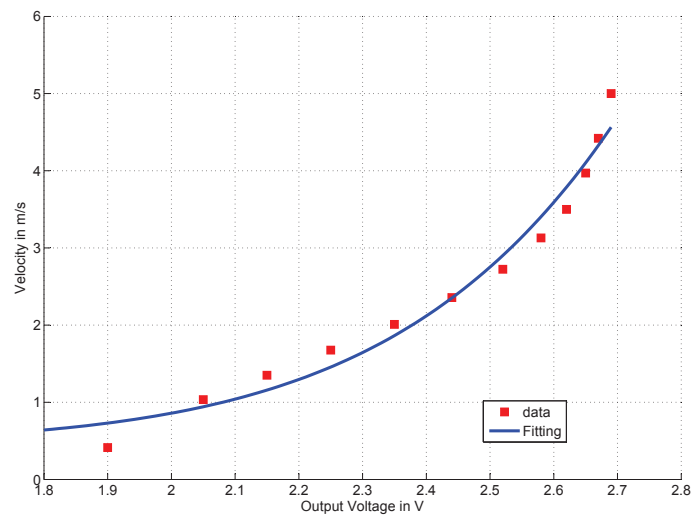
Figure 5.6: Calibration curve of one thermal flow sensor

are: 11.590 m, 2.294 m, and 2.557 m for length, width and height. The container
is filled with banana pallets. One pallet consists of 48 banana boxes, made up of 8
layers (called also tiers) with 6 boxes in each layer (see Fig. 5.7.c). Dimensions of one
box are: 0.50 m, 0.40 m, and 0.25 m for length, width and height. consequentially
one pallet dimensions (Euro-Palette) are: 1.2 m, 1.0 m, and 2.0 m for length, width
and height. Because the size of banana pallets does not fit the container dimensions,
part of the pallets have to be rotated by 90°. The standard scheme (L1) of pallet
layout inside the container is shown in Fig. 5.7.a. A new layout (L2), also called the
chimney layout, was tested in the measurements. In this new layout a considerable
gap is created between each four-pallet sets as in Fig. 5.7.b. The maximum number
of pallets which can be loaded is 20. However, we performed several tests with 16,
12, 11 or 8 pallets. Deciding the number of pallets in each test is related to several
considerations such as the time, logistic, and number of sensors available for that
test.

The cooling unit is placed behind the reefer side. Inlet and outlet are at the bottom
and top of the reefer wall. Incoming airflow from the inlet is pushed through air
ducts located on the floor of the container. These ducts are open from top as shown
in Fig. 5.8. The advantages of the channels are that they guide air for long distance,
distribute it uniformly and allow some space under the pallets.

Fig. 5.9 shows the top view of the container filled with 16 pallets distributed accord-
ing to the chimney layout (L2). In this case, four chimneys were created. Fig. 5.10
shows the top view of the container filled with 16 pallets distributed this time ac-
cording to the standard scheme layout (L1). It is important to mention that there
is a considerable gap between one row of pallets and container's door according to

Figure 5.7: (a) The standard scheme layout of pallets in the container, (b) the chimney layout of pallets in the container and (c) top view of a pallet shows the six boxes on the top layer.
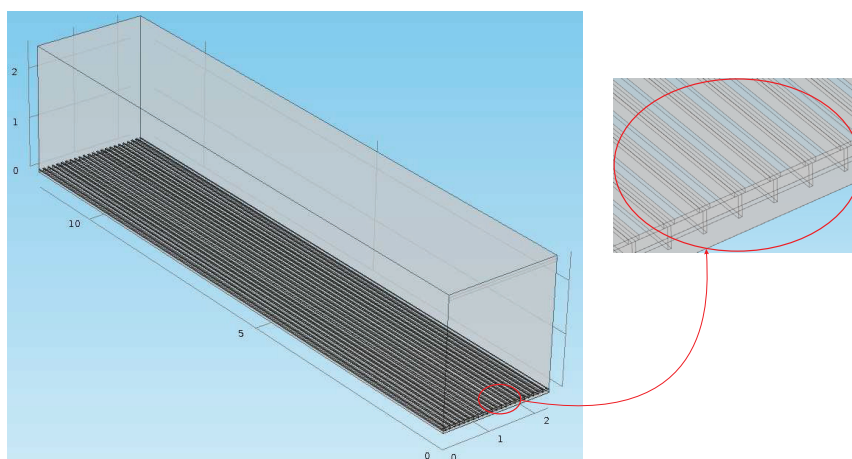
Figure 5.8: view of the container and a view show the air channels on the floor

this layout.

Fig. 5.11 shows a side view of the container filled with 16 pallets.

5.2.2 Primary observations of turbulence features in the container

Airflow measurement is crucial to obtain the real values inside the container and combine them with other parametric values. Flow sensors are part of a wireless sensor network which communicates with an internal gateway through the "BananaHop" protocol which had been developed previously for the project tests with bananas in the Intelligent Container [Lang11]. The gateway operates as a bridge

Figure 5.9: Top view of the container equipped by 16 pallets

Figure 5.10: Top view of the container equipped by 16 pallets

between the internal wireless sensor nodes and the mobile network to access sensor readings by means of a graphical user interface on an internet web server.

An equipped container is an enclosed area with a complex geometry to allow any flow through it. Incoming air is pushed through the inlet which is located at the bottom of the reefer side. 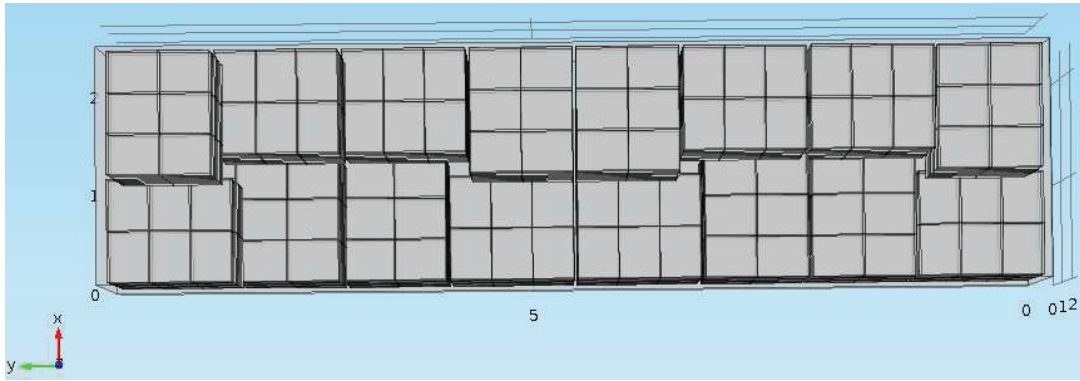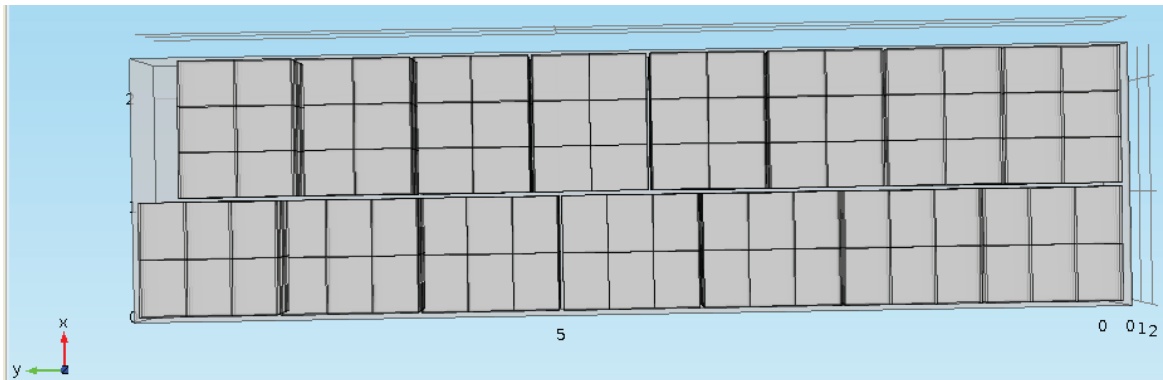All pallets and boxes are obstacles disturbing the air movement. The flow inside the container is turbulent as the definition of turbulence can be cited as a continuous three dimensional flow contains eddies or whirls of different sizes. Turbulence is nonlinear and turbulent eddies transport both energy and matter over time and length scales of varying sizes [Carp11]. The large turbulent eddies transfer their kinetic energy into smaller eddies until viscosity dissipates the eddies into heat [Carp11].

The dynamic and thermal instabilities encourage forming turbulence inside the container. On the one hand, the dynamic instabilities are caused by the boundary between air volumes with different velocities. Incoming air flows under the pallets through the air ducts (see Fig. 5.8) and outgoing air flows above the pallets towards the outlet at the top of the reefer side of the container. Between these two clouds, air flows in gaps between pallets in both vertical and horizontal directions. All pallets representing obstacles in front of the airflow causes deflection of the flow distribution
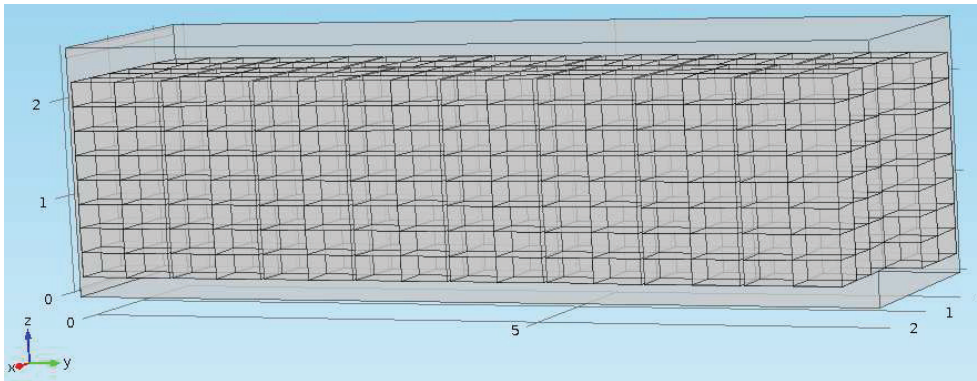
Figure 5.11: Side view of the container with all pallets and boxes

Figure 5.12: Photo of the container during pallets loading

generating a gradient in the airflow. This flow gradient creates a shear stress which is an important source of turbulence.

On the other hand, the thermal instability is caused by the difference in temperature between the incoming air temperature (about 13°C) and the temperature of the components inside the container. It is important to consider the generated heat by the bananas inside boxes due to respiration and other physiological aspects after the harvest. When the temperature of banana boxes increases the temperature of the surrounding air inceases as well. Due to the buoyancy forces the warmer air particles start to move. As a result the convection phenomenon is created which participates in forming the turbulence inside the container.

By using the Reynolds notifications, one parameter x can be expressed as two com-

ponents: the mean component $\bar{x}$ and the varying component x' as:

$$x = \bar{x} + x' \tag{5.2}$$

The arithmetic mean and the varying components are given as:

$$\bar{x} = \frac{1}{n}\sum_{i=1}^{n} x_i \tag{5.3}$$

$$\overline{x'} = 0 \tag{5.4}$$

where, n is the number of elements in one period. The related standard deviation is given as:

$$\sigma_x = \sqrt{\frac{1}{n-1}\sum_{i=1}^{n}(x_i - \bar{x})^2} \tag{5.5}$$

Evaluation of the received data from each sensor is done by calculating the mean velocity value $\bar{v}$, standard deviation of the collect data σ_v and the turbulence intensity (I) as main parameters of turbulent airflow. The latter quantity (I) is defined as the standard deviation of the longitudinal air velocity in respect with the mean velocity, as in the following equation [Carp11]:

$$I = \frac{\sigma_v}{\bar{v}} \tag{5.6}$$

Examples of some sensors' results are shown in Tab. 5.2.

5.3 Field tests and Results

Several tests have been performed in the evaluation of airflow pattern in logistic containers during the thesis time 2010 - 2013. Most of these field tests took place in Stelle, Germany.

The flow inside the container is turbulent due to the pressure difference, multiple obstacles in front of the incoming airflow and the non-uniform gaps between pallets. This turbulence feature is also not stable everywhere in the container. It depends on
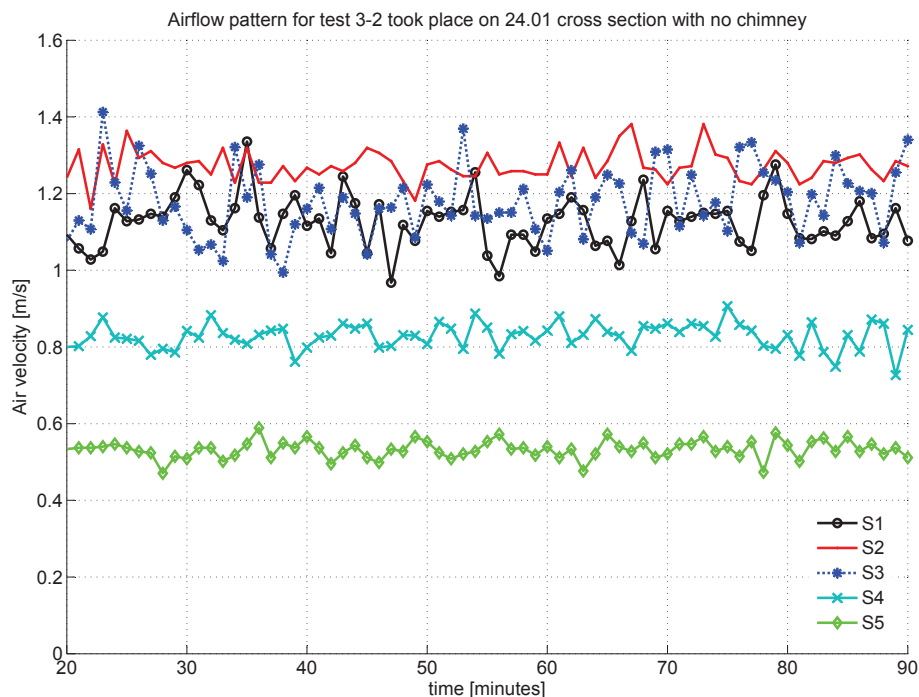
Figure 5.13: Examples of some sensors results show the turbulent aspect of the airflow inside the container (test took place in January 2013)

the position, layout and input flow. Fig. 5.13 cites the experimental results obtained by five sensors placed in one cross section of the container, i.e. between two pallets. They are in different height levels, their position, mean velocity, standard deviation and turbulence intensity are mentioned in Tab. 5.2.

The Tab. 5.2 additionally shows the mean velocity value, standard deviation and the turbulence intensity of these sensors

The following tests were performed by using a reduced number of pallets (12 pallets) to evaluate the airflow pattern in the container for both, the standard and the chimney layouts. Due to the limited number of available sensors (15 IMSAS sensors), four separate tests were arranged to evaluate airflow in the wall side of the container, on the top of pallets, under the pallets, and in a cross section of the container. In total eight 8 separate tests were needed for both layouts. The sensors were distributed in each test according to one plane of: XY, XZ, or YZ. The plane XY is used in two tests to evaluate airflow pattern above and under the pallets. The plane YZ is used for the wall side of the container. Here, the sensors were fixed on a few pallets in the empty space between the wall and the pallets. The plane XZ is used to evaluate airflow in a cross section.

Eleven pallets were used in the standard scheme layout (L1), whereas twelve pallets

Table 5.2: Mean velocity value, standard deviation, and turbulence intensity for some sensors placed in different position of the container

Sensor	Position	Mean velocity (m/s)	Standard deviation (m/s)	Turbulence Intensity
S1	P3 (S1, T1)	1.13	0.07	6 %
S2	P3 (S1, T4)	1.27	0.04	3 %
S3	P3 (S1, T8)	1.18	0.09	8 %
S4	P4 (S2, T1)	0.83	0.03	4 %
S5	P4 (S2, T4)	0.57	0.07	12 %

were used in the chimney layout (L2). These pallet numbers allowed obtaining an aligned end of pallets from the door side. However, the used length of the container is not equal; 6.30 m in L1 compared to 6.90 m in L2. It was assumed that this slight difference in length will not affect the results obtained from the comparison between the two layouts.

5.3.1 Wall-side tests

The purpose of these tests is to evaluate and examine the airflow distribution in the side space between the container-wall (right side) and the pallets placed near it.
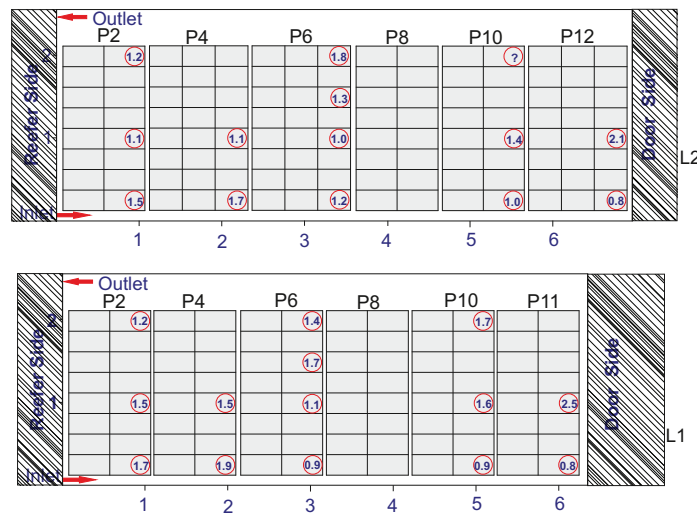
Figure 5.14: Results of the wall side tests for both layouts

All sensors were placed vertically in this test to check the airflow movement in the vertical direction. As expected, the airflow rises from bottom to top of the pallets and all sensors gave positive values. Results, as depicted in Fig. 5.14, show that :

- In the low level, tier 1, the vertical air velocity decreases from the reefer side towards the door side, whereas in the middle and top levels, this velocity increases from the reefer towards the door side.

- The velocity decreases from the bottom to the top for pallets near reefer side, whereas the inverse is noticed for pallets near the door side.

- Both layouts show similar results for this test, i.e. airflow behavior is similar in the gap between the pallets and the wall.

5.3.2 Top of pallets tests

The purpose of these tests was to evaluate airflow pattern in the level above the pallets. Sensors were placed on the top of the pallets in three positions along the container (see Fig. 5.15). All sensors showed negative values, i.e. flow direction is from the door side towards the reefer side. This was expected because airflow is in the direction of the outlet. Tests' results show that:

- Small velocity values appear on the top surface of the pallets, because the distance from the pallets top to the ceiling is empty, thereby higher velocities resulting at the level of the outlet.

- Results were unstable along the width of the container. Values vary between 0.2 and 1.4 m/s for standard layout (L1), whereas these values are between 0.2 and 1.1 m/s for the chimney layout (L2).
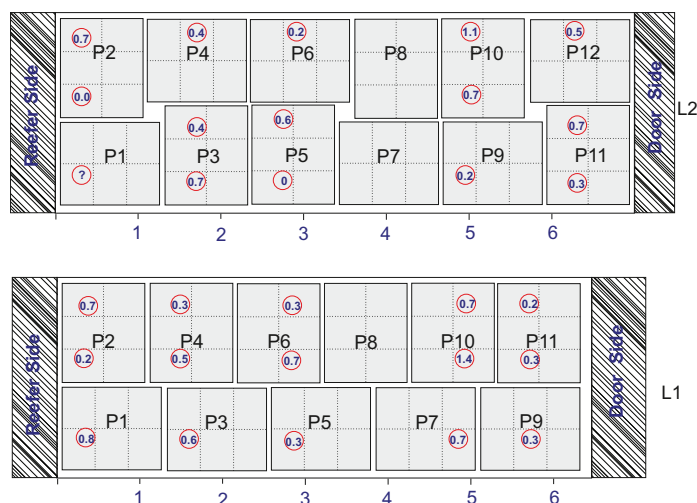

Figure 5.15: Results of airflow evaluation in the level of top of the pallets for both standard layout (L1) and chimney layout (L2)

5.3.3 Bottom of pallets tests

The purpose of these tests is to evaluate airflow velocities under the pallets (see Fig. 5.16). The sensors were placed in the wooden pallets (holders) which are used to hold banana pallets and to move them by means of the lift. The wooden pallets have empty spaces between their feet. Results show that:

- Velocities in the horizontal direction decreases in general from the reefer side to the door side

- Sensors in the middle show higher values than those near the walls

- Sensors readings are affected by obstacles (the feet of the wooden pallets) which cause turbulence flow and also by the gaps separating the pallets.
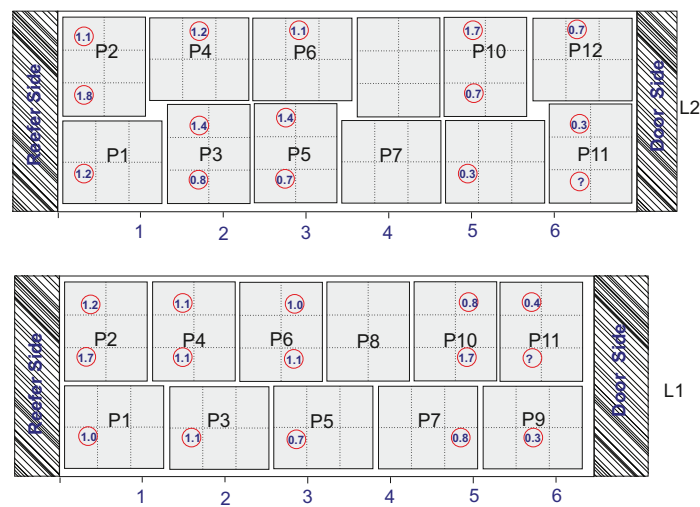
Figure 5.16: Airflow velocities at the level under the pallets

5.3.4 Airflow in cross section

In these tests airflow distributions were checked in some cross sections of the container. In the standard layout (L1), it is not possible to distribute sensors in one cross section plane, so they were distributed on the nonaligned pallets (3 and 4) from one side and (7 and 10) from the other side. However, in the chimney layout it is possible to place all sensors in one XZ plane. they were distributed on the (3 and 4) pallets from one side and on the (7 and 8) from the other side.Fig. 5.17 depicts air velocity values at the cross sections mentioned above. Results show the following:

- The standard layout shows higher velocity values in comparison with the chimney layout. This can be explained by the fact that flow goes through the open chimney rather than other smaller gaps.

- No general trend describes the velocity distribution according to the X direction.

Figure 5.17: Airflow at cross sections of the container
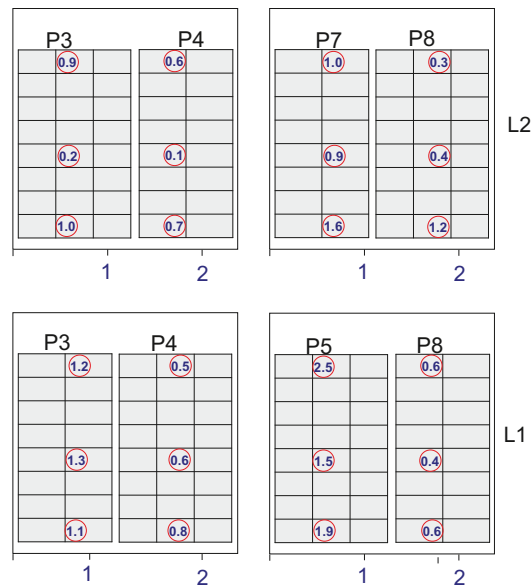
5.3.5 General evaluation

The above results mentioned in sec. 5.3 are samples of the performed tests. Some additional results are cited in sec. 6.2 to validate simulations.

The performed experimental measurements proved that thermal flow sensors are powerful tools to enable measuring airflow accurately in the container. They were tested almost in all gaps and areas of the container. They were successfully integrated within the wireless network through the BananaHop protocol. However, these results are not enough to give a complete evaluation of the airflow distribution. The main reasons are: first, the number of available sensors (15 only) is very small comparatively by the container dimensions. Second, the sensors were used in separate tests assuming that all conditions of experimental measurements are identical in repeated tests. In practice, the main factors that influence airflow distribution in the container are the gaps between pallets and it is almost impossible to obtain equal gaps between pallets.

6 Results and Discussion

This section presents the k-ε simulation model and the obtained results (sec. 6.1.2). On the one hand, simulations' results are compared with airflow experimental measurements in favour of validating these simulations (sec. 6.2). On the other hand, airflow results are compared with temperature data obtained from several offshore and ashore measurements (sec. 6.3). Such comparisons enable explaining the reason and place of "hot spots" in the container, as well as taking actions to improve the efficiency of cooling system.

6.1 Simulation Model

It was mentioned in sec. 1.2 that the k-ε method from the RANS approach was selected to perform CFD simulations of the airflow inside the container. The k-ε model is one of the most common turbulence models. This model, similar, to other RANS (Reynolds-averaged Navier-Stokes) approaches evaluates averaged variables for both steady-state and dynamic flows. Therefore, it deals with the mean of the air parameters, which is more useful than the instantaneous value of the turbulent flow parameters. As a consequence airflow distributions can be quickly predicted. The k-ε model has become very popular for industrial applications due to its good convergence rate and relatively smaller requirements of needed time and computer resources. It is frequently used for modeling airflow in enclosed environments although it has limitations for some problems where a high pressure difference exists.

6.1.1 Description of the Model

The COMSOL MULTIPHYSICS program version 4.3b [COMS12] was used for developing a simulation model to evaluate airflow distribution in a pre-designed container. The model was built by stationary studies of the k-ε turbulent flow physics. The model has 5 free constants, their standard values are (see sec. 1.2.2): $C_{1\varepsilon} = 1.44$; $C_{2\varepsilon} = 1.92$; $C_\mu = 0.09$; $\sigma_k = 1$; and $\sigma_\varepsilon = 1.3$. Boundary conditions are as follows: inlet velocity is 8 m/s which is equivalent to the cooling unit capacity 5480 m^3/hr at 50 Hz power supply. Turbulence intensity (I) is set to 3 %. This value is estimated from the experimental airflow measurements mentioned in chapter 5. The turbulence length scale (l) is estimated to be 0.004 m which represents 5% of the channel height of the inlet.

A mesh sensitivity study was performed to ensure the accuracy of the results. In this mesh refinement four different meshes were tested. The specifications of the four meshes are provided in Tab. 6.1. The finest mesh is considered as reference mesh, i.e. M4 in this case. Then, the relative errors were calculated for the first three solutions (S_1, S_2, and S_3) in respect to the reference solution (S_4). The presented results in this paper are taken from the third mesh (M_3) where the relative error is less than 1.5 % in respect to the reference result. (S_i) in the table Tab. 6.1 refers to the solution corresponds to the mesh (M_i).

Table 6.1: Mesh sensitivity study

Mesh solution	Total number of mesh elements	Maximum element dimension (m)	Relative error $\frac{S_4 - S_i}{S_4} \cdot 100$
M_1	294340	0.552	10.8 %
M_2	717834	0.242	5.2 %
M_3	913075	0.162	1.4 %
M_4	1122916	0.128	

The wall function expresses the relationships between the velocity and the wall shear stress [CFD11]. Close to the wall in the viscous sub-layer it is given empirically that:

$$u^+ = y^+ \tag{6.1}$$

with u^+ and y^+ are the dimensionless velocity and wall distance, respectively. In the region where $30 \leq y^+ \leq 100$ the velocity profile can be estimated with the log law:

$$u^+ = \frac{1}{\kappa} ln(y^+) + B \tag{6.2}$$

with κ is von Karman's constant, B is universal constant. These constant values are set by COMSOL as default values to 0.41 and 5.2, respectively. In this model, COMSOL includes the viscous sub-layer and the logarithmic layer. The wall offset is computed automatically by COMSOL as an integral part of the solution process.

The inner dimensions of the cargo hold of a standard 40 feet reefer container are as follows: $11.590 \times 2.294 \times 2.557 \ m^3$ (Length × Width × Height). This container is equipped with a Thermoking Magnum Plus cooling unit. The inlet and the outlet are at the bottom and top of the reefer side, as shown in Fig. 6.1. Airflow patterns were extracted for a container loaded with banana pallets. One pallet consists of 48 banana boxes, made up of 8 layers (called also tiers) with 6 boxes per layer. The dimensions of one box are: $0.5 \times 0.4 \times 0.25 \ m^3$. Consequentially, the dimensions

of one pallet are: $1.2 \times 1.0 \times 2.0$ m^3. Since the size of banana pallets does not fit the container dimensions, part of the pallets have to be rotated by 90°. The standard pallet layout scheme (L1) inside the container is shown in Fig. 6.2 (a). A new layout (L2), also called the chimney layout, was tested in both simulations and measurements. In this new layout a considerable gap is created between each four-pallet sets as in Fig. 6.2 (b). Two cases were checked either by keeping the top of the chimney opened (L2_1) or closed (L2_2).
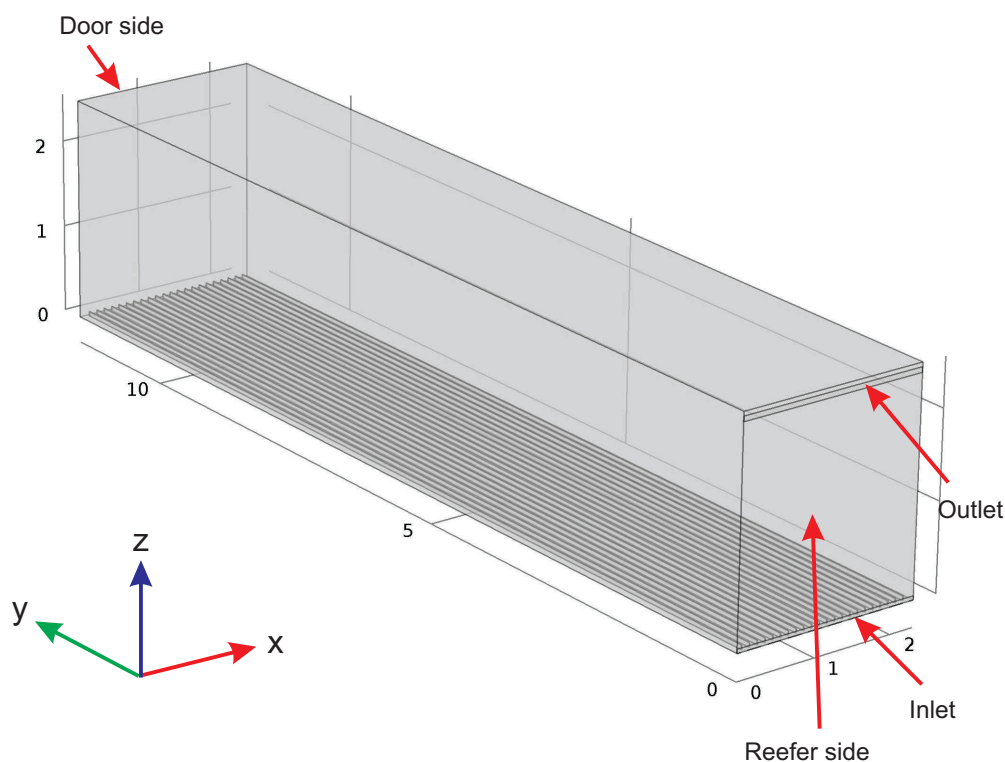

Figure 6.1: Empty container

The simulation model was built in accordance with the experimental setup which consists of a specially equipped 40-feet container and two banana loading schemes: standard and chimney-based. Due to the availability of resources, time and logistic difficulties, only 11 pallets under the standard scheme and 12 under the chimney-based scheme were tested. This reduced scale approach enabled optimized testing time for multiple tests. Therefore, to be confer with the experimental setup, simulations were done for a reduced number of pallets in the container: 11 for L1 and 12 for L2 (see Fig. 6.2). The difference in pallet numbers in the two loading schemes is to obtain an approximate alignment of the last row of pallets in both layouts. With a view to separate the pallets from the unused space in the container, a mobile wall was installed after the last row of pallets and well-sealed by using foam and duct tape.
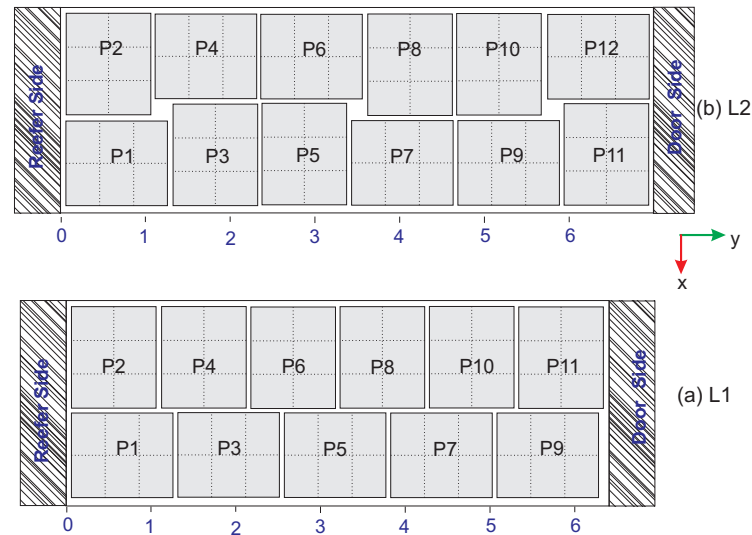
Figure 6.2: Top view of the container for: (a) standard scheme layout and (b) for chimney layout L2.

6.1.2 Simulation Results

Simulations were conducted for the two above-mentioned layouts L1 and L2 (see Fig. 6.2). Free convection is considered as negligible since the maximum recorded temperature difference is about 2° C. To show these results in a comparative way, some particular planes were considered in the container. First, in the XY plane three basic cases are essential to be discussed: under the pallets, in the pallets level and above the pallets. In the inlet level (i.e. under the pallets as shown in Fig. 6.3) high velocities were noticed in the front of container decreasing gradually with the y coordinate. Velocity values are about 8 m/s at the inlet level, 4 m/s in the middle and 2 m/s at the end of the simulated part. All cases show approximately similar results. However, for higher levels, i.e. in pallets level (z = 0.2 to 2.2 m), contradictory results were found. In the front part of the container very low air velocities began at less than 0.2 m/s at reefer side and then they increase gradually to be about 1 m/s at the middle of the container, ending with 3 m/s at the end of the container (see Fig. 6.4). Additionally, air velocities inside the chimneys in L2_1 layout are higher than the ones in surrounding gaps. Chimneys do not have identical impact on airflow distribution. The chimney near the reefer side has lower velocity values than the one in the middle, which has a lesser value than the one close to the door (Fig. 6.4 L2_1). In the L2_2 case, where the top of the chimney is closed, we notice how airflow is forced to flow in the gaps surrounding the chimneys (Fig. 6.4 L2_2). This causes a more uniform distribution of air velocity in L2_2 layout in comparision with L1 and L2_1.

The third level is the outlet level, i.e. above the pallets. There, we have similar airflow distribution to the one at the inlet level with the difference in velocity values and homogeneity (see Fig. 6.5). In Fig. 6.5 we notice that the returning airflow starts
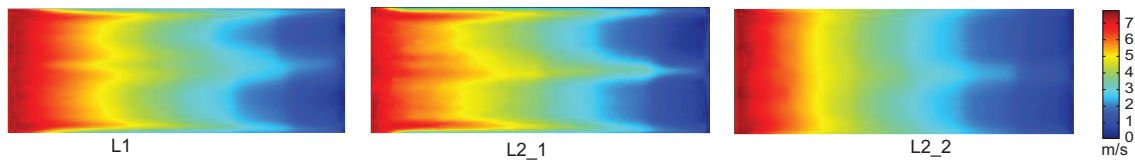
Figure 6.3: Velocity magnitude in the inlet level for the three cases L1, L2_1 (chimneys with opened top) and L2_2 (chimneys with closed top)
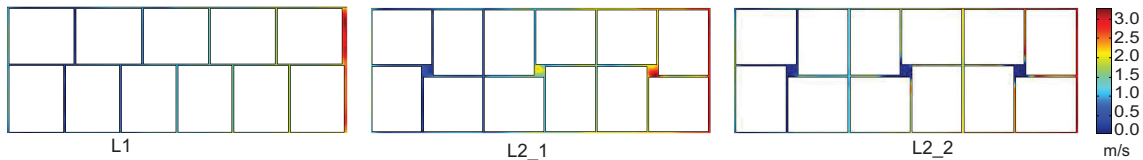

Figure 6.4: Velocity magnitude in pallets level for the three cases L1, L2_1 and L2_2

with low velocities of about 0.5 m/s and increases gradually to about 3 m/s at the outlet level on the reefer side. It is notable that there are two separated clouds of velocity above the two rows of pallets in L1 case. It is recognised that there are low velocities near the lateral walls as well as in the middle (above the gap separating the two rows of pallets) and relatively high velocities above the pallets. The velocity profile above each row of pallets is the profile of turbulent flow as shown in Fig. 6.6. In the L2_1 case these 2 clouds are clearly viewed but with some connection areas above the chimneys and above the first part of the container (with lower values in the middle). Additionally, there is a recognized high-velocity-spot above the third chimney. However, for the L2_2 we notice a uniform velocity distribution above the first half of the container where the two clouds are merged together and start to separate in the second half. The Figures: Fig. 6.3, Fig. 6.4 and Fig. 6.5 show that the expected hot spots can be created in the first part of the container. Because the cooling air is supplied from the floor side, the best cooling is achieved in the lowest tier (1). The highest tier (8) is additionally cooled over its top side from the return air flow. The highest temperatures were found in tiers 5 to 7 according to the temperature measurements [Jede13]. Therefore, the boxes in these tiers of the first two pallets are the most likely to produce hot spots. Comparatively, L2_2 produces the best homogeneous-airflow distribution.
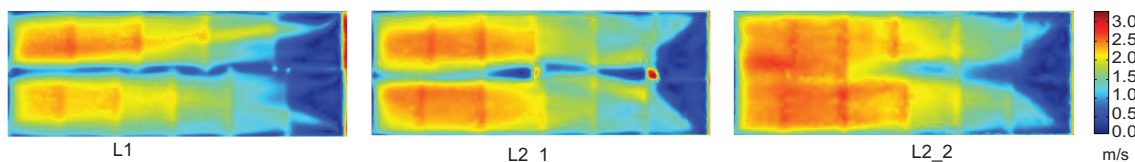

Figure 6.5: Velocity magnitude above the pallets for the three cases L1, L2_1 and L2_2

In the XZ plane, airflow velocity distribution is highly influenced by the y coordinate
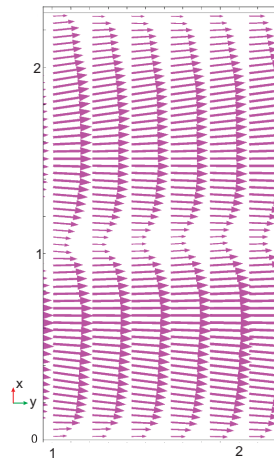
Figure 6.6: Velocity profile above the pallets

of this plane. Velocity, in the pallets level, increases with the y coordinate. Highest values are at the end of the container especially in the gap between the door and the last row of pallets. By comparing the velocity distribution at that gap, we find similar behavior between L2_1 and L2_2 from one side and different behaviour between L1 and L2 from other side. Similarity (between L2_1 and L2_2) is by obtaining a homogeneous airflow distribution in that gap in the pallet level, whereas in L1 case there is non-symmetric distribution as shown in Fig. 6.7 . This difference is not only because of the different layout but also because of the larger gap on the left side. The two rows of L1 layout do not end at the same coordinate; the maximum difference is about 4 cm.
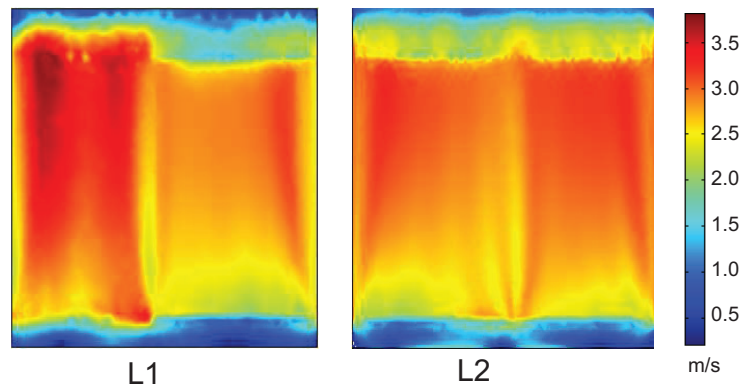
Figure 6.7: Comparison between airflow distribution in the XZ plane at the end of the container in the gap, between the end pallets and door

Another interesting issue can be noticed in the XZ plane; it is the airflow behaviour around a chimney. When comparing the two chimney layouts, (L2_1 and L2_2) in the XZ plane at the third chimney (y = 5.62 m), the result shown in Fig. 6.8 is found. In L2_1 the higher velocity is through the chimney whereas in the L2_2 case, the flow is forced to go through all gaps around the chimney as it is closed

from top. This fact causes more fresh air to flow in the gaps in the region of 5-7 tiers which were found from temperature measurements as the hottest tiers in all pallets. Consequently, more cooling air is provided to these specific regions.

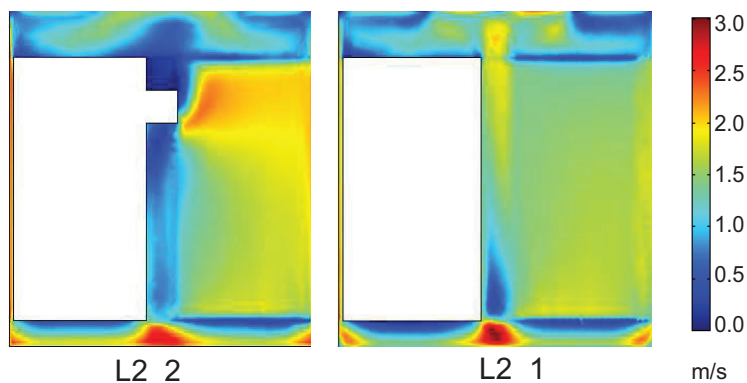**Figure 6.8:** Airflow distribution in the XZ plane of the container at the coordinate (Y= 5.62), the middle of the third chimney for both cases of chimney layout: open and close top of the chimney

In the interest of quantifying the uniformity of these layouts we collected all velocity data along the width of the container in three different horizontal planes and three positions in each plane. The horizontal planes correspond to the heights (z= 0.15, 1 and 2.3 m) and for each plane the three positions correspond to the coordinates (y= 1.1, 3.5 and 5.1 m). Tab. 6.2 depicts the mean velocity and the standard deviation in each position. Results show that standard deviation for L2_2 layout produces, comparatively, the best homogeneous-airflow distribution, as the standard deviation of velocity values are the minimum in most cases.

Table 6.2: Quantifying velocity distribution by calculating mean velocity and standard deviation in 9 different positions of the container.

	Top.1	Top.2	Top.3	Mid.1	Mid.2	Mid.3	Bot.1	Bot.2	Bot.3
L1	2.20 ± 0.56	1.74 ± 0.45	1.13 ± 0.37	0.44 ± 0.23	1.48 ± 0.33	2.14 ± 0.16	2.00 ± 0.38	2.15 ± 0.56	1.30 ± 0.66
L2_1	1.86 ± 0.40	1.59 ± 0.33	1.16 ± 0.36	0.35 ± 0.22	1.79 ± 0.26	1.70 ± 0.34	2.10 ± 0.17	2.04 ± 0.48	1.47 ± 0.51
L2_2	1.87 ± 0.31	1.56 ± 0.29	1.15 ± 0.34	0.39 ± 0.25	1.75 ± 0.21	1.86 ± 0.29	2.08 ± 0.20	1.99 ± 0.47	1.38 ± 0.46

6.2 Comparison Between Simulation and Measurement Results

As mentioned in chapter 5 the experimental measurements could prove that thermal flow sensors are powerful tools enabling measuring airflow accurately in the container. The sensors were manipulated in more than ten tests and were tested almost in all gaps and areas of the container. These flow sensors were successfully integrated within the wireless network through the "BananaHop" protocol. Sensors' readings were monitored during the tests by the web server via internet. Their data were essential to determine the simulation-model parameters and to give an idea about air velocity values in a specific region of the container. However, the experimental airflow measurements are insufficient to make a complete comparison with all simulations because of the limited number of sensors used which can provide airflow values only in the specific positions where they were placed.

This subsection presents two comparison examples between both simulation and measurements results in order to validate the simulations. First comparison example is in the floor level of the container under the pallets (inlet plane). In this level there are no obstacles in front of the incoming cold air. Airflow is pushed through the open-top channels located on the container's floor (see sec. 5.2.1). Air velocities in both horizontal and vertical directions were measured in seven positions in the middle of the container as shown in Fig. 6.9. The velocity magnitude (v) is calculated by combining the horizontal velocity (v_y), the vertical velocity (v_z) according to the equation:

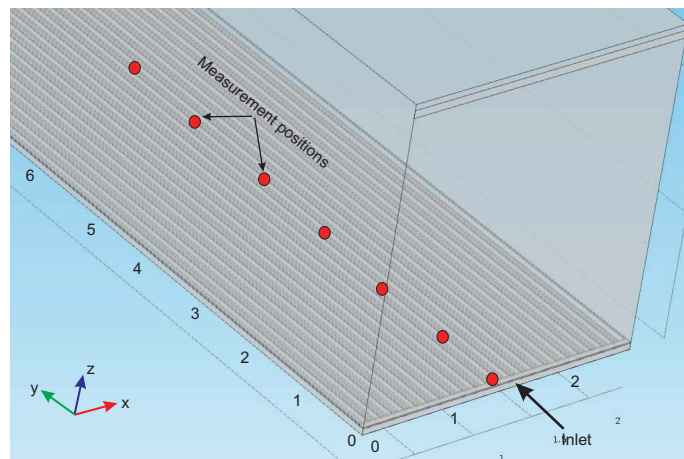$$v = \sqrt{(v_y^2 + v_z^2)} \tag{6.3}$$

Figure 6.9: Positions of test points in the floor of the container

Fig. 6.10 shows the comparison between both simulation and experimental results. Both results show a similar trend and good agreement in the first part of the container before a slight deviation starts to increase with y coordinates.
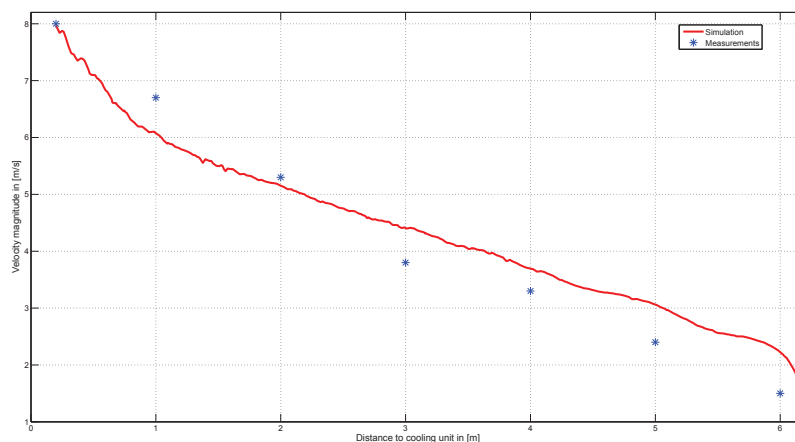

Figure 6.10: Velocity magnitudes in the inlet level. Points are experimental results and line is model simulation, with corresponding model simulated line.

Second example is to compare simulation and measurement results in some positions located in the gap between the pallets and the container's wall. Sensors were attached in that gap outside the boxes in the fourth row (about 1.2 m from floor) as shown in Fig. 6.11. They have detected the vertical velocity (v_z). The pallets arrangement in this test is according to the chimney layout (L2). Comparison shows that both results have a similar trend, although it lacks experimental data within 2 m to the cooling unit. The simulated air velocity increases with the y coordinate. Some negative values for air velocity are observed near the cooling unit. The negativity means that air is flowing in the negative direction of z axis. The main reason for this negative velocity is the entrainment effect caused by the wall jet (see Fig. 6.19). It is important to notice here that the tortuosity in the simulation curve is due to gaps between pallets where additional airflow come from these gaps.

6.3 Comparison with Temperature Results

Temperature, as main parameter which affects produce's quality during transportation, was measured and monitored during many tests in the last five years [Jede13]. This includes offshore and ashore temperature tests. Offshore tests took place during containers transportation from Central America to Europe, whereas as the ashore tests were performed with the same container already described for airflow measurements (see sec. 5.2.1). To explain the main results (founded by temperature measurements) and also to better understand the effect of airflow on temperature distributions, this study suggests comparing temperature results with those of airflow.
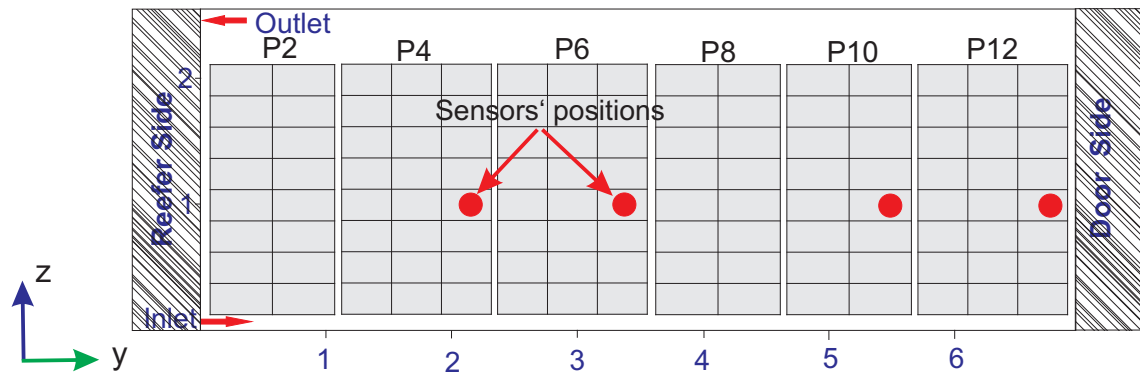
Figure 6.11: Positions of test points in the gap between pallets and container's wall at a distance 1.2 m from floor
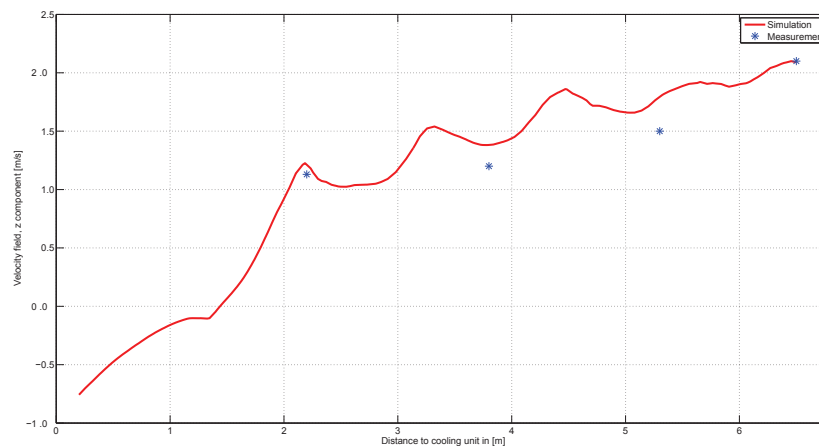

Figure 6.12: Vertical velocities in the gap between pallets and wall of container at a height of 1.2 m from floor. Points are experimental results, with corresponding model simulated line.

First, it was found that the speed of temperature change inside the pallets is rather slow. It may take one week until the box temperature arrives at a stable temperature value [Jede13]. Fig. 6.13 (left) shows the temperature curves recorded in tier 5 (about 1.25 m from floor) during a sea transport from Costa Rica to Antwerp in 2011. Temperature sensors were placed in the center of the banana boxes. Results show that temperature vary significantly with the horizontal distance (y). Fig. 6.13 (right) depicts the average temperature over the transport duration as function to the distance from the cooling unit. The maximum temperature difference is about 1.9° C over the whole container. The first pallet which is located near the cooling unit was 0.5° C warmer than any other measured point in the container. The higher temperature in the first part of the container just beside the cooling unit form unexpected hot spot. Simulations can well explain the reason why a hot spot is forming in this region. Fig. 6.14 shows airflow simulation in the YZ-plane in the gap between the two rows of pallets in the standard scheme L1. a wall jet

effect is presented by that Figure. The cold air is pushed through the inlet into the container's volume which contains air (moving or stagnant). The velocity is zero at the walls due to the no slip condition of a viscous fluid. In the inlet height level there are no obstacles in the y direction. The pushed air causes an entrainment effect where the existing air gets drawn into the developing wall jet. This entrainment effect causes a large eddy in the front part of the container (see Fig. 6.14) which is the result in turbulent mixing. In this region, the hot spot is formed due to two reasons: the poor ventilation in the middle part of the pallet and the relatively warm returning air.
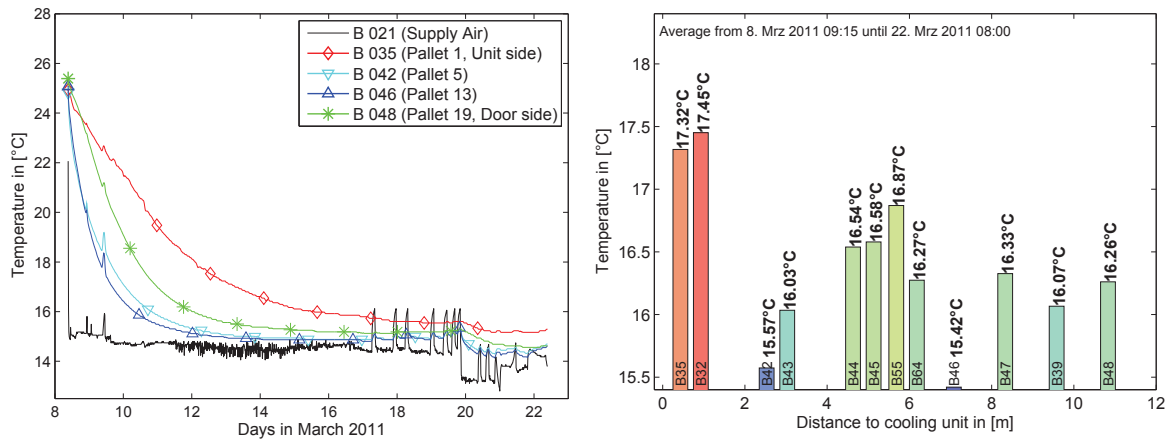
Figure 6.13: Temperatures recorded in tier 5 during a transport in 2011. Temperature over time (left) and average temperature (right). (Figure prepared by R. Jedermann)

Figure 6.14: Velocity magnitude in the YZ-plane in gap between the two rows of pallets for the standard scheme layout L1

Second, it was found from several tests that temperature varies vertically in pallets. As a general rule: the warmest boxes were found in tiers 6 to 7 (1.50 to 1.75 m from

the ground). This can be explained by the fact that the lower tiers are cooled from pushed air under pallet whereas the tier on top is cooled by the returning airflow above pallets. Fig. 6.15 shows temperature distribution according to the vertical axis. In each tier (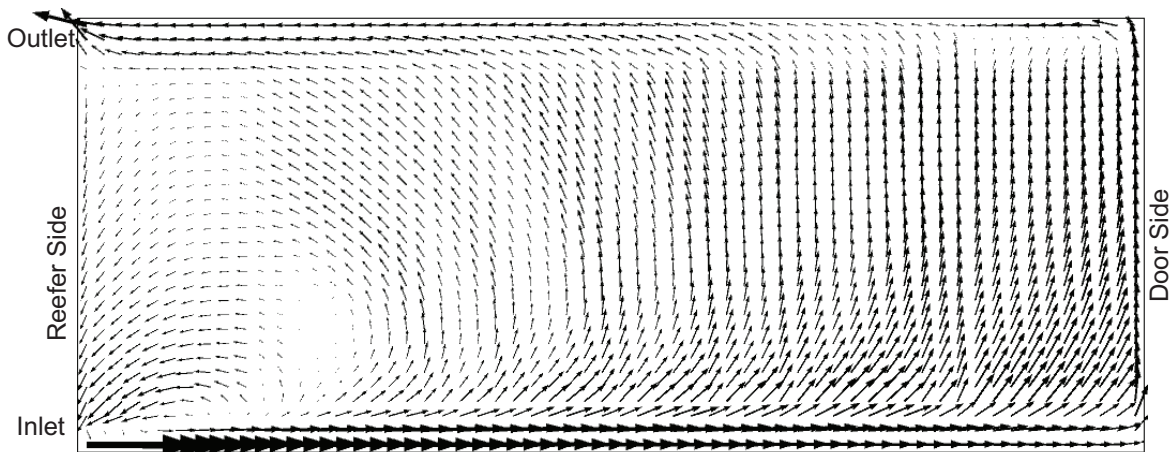raw) temperature is calculated as mean value for the whole container and represented with its standard deviation. In favour of minimizing temperature differences for these tiers, the chimney based layout of pallets was suggested. By closing the top of chimneys, more fresh cold air is forced to flow in the gaps around the chimney which cool down boxes in the tiers 6 to 8 (see Fig. 6.16).
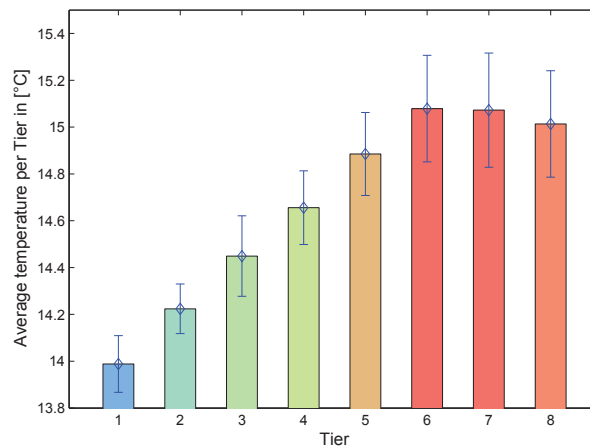
Figure 6.15: Vertical temperature distribution and standard deviation (Figure prepared by R. Jedermann).
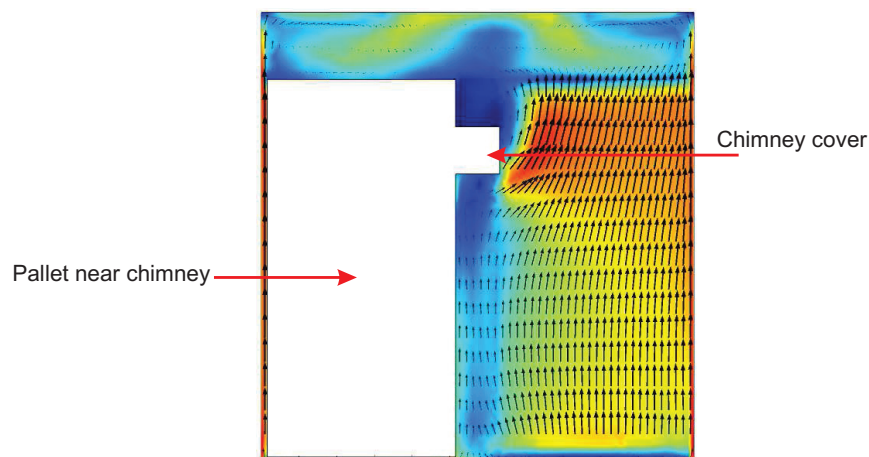
Figure 6.16: Velocity magnitude in XY plane in and around one chimney

Third, it was found from four tests ashore that the corners of a bananas box respond much faster to temperature changes than the boxes' center within stable conditions of the container. To evaluate this cooling effect, Jedermann et al. [Jede13] presented a linear system model to approximate the temperature curves. The model has the air and the box center temperatures as inputs. It consists of two delay elements with

time constants of 0.3 hours and 4 hours. The model adapts to different degrees of cooling efficiency by adjusting a dimensionless gain factor k1 to scale the influence of air temperature to the corner. k1 can be estimated by system identification techniques. A high value of k1 indicates fast cooling by high air flow. Test's results showed that the distance from cooling unit has significant influence on k1 values. Fig. 6.17 shows the mean value of k1 calculated for loggers' data installed in the XZ-plane in the gaps between the pallets. The light blue bars refer to the chimney based layout, whereas the dark blue bars refer to the standard scheme layout. 16 pallets were used for both layouts. Fig. 6.17 indicates clearly that the cooling effect increases with the distance from cooling unit.
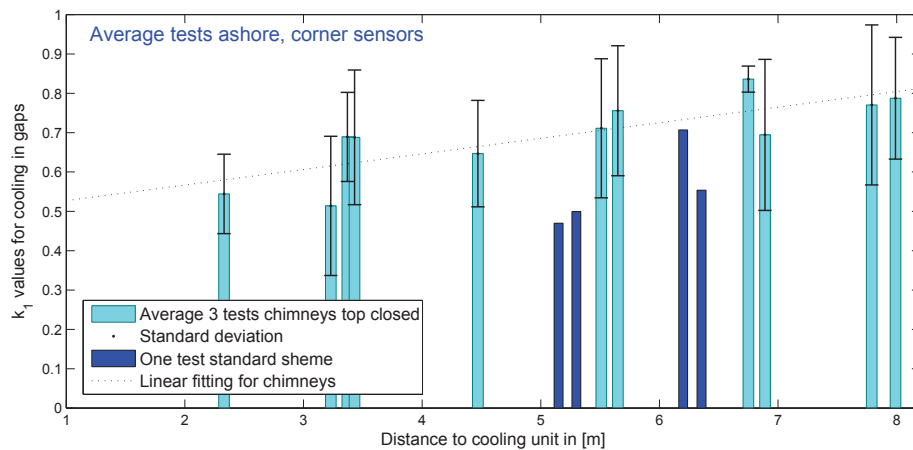

Figure 6.17: k1 values for cooling of the box corners. (Figure prepared by R. Jedermann)

Comparing the above mentioned results about the cooling effect (k1) with the airflow pattern is possible in an indirect way. The areas with higher air velocity values are the more ventilated and they have better cooling effect than areas with less air velocity values. In this context, the mean air velocity which corresponds to the tiers 5 to 7 of pallets was calculated from simulation results for both: chimney layout (L2_2) and standard scheme layout (L1). Results are presented in Fig. 6.18.

In this figure a similar trend is noticed for the cooling effect as in Fig. 6.17. Both figures show that the first part of container closest to the cooling unit has the minimum air velocity values as well as the poorest cooling. This fact assures the existence of hot spot in that area. Additionally, both figures confirm that the chimney based layout of pallets in the container provide better cooling effect and airflow distribution than the standard scheme layout. This new layout (L2_2) improves the ventilation near the cooling unit and participates in reducing the entrainment effect explained for the standard scheme (see Fig. 6.14). However, temperature values in this region are still the highest in the container. Fig. 6.19 shows the velocity magnitude in the XZ plane for the chimney layout.

As a conclusion, the chimney layout provides more uniform airflow distribution and
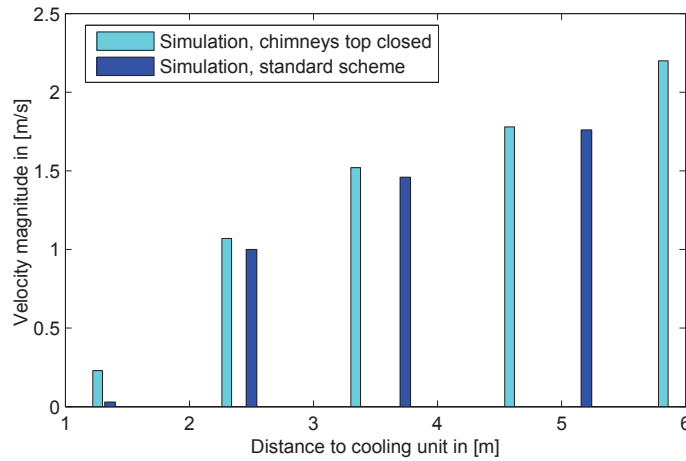
Figure 6.18: average velocity in gaps by simulation
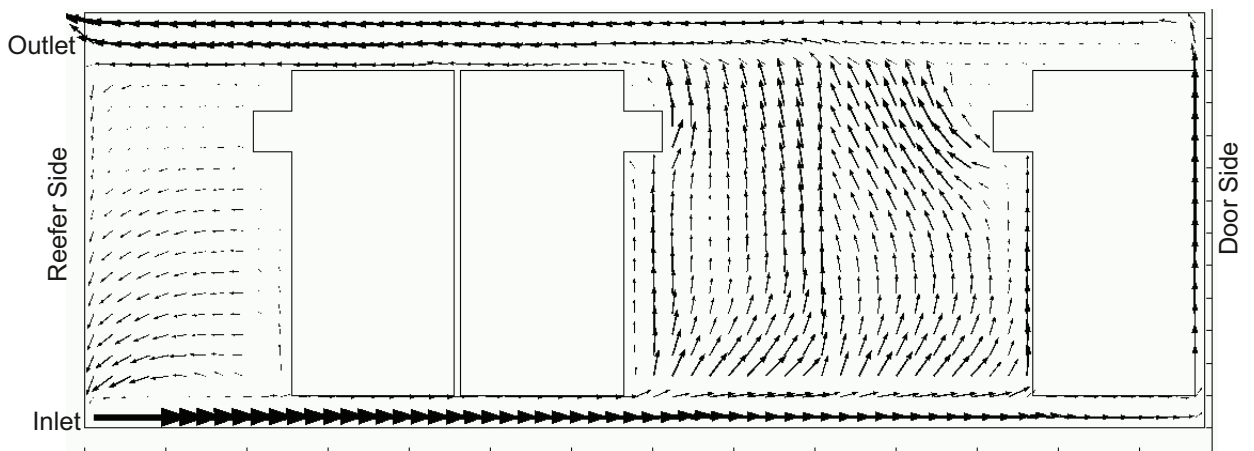
Figure 6.19: Velocity magnitude in the YZ-plane at (X= 1.05 m) for the chimney layout L2_2

has better cooling comparing with the standard layout. Cooling effect indications show that the cooling increases with the distance from cooling unit. This was validated by both simulation and temperature measurements for containers loaded by 11, 12 and 16 pallets. Loading the container with more pallets might lead to different airflow distributions.

7 Summary and Conclusions

This study set out to explore the benefits of evaluating airflow pattern in order to improve logistic processes in transport containers. The quality of transported sensitive products is highly affected by environmental conditions especially temperature. In the case of bananas, higher temperatures may speed up the ripening process or cause the senescence, whereas lower temperatures may cause freezing or chilling injury. Therefore, it is essential to have uniform temperatures throughout the system to maintain the quality and the shelf life during transportation.

In reefer containers, convection is the dominant mode of heat transfer, the temperature and its distribution are controlled by the airflow pattern. Distributed airflow is responsible for convecting generated heat in the container. Fruits keep producing heat and moisture after harvesting. Thus, in some regions of the transport container, where ventilation is poor, hot spots occur. As a consequence, commodities in these stagnant zones are subject to non-homogeneous deterioration which degrading their quality. Predicting the locations of the hot spots and then taking the necessary correction and preventive actions implies understanding the convection transport in the container. Airflow pattern were obtained by simulation and experimental measurements. In literature, there is a large number of simulated airflow and heat transfer studies in enclosed areas in the last few decades. Many of them are mentioned in [Zhai07, Amba13]. These studies have benefited from the huge development of computational fluid dynamics. Such numerical models, with their advantages of fast time and low cost, offer a powerful tool to understand fluid flow and heat transfer in the intended enclosed environments. Still, they cannot replace the extensive and costly experimentation which are imperative for validation and supervision. Moreover, the complexity of airflow pattern analysis and its dependency on many operating conditions have pushed researchers to recommend further parametric studies [Smal06]. In this context, some parametric studies, especially for temperature, were reported. However, there are very few reported studies about airflow measurements in the logistic containers. Furthermore, there is no flow sensor commercially available capable of performing wireless airflow measurements within the limitations and conditions of the container.

The above reasons are the motivation for this study to evaluate airflow pattern by measurements and simulations. This study singled out the thermal flow sensors as potential options to perform the airflow measurements in a logistic reefer container. Their small size, high sensitivity and ability to be used in wireless systems are the main reasons which support this choice. This study also developed $k - \epsilon$ model from

Reynolds-averaged Navier-Stokes approach to simulate airflow distributions in the container.

This study answers the questions:

1. Are thermal flow sensors capable and suitable for accurate airflow measurement in reefer containers?

2. How do airflow measurements and simulations improve transport processes for the logistic containers?

7.1 Thermal flow sensors characteristics

The selected flow sensors are micro-flow sensors which have been developed by IM-SAS a few years ago. In order to avoid repeating the previous studies done on theses sensors, this thesis considered only some essential issues which were not treated enough before.

First, a numerical simulation model for sensor response time and some other characteristics was presented in chapter 2. This model uses the finite-difference method to solve the heat transfer equations, taking into consideration the transient conduction and convection between the sensor membrane and the surrounding fluid. Program results agree with experimental measurements and explain the response time dependence on the velocity and sensor geometry. Values of the response time vary from about 5 ms in the case of stagnant flow to 1.5 ms for a flow velocity of 44 m/s. Additionally, response time increases with the distance between the heater and thermopiles. These results assure the suitability of selecting thermal flow sensors for the applications that require short response time.

Second, the study made a detailed characterization for the selected flow sensors. The characteristic curves were extracted for four different sensor configurations for the velocity range 0 to 5 m/s. It was found that the characteristic curves for the ultra-low range (10 to 10 SCCM) are linear. Additionally, the study focused more specifically on the minimum detectable air velocity feature of the thermal flow sensors. Theoretically, very small detection limits of air velocity of some micrometers per second are achievable. However, the superimposed free convection is the main obstacle which prevents reaching these expected limits. Furthermore, experimental investigations are an additional challenge since it is difficult to generate very low flows. The study introduced a physical method, capable of generating very low flow values in the mixed convection region. Moreover, it presented the sensor characteristic curves at the zero flow case and in the mixed convection region. Results show that the estimated minimum detectable air velocity by the presented method is 0.8 mm/s. The equivalent air velocity to the noise level of the sensor at the zero flow case is about 0.13 mm/s. Thermal flow sensors are capable of detecting very low air velocities by optimizing the noise sources. On the one hand, the natural convection can be minimized by either reducing the characteristic length or reducing the

temperature difference between the heater and surrounding air. The first solution requires reducing the sensor dimensions, for example by using narrow and deep air channels, whereas the second solution will decrease the sensor sensitivity and the measuring range. On the other hand the noise arising from the measurement system can be reduced by optimizing the choices of the circuit elements such as ADC with higher resolution. Moreover, the promising results of using micro-channels realized by microfluidic structures in providing very accurate measurements for very low flow rates, particularly for liquids, gives motivation to use such structure for airflow as well.

Third, the study introduced a calibration method for the sensors, since they need to be calibrated before manipulating in the experimental measurements. A new test-device was designed and manufactured for this calibration purpose; it is suitable for producing turbulent flow with air velocity ranged from 0 to 7 m/s. The sensor is placed in a long tube in which the air velocity is controlled through a mass flow controller. Sensor results were characterized, modeled by a MATLAB based function-model and then calibrated. The calibration method is based on direct comparison between readings of the sensor under calibration and a reference anemometer. Uncertainties, raised from various parameters that affect the flow measurement, were estimated for some chosen air velocity values. Results of this calibration method show that the maximum relative difference between the reference and the sensor under calibration is about 9 % for the range $0 - 3$ m/s; it decreases to 5 % for the range $3 - 7$ m/s with a combined uncertainty of about 0.24 m/s. The calculated errors and uncertainties are relatively large due to turbulent nature of the flow which meets the application conditions. Reducing sensor's uncertainty is possible for some other application where controllable flow passes through the sensor.

7.2 Airflow pattern by measurements and simulations

The study referred to airflow field tests which were prepared within the Intelligent Container activities. It described the differed types of sensors used in these tests, in addition to the necessary preparations. Constant power circuit was built; it is integrated into TelosB wireless platform to enable obtaining sensors data wirelessly through the "BananaHop protocol" in the container. (Note: the circuit, the TelosB platform and the BananaHop protocol were not designed or developed by the author). Rigid enclosures were designed and fabricated by 3D printing technology. These enclosures not only provide suitable housing to the sensors with their circuits, but also protect the sensors from any external forces. The new "airflow sensors" (flow sensors with the wireless circuits and enclosures) were calibrated in a calibration method based on the method described in sec. 4.2. Calibration curves were produced for the fifteen sensors prepared for the measurements. Several field tests took place in the container which was filled with banana pallets. Some tests'

results were presented in this study. Tests show that it is possible to obtain airflow velocity values in all places of the container: under/ above the pallets in gaps between pallets and in gaps between the container's walls and pallets. Sensors data were useful to analyze the turbulence intensity and some other parameters needed for the simulation model. Consequentially, tests' results answer positively to the first research question cited by this study. Results proved that thermal flow sensors are suitable and capable of performing accurate airflow measurements in the container. However, these results are not enough to give a complete evaluation of airflow distribution. The main reasons are: first, the number of available sensors (15 only) is very small comparing to the container dimensions. Second, the sensors were used in separate tests assuming that all conditions of experimental measurements are identical in repeated tests. In practice, the main factors that influence airflow distribution in the container are the gaps between pallets and it is almost impossible to obtain equal gaps between pallets.

Beside the experimental measurements, this study presented a COMSOL based simulation model. This model simulates airflow inside the container by a turbulent k-ε model. To be in accordance with the experimental setup, simulations were done for a reduced number of pallets in the container: 11 pallets for standard scheme layout (L1) and 12 for the chimney based layout (L2). A mesh sensitivity study was performed to ensure the accuracy of the results. In this mesh refinement, four different cases were tested. The selected mesh correspond to a result error less than 1.5 % with respect to the reference result. Simulations provided airflow pattern for both layouts. It is possible to produce, by these simulations, 1D, 2D or 3D figures showing airflow distributions in different locations of the container. Simulation results were partly verified by the experimental measurements. Furthermore, a comparison between the simulations with the spatial temperature profiles recorded during additional tests offshore and ashore, showed good agreement with effects predicted by airflow simulations. The main founding by the airflow study are summarized by:

- Chimney layout with closed-top (L2_2) provides comparatively, the best homogeneous airflow distribution in the whole container. The comparison included also the standard scheme layout (L1) and the opened-top chimney layout (L2_1). This conclusion was supported by a quantifying study where the standard deviation of the velocity values for (L2_2) is the minimum in most cases.

- Analyzing simulation results near the cooling unit recognize the existence of a big eddy in the first part of the container near the inlet. The air pushed into the container causes an entrainment effect where the existing air gets drawn into the developing wall jet (see Fig. 6.14). This result explains the highest temperature values found by offshore temperature measurements (see Fig. 6.13). Changing the layout to the chimney scheme contributes to limit this phenomenon and increases the velocity in this.

- A comparison study for the cooling effect, from the temperature offshore data,

gives the advantage to the chimney based layout. This result was supported by airflow simulation where a similar trend to the cooling effect was found (see Fig. 6.17 and Fig. 6.18).

These findings answer the second research question. Analyzing airflow distributions in the container and comparison with the experimental results of temperature enabled explaining the unexpected hot spot near the reefer side. In addition, using the chimney layout in distributing the pallets in the container improve the efficiency of the cooling unit and gives a better airflow distribution.

7.3 Outlook

It is recommended that further research be carried out the following areas:

- Further work needs to be done to reduce the size of the "airflow sensor". Now four layers are placed within the sensor's enclosures include: sensor's PCB, constant power circuit, TelosB platform and the battery. It would be interesting to develop only one circuit which includes all components and to reduce the battery size. Such changes may reduce the enclosure height by 60 %; as a result, the sensor's enclosure will produce less turbulence and give the possibility of using the sensors in smaller gaps.

- It is recommended that further simulations be achieved to consider the complexity of the container. In reality, each banana box has several holes with different shapes and sizes distributed on all sides of the box. These holes allow exchanging heat and airflow with the distributed airflow in the container. Therefore, adding heat transfer in the future simulations in addition to the detailed design of boxes and pallets will provide more accurate results.

- Further experimental investigations are recommended to test some ideas that may reduce the high temperatures in the front part of the container. As it was found and explained about the hot spot near the cooling unit caused by the entrainment effect of the wall jet, blocking some air ducts in container's floor and forcing air to go vertically in front part may reduce temperatures in that part of the container.

Acknowledgments

Bibliography

[Al-G07]   Al-Garni, A. M., Low speed calibration of hot-wire anemometers. Flow Measurement and Instrumentation 2007, 18 95–98

[Amba13]   Ambaw, A.; Delele, M. A.; Defraeye, T.; Ho, Q. T.; Opara, L. U.; Nicolaï, B. M.; Verboven, P., The use of CFD to characterize and design post-harvest storage facilities: Past, present and future. Computers and Electronics in Agriculture 2013, 93 (0), 184-194.

[Asha09]   Ashauer, M.; Glosch, H.; Hedrich, F.; Hey, N.; Sandmaier, H.; Lang, W. Thermal flow sensor for liquids and gases based on combinations of two principles. Sens. Actuat. A: Phys. 1999, 73, 7-13.

[Brek94]   Brekhovskikh L. M., Goncharov V. V. Mechanics of continua and wave dynamics, Springer-Verlag, Berlin, 1994.

[Buch06]   Buchner, R.; Sosna, C.; Maiwald, M.; Benecke, W.; Lang, W. A high temperature thermopile fabrication process for thermal flow sensors. Sens. Actuat. A: Phys. 2006, 130-131, 262-266.

[Buch07]   Buchner, R.; Bhargava, P.; Sosna, C.; Benecke, W.; Lang, W. Thermo-electric Flow Sensors with Monolithically Integrated Channel Structures for Measurements of Very Small Flow Rates. In Proceeding of the 2007 IEEE Sensors, Atlanta, GA, USA, 28–31 October 2007; pp. 828–831.

[Buch09]   Buchner, R. Hochtemperaturprozess zur Fertigung miniaturisierter thermischer Strömungssensoren und ihre Applikation in Flüssigkeiten; Verlag Dr. Hut: Munich, Germany, 2009.

[Carp11]   Carpman N., Turbulence Intensity in complex environments and its influence on small wind turbines, Examensarbete vid Institutionen för geovetenskaper ISSN 1650-6553 Nr 219, Uppsala, 2011.

[CFD11]   CFD Online (07 September 2011), Law of the Wall, http://www.cfd-online.com/Wiki/Law_of_the_wall (accessed on 11 November 2013).

[CFD13-1]   CFD Online (21 August 2013), Introduction to Turbulence, http://www.cfd-online.com/Wiki/Introduction_to_turbulence/Reynolds_averaged_equations (accessed on 20 November 2013).

[CFD13-2]   CFD Online (22 August 2013), Standard k-epsilon Model, http://www.cfd-online.com/Wiki/Standard_k-epsilon_model (accessed on 20 November 2013).

[COMS12] COMSOL Multiphysics 4.3, User's Guide. COMSOL 2012.

[Cubu10] Cubukcu, A.S.; Zernickel, E.; Buerklin, U.; Urban, G.A. A 2D thermal flow sensor with Sub-mW power consumption. Sens. Actuators A Phys. 2010, 163, 449–456.

[Bree99] de Bree, H.-E.; Jansen, H.V.; Lammerink, T.S.J.; Krijnen, G.J.M.; Elwenspoek, M. Bi-directional fast flow sensor with a large dynamic range. J. Micromech. Microeng. 1999, 9, 186-189.

[Flem01] Fleming, W. J., Overview of automotive sensors. Sensors Journal, IEEE 2001, 1 (4), 296-308.

[Furn89] Furness, R. A., Fluid flow measurement. Longman: Harlow, UK, 1989.

[Gian07] Gianchandani, Y.; Tabata, O.; Zappe, H. Comprehensive Microsystems; Elsevier Science and Technology: Cambridge, UK, 2007.

[Graf07] Graf, A.; Arndt, M.; Sauer, M.; Gerlach, G., Review of micromachined thermopiles for infrared detection. Meas. Sci. Technol. 2007, 18 59–75.

[Haas08] Haasl, S.; Stemme, G., Flow sensors. In Comprehensive Microsystems, Elsevier Books: 2008; Vol. 2.

[Hed10] Hedrich, F.; Kliche, K.; Storz, M.; Billat, S.; Ashauer, M.; Zengerle, R. Thermal flow sensors for MEMS spirometric devices. Sens. Actuat. A: Phys. 2010, 162, 373-378.

[Herw86] Herwaarden, A. W. V.; Sarro, P. M., Thermal sensors based on the Seebeck effect. Sensors and Actuators 1986, 10 321-346.

[Incr02] Incropera, F.P.; DeWitt, D.P. Fundamentals of Heat and Mass Transfer, 5th ed.; John Wiley & Sons: Hoboken, NJ, USA, 2002.

[IVM08] International Vocabulary of Metrology–Basic and general concepts and associated terms (VIM). 3rd ed.; JCGM 200: 2008.

[Issa11] Issa S, Sturm H, Lang W (2011) Modeling of the Response Time of Thermal Flow Sensors. Micromachines 2: 385-393.

[Issa12] Issa, S.; Lloyd, C.; Lang, I. W., Calibration of Thermal Flow Sensors by New Test Device for Low Airflow Rates. International Graduate School for Dynamics in Logistics, 2012, 23.

[Issa13-1] Issa, S.; Lang, W., Characterization of Thermal Flow Sensors for Air Flow Measurements in Transport Containers. In Dynamics in Logistics, Kreowski, H.-J.; Scholz-Reiter, B.; Thoben, K.-D., Eds. Springer Berlin Heidelberg: 2013; pp 361-370.

[Issa13-2] Issa, S.; Lang, W., Minimum Detectable Air Velocity by Thermal Flow Sensors. Sensors 2013, 13 (8), 10944-10953.

[JCGM08] JCGM 100:2008. Evaluation of measurement data – Guide to the expression of uncertainty in measurement.

Bibliography

[Jede09]   Jedermann R, Ruiz-Garcia L , Lang W (2009) Spatial temperature pro-
           filing by semi-passive RFID loggers for perishable food transportation.
           Computers and Electronics in Agriculture 65: 145-154.

[Jede13]   Jedermann, R.; Geyer, M.; Praeger, U.; Lang, W., Sea transport of ba-
           nanas in containers – Parameter identification for a temperature model.
           Journal of Food Engineering 2013, 115 (3), 330-338.

[John28]   Johnson J. B (1928) Thermal Agitation of Electricity in Conductors.
           Physical Review 32: 97-109.

[Kaan10]   Kaanta, B.C.; Chen, H.; Zhang, X. Novel device for calibration-free flow
           rate measurements in micro gas chromatographic systems. J. Micromech.
           Microeng. 2010, doi:10.1088/0960-1317/20/9/095034.

[Kade04]   Kader, A. A.; Rolle, R. S., The role of post-harvest management in as-
           suring the quality and safety of horticultural produce. FAO: 2004; Vol.
           152.

[Kalt99]   Kaltsas G, Nassioppoulou A. G (1999) Novel C-MOS compatible mono-
           lithic silicon gas flow sensor with porous silicon thermal isolation. Sensors
           and Actuators A: Physical 76: 133-138.

[Karp99]   Karpelson, A., Computation of Mean Velocity Distribution in a Turbulent
           Flow. arXiv preprint physics/9904030 1999.

[Busc90]   Kenneth W. Busch, Marianna A. Busch (1990). Multi-element Detec-
           tion Systems for Spectrochemical Analysis. Wiley-Interscience. ISBN
           0471819743

[Kest05]   Kester, W. Taking the Mystery out of the Infamous Formula, NR = 6.02
           N+ 1.76 dB "and Why You Should Care; Analog Devices MT-001 2005;
           Available online: http://www.locutus.it/sundry/ MT-001.pdf (accessed
           on 7 August 2013).

[Kim09]   Kim T. H., Kim D. K., Kim S. J. (2009) Study of the sensitivity of a
           thermal flow sensor. International Journal of Heat and Mass Transfer 52:
           2140-2144.

[Kohl03]   Kohl, F.; Fasching, R.; Keplinger, F.; Chabicovsky, R.; Jachimowicz,
           A.; Urban, G. Development of miniaturized semiconductor flow sensors.
           Measurement 2003, 33, 109-119.

[Koth07]   Kothandaraman, C. P.; Rudramoorthy, R., Fluid mechanics and machin-
           ery 2ed.; New Age International (P) Ltd.: New Delhi 2007.

[Kuo12]   Kuo, J.T.W.; Yu, L.; Meng, E. Micromachined thermal flow sensors—A
           review. Micromachines 2012, 3, 550–573.

[Lagu12]   Laguerre, O.; Hoang, M. H.; Osswald, V.; Flick, D., Experimental study
           of heat transfer and air flow in a refrigerated display cabinet. Journal of
           Food Engineering 2012, 113 (2), 310-321.

[Land87]   Landau L. D., Lifshitz E. M. Fluid Mechanics, Pergamon Press, Oxford, 1987.

[Lang90]   Lang, W. Heat transport from a chip. IEEE Trans. Electron Devices 1990, 37, 958-963.

[Lang11]   Lang, W.; Jedermann, R.; Mrugala, D.; Jabbari, A.; Krieg, B.; x; ckner, B.; Schill, K., The Intelligent Container ;A Cognitive Sensor Network for Transport Management. Sensors Journal, IEEE 2011, 11 (3), 688-698.

[Lang12]   Lang, W., Sensors, course notes: 2012

[Liao13]   Liao, S.H.; Chen, W.J.; Lu, M.S.C. A CMOS MEMS capacitive flow sensor for respiratory monitoring. IEEE Sens. J. 2013, 13, 1401–1402.

[Lien08]   Lienhard, J. H. I. V.; Lienhard, J. H. V., A Heat Transfer textbook. 3rd ed.; Phlogiston Press: Cambridge, 2008.

[Lloy13]   Lloyd, C.; Issa, S.; Lang, W.; Jedermann, R. In Empirical airflow pattern determination of refrigerated banana containers using thermal flow sensors, Cool chain-Management, 5th International Workshop, University of Bonn, Bonn, University of Bonn, Bonn, 2013.

[Mour09]   Moureh J, Tapsoba S, Derens E et al (2009) Air velocity characteristics within vented pallets loaded in a refrigerated vehicle with and without air ducts. International journal of refrigeration 32: 220-234.

[Nieu94]   Nieuwstadt, F.T.M.; Eggles, J.G.M.; Janssen,R.J.A.; Pourquie, M.B.J.M, Direct and large-eddy simulations of turbulence in fluids. Future Generation Computer Systems, 1994, 10 189–205.

[Oli99]   Olin, J. G., Industrial thermal mass flowmeters. Measurement & Control 1999, 193, 83-90.

[Özah10]   Özahi, E.; Çarppinlioglu, M. Ö.; Gündogdu, M. Y., Simple methods for low speed calibration of hot-wire anemometers. Flow Measurement and Instrumentation 2010, 21, 166 -170.

[Pats12]   Patsis, G.P.; Petropoulos, A.; Kaltsas, G. Modelling and evaluation of a thermal microfluidic sensor fabricated on plastic substrate. Microsyst. Technol. 2012, 18, 359–364.

[Paul99]   Paull, R., Effect of temperature and relative humidity on fresh commodity quality. Postharvest Biology and Technology 1999, 15 (3), 263-277.

[Pitt98]   Pitts, D.; Sissom, L. Schaum's Outlines of Theory and Problems of Heat Transfer, 2nd ed.; McGraw-Hill: New York, NY, USA, 1998.

[Rodr07]   Rodríguez-Bermejo, J.; Barreiro, P.; Robla, J. I.; Ruiz-García, L., Thermal study of a transport container. Journal of Food Engineering 2007, 80 (2), 517-527.

[Silv12]   Silvestri, S.; Schena, E., Micromachined flow sensors in biomedical applications. Micromachines 2012, 3 (2), 225-243.

[Smal06]   Smale, N. J.; Moureh, J.; Cortella, G., A review of numerical models of airflow in refrigerated food applications. International Journal of Refrigeration 2006, 29 (6), 911-930.

[Sosn]   Sosna, C., Diplom arbeit.

[Sosn11]   Sosna, C.; Walter, T.; Lang, W. Response time of thermal flow sensors with air as fluid. Sens. Actuat. A: Phys. 2011, doi:10.1016/j.sna.2011.02.023.

[Spit84]   Spitzer, D. W., Industrial flow measurement. The Instrument Society of America: Durham NC, USA, 1984.

[Sun07]   Sun, J.-B.; Qin, M.; Huang, Q.-A. Flip-chip packaging for a two-dimensional thermal flow sensor using a copper pillar bump technology. IEEE Sens. J. 2007, 7, 990–995.

[Putt99]   Van Putten, M.J.A.M.; van Putten, M.H.P.M.; van Putten, A.F.P. Thermal flow measurements at Gr/Re2 >>1 by silicon anemometry. IEEE Trans. Instrum. Meas. 1999, 48, 724–729.

[Weck97]   Weckmann, S. Dynamic electrothermal model of a sputtered thermopile thermal radiation detector for earth radiation budget applications. Virginia Polytechnic Institute and State University, 1997.

[Xie06]   Xie, J.; Qu, X.-H.; Shi, J.-Y.; Sun, D.-W., Effects of design parameters on flow and temperature fields of a cold store by CFD simulation. Journal of Food Engineering 2006, 77 (2), 355-363.

[Zhai07]   Zhai, Z. J.; Zhang, Z.; Zhang, W.; Chen, Q. Y., Evaluation of Various Turbulence Models in Predicting Airflow and Turbulence in Enclosed Environments by CFD: Part 1—Summary of Prevalent Turbulence Models. HVAC&R Research 2007, 13 (6), 853-870.

[Zhan07]   Zhang, Z., Modeling of airflow and contaminant transport in enclosed environments, Dissertation 2007, Purdue University.

[Zou06-1]   Zou, Q.; Opara, L. U.; McKibbin, R., A CFD modeling system for airflow and heat transfer in ventilated packaging for fresh foods: I. Initial analysis and development of mathematical models. Journal of Food Engineering 2006, 77 (4), 1037-1047.

[Zou06-2]   Zou, Q.; Opara, L. U.; McKibbin, R., A CFD modeling system for airflow and heat transfer in ventilated packaging for fresh foods:: II. Computational solution, software development, and model testing. Journal of Food Engineering 2006, 77 (4), 1048-1058.

Author Publications

[1] Issa, S.; Sturm, H.; Lang, W., Modeling of the Response Time of Thermal Flow Sensors. Micromachines 2011, 2 (4), 385-393.

[2] Issa, S.; Lloyd, C.; Lang, W., Calibration of Thermal Flow Sensors by New Test Device for Low Airflow Rates. International Graduate School for Dynamics in Logistics, Research Report 2012/2013, 23-26.

[3] Issa, S.; Lang, W., Minimum Detectable Air Velocity by Thermal Flow Sensors. Sensors 2013, 13 (8), 10944-10953.

[4] Issa, S.; Lang, W., Characterization of Thermal Flow Sensors for Air Flow Measurements in Transport Containers. In Dynamics in Logistics, Kreowski, H.-J.; Scholz-Reiter, B.; Thoben, K.-D., Eds. Springer Berlin Heidelberg: 2013; pp 361-370.

[5] Safaei, M.; Issa, S.; Seifert, M.; Thoben, K.-D.; Lang, W., A Method to Estimate the Accumulated Delivery Time Uncertainty in Supply Networks. In Dynamics in Logistics, Kreowski, H.-J.; Scholz-Reiter, B.; Thoben, K.-D., Eds. Springer Berlin Heidelberg: 2013; pp 337-347.

[6] Lloyd, C.; Issa, S.; Lang, W.; Jedermann, R., Empirical airflow pattern determination of refrigerated banana containers using thermal flow sensors, Cool chain-Management, 5th International Workshop, University of Bonn, Bonn, 2013.

[7] Lloyd, C.; Pötsch, T.; Yi, S.; Zuniga, R.; Safaei, M.; Issa, S.; Rügge, I., Resources in Logistics- A Multidisciplinary Challenge. 6th International Conference on Management and Control of Production and Logistics, Fortaleza, Ceará, Brazil, 2013.

[8] Issa, S.; Lang, W., Airflow simulation in reefer Containers, 4th International Conference on Dynamics in Logistics, University of Bremen, Bremen, 2014.